Master's Thesis

Sidse Lærke Lolk

Frustrated magnetism in Cr-jarosite

Supervisors:
Kim Lefmann
Niels Bohr Institute, University of Copenhagen

Ulla Gro Nielsen
Department of Physics, Chemistry and Pharmacy, University of Southern Denmark

Submitted October 24, 2020

Abstract

The subgroup of magnetic materials which are subject to geometric frustration experience competing interactions of the spins, thereby suppressing magnetic order, which might give rise to exotic phenomena such as quatum spin liquid phases. Here we investigate the magnetic properties of the frustrated antiferromagnetic $S = \frac{3}{2}$ kagomé system Cr-jarosite $KCr_3(SO_4)_2(OH)_6$. Deuterated samples of Cr-jarosite were produced by hydrothermal synthesis, and chemical characterization of the samples was performed by ^2H nuclear magnetic resonance, thermogravimetric analysis, infrared spectroscopy, powder x-ray diffraction, scanning electron microscopy, and energy-dispersive x-ray spectroscopy. The measurements revealed that the combined sample consists predominantly of stoichiometric Cr-jarosite, with $\sim$2 % Cr vacancies, and that $\sim$18-28 % of K on the A-site is substituted with D_nO. PXRD revealed disordered stacking of the kagomé planes, most likely caused by D_3O^+. Inelastic neutron scattering experiments were performed on a combined sample using the instruments MARI and LET at ISIS. The neutron spectroscopy revealed a co-existence of magnetic properties in the form of 3D antiferromagnetic ordering and 2D dynamics. The magnetic ordering refutes Cr-jarosite as a potential spin liquid.

Acknowledgments

This thesis would not have been possible without the help and patience of my brilliant and always supportive supervisors Kim Lefmann and Ulla Gro Nielsen.

Christian Brandt Jørgensen has been a great support in the NMR and IR lab work at University of Southern Denmark. Anders Bruhn Arndal Andersen has provided tremendous support in all the lab work at University of Southern Denmark, as well as being very patient and supportive with my at times endless streams of questions and lack of experience with chemical concepts. Also a special thanks to Tae-Hyun Kim who was so kind to perform the SEM and EDS measurements.

Thanks to Mikkel Juelsholt for providing crystallographic information on deuterated Cr-jarosite.

The instrument scientists Tatiana Guidi and Duc Le were amazingly helpful both at and after the beamtime at MARI, as well as at the LET beamtime.

Thanks to Sofie Janas for always being a great source of both mental and academic support, hand-holding throughout data analysis and providing, at times much needed, encouragement.

Thanks to Mads Kildholt for unlimited tex and mental support all throughout this project. Thanks to Nanna Bach-Møller for endless supplies of tea, improvised office space, and linguistic support.

I am very thankful for everyone who took the time to read through drafts of my thesis.

Contents

1 Introduction

The subject of material science hosts a wide variety of research fields, often interdisciplinary between physics, chemistry and engineering. The field of solid state physics research is especially flourishing at the moment, exploring, among many things, the properties of futuristic materials such as carbon nanotubes, high temperature superconductors, and semiconductors for possible use in quantum computers [1]. Exploring the properties of materials do not necessarily yield an obvious purpose for said material, but this kind of fundamental research is nevertheless important for facilitating new discoveries and adding to the foundation of knowledge in material science.

Solid state physics investigates materials with lattice structures: systematic arrangement of atoms which form compounds where the structure on the atomic level dictates the overall properties of the material. This holds especially true for magnetic materials where it is the arrangement of spins which create the magnetic phenomena, such as the parallel and antiparallel alignment of spins which create ferro- and antiferromagnetism [2]. Antiferromagnetism is a type of magnetic ordering which does not show itself macroscopically, unlike the obvious magnetic effects seen from, for example, ferromagnetism in permanent magnets. In antiferromagnets, every spin seeks to be aligned antiparallel to its neighbor, causing the material to have a total magnetization of zero. The properties of antiferromagnets are investigated through techniques such as neutron scattering, which can probe the atomic structure and spins. Antiferromagnetic materials can exhibit phenomena such as frustration, where competing interactions and orientations of spins suppresses the magnetic ordering. The ground state becomes degenerate which can facilitate some unusual phases of matter, such as quantum spin liquids, which theoretically should evade order altogether, even at $T = 0$ K.

Frustration occurs in systems where the lattice structure hinders antiferromagnetic alignment. Such lattice systems are usually triangular in nature, and include systems such as kagomé and pyrochlore lattices. The family of compounds with kagomé lattices hosts a vast selection of possible spin liquid candidates [3], among them the substance of interest for this study: Cr-jarosite, $KCr_3(SO_4)_2(OH)_6$. Studies of Cr-jarosite are found in both chemistry and physics oriented research, generally with focus on stoichiometry or magnetic properties respectively. This study aims to use both in order to get an in depth analysis of the compound and its properties.

My contribution to this project started out with synthesizing seven Cr-jarosite powder samples, six of which are deuterated, which were then combined to one collective deuterated sample. I then performed characterization experiments on the subsamples and combined sample respectively, using multiple techniques: nuclear magnetic resonance, thermogravimetric analysis, infrared spectroscopy, and powder x-ray diffraction. The characterization was done in order to determine if the correct stoichiometric compound was achieved, as well as the type and quantity of defects that might be present. The multitude of techniques warrants that the characterization is as comprehensive as possible.

Time-of-flight neutron scattering experiments were performed on the combined sample in order to reveal the magnetic structure and dynamics. I participated in the beamtime at the instrument MARI on ISIS, which were later followed up with a beamtime on LET, ISIS, and analyzed the data from these experiments. The LET beamtime was carried out by the scientists at ISIS.

This thesis includes data from scanning electron microscopy and energy-dispersive x-ray

spectroscopy, which were performed by Dr. Tae-Hyun Kim, University of Southern Denmark, as well as results from susceptibility measurements performed by PhD student Sofie Janas, University of Copenhagen.

2   Magnetism

Magnetism in materials is intrinsically due to the magnetic moment of the atoms in the material. The magnetic moment of a particle is proportional to the angular momentum of said particle. Both the nucleus and electrons of an atom have magnetic moment, but the electron magnetic moment is significantly larger than that of the nucleus. In the following, only the magnetic moment of the electron will be considered. The nuclear magnetic moment is examined in section 5.1.

Since angular momentum of particles consists of both orbital angular momentum, $\boldsymbol{L}$, and spin angular momentum, $\boldsymbol{S}$, the magnetic moment can be given as both an orbital magnetic moment and a spin magnetic moment [4]:

$$\boldsymbol{\mu_L} = -g_L \mu_B \boldsymbol{L} \tag{1}$$

$$\boldsymbol{\mu_S} = -g_S \mu_B \boldsymbol{S} \tag{2}$$

The negative sign comes from the electron charge. μ_B is the Bohr magneton, $\mu_B = \frac{e\hbar}{2m_e}$, which serves as unit of measuring the magnetic moment. g_L and g_S is the g-factor, which serves as a proportionality constant, for the orbital and spin angular momenta respectively. The value of g_L depends the mass of the nucleus, where g_S normally have the value of $\simeq 2$ [2].

The total magnetic moment is just the sum of the orbital and spin components:

$$\boldsymbol{\mu} = -g_J \mu_B \boldsymbol{J} \tag{3}$$

Where $\boldsymbol{J}$ is the total angular momentum $\boldsymbol{J} = \boldsymbol{L} + \boldsymbol{S}$. g_J is the g-factor for the total angular momentum, known as the Landé g-factor.

In order to describe the bulk behavior of the magnetic moments in a solid, the term magnetization is used, which describes the magnetic moment per unit volume:

$$\boldsymbol{M} = \frac{d\boldsymbol{\mu}}{dV} \tag{4}$$

When there is no preferred orientation for the magnetic moments each magnetic moment will point in a random direction, whereby the magnetization will be $\boldsymbol{M} = 0$.

The magnetization is related to the magnetic field $\boldsymbol{H}$ by a quantity known as the magnetic susceptibility, χ. For a linear magnetic material the relation is [2]:

$$\boldsymbol{M} = \chi \boldsymbol{H} \tag{5}$$

The magnetic susceptibility is a measure of how the material responds to an applied magnetic field. A positive susceptibility indicates that the magnetization aligns with the applied magnetic field. This is called paramagnetism. A negative magnetic susceptibility on the other hand indicates that the magnetization opposes the applied field, which is called diamagnetism. Paramagnetism contribute to a weak attraction towards the magnetic field, where diamagnetism contribute to a weak repulsion from the magnetic field.

Diamagnetism is a weak effect which is inherent to all materials, whereas for paramagnetic materials, the diamagnetic effect is outweighed by the much stronger paramagnetic effect [2]. Both diamagnetism and paramagnetism are effects related to how the material reacts to an applied magnetic field, whereas other types of magnetism, e.g. ferromagnetism, describes a magnetic behavior which is not induced by an external magnetic field.

2.1 Magnetic ordering

Ferromagnetism and antiferromagnetism describes an inherent magnetic order in materials. Ferromagnetic materials exhibit spontaneous magnetization, meaning that the spins align in some direction without exposure to a magnetic field. An example of ferromagnetic ordering is shown in figure 1a. Ferromagnetism is probably what most people associate with magnetism since this is the mechanism behind permanent magnets, as, for example, in fridge magnets.

Antiferromagnetism is a type of magnetic order where neighboring spins are antiparallel, as illustrated in figure 1b. This results in them having no magnetization without applying an external magnetic field. Therefore antiferromagnetic materials do not exhibit any macroscopic magnetic effects, as opposed to ferromagnets. The antiferromagnetic lattice can be considered as two superimposed ferromagnetic sublattices, illustrated by the red and blue arrows in figure 1b, respectively.

Even though the focus in this thesis is on antiferromagnetic materials, some ferromagnetic theory is included as well, since it is often illustrative to compare the two concepts.
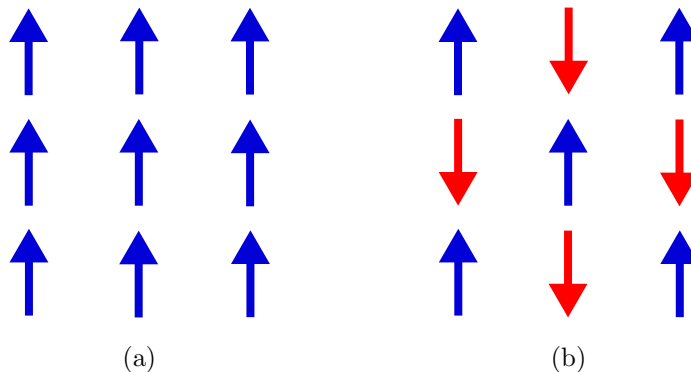

Figure 1: Illustration of magnetic ordering on a square lattice. (a) Ferromagnetic ordering: all spins are oriented in the same direction. (b) Antiferromagnetic ordering: neighboring spins have opposite orientations.

Whether ferromagnetic or antiferromagnetic, a material exhibits this kind of spontaneous ordering only below a certain temperature, called the ordering temperature or critical temperature. Above the critical temperature the material is paramagnetic. The critical temperature for ferromagnetic and antiferromagnetic materials is called the Curie temperature, T_C, and Néel temperature, T_N, respectively, since their discoveries are attributed to different physicists.

The temperature dependence of this phase transition is described by Landau theory and the temperature dependence in the paramagnetic phase is described by the Curie-Weiss law. This is expressed via the susceptibility, the graphs of which is illustrated in figure 2. For a purely paramagnetic material there is no phase transition and the susceptibility follows the Curie law in the entire temperature range [5]:

$$\chi = \frac{C}{T} \qquad (6)$$

C is the Curie constant. The Curie law translates the fact that materials generally becomes less magnetically responsive as the temperature is increased.
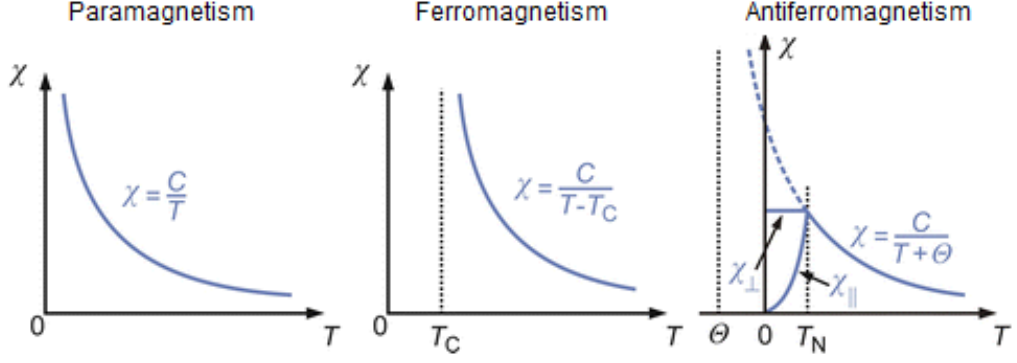
Figure 2: Temperature dependence on susceptibility for three types of magnetically ordered systems, adapted from [6].

Ferromagnetic and antiferromagnetic materials essentially behave paramagnetically until they reach their maximal susceptibility at the critical temperature. Exactly at the phase transition the theory fails to describe the phenomena, as it is based on an average of the system, but at the phase transition fluctuations become increasingly important [2]. For ferromagnetic materials the susceptibility above T_C is expressed by the Curie-Weiss law:

$$\chi = \frac{C}{T - T_C} \tag{7}$$

Below the critical temperature the material spontaneously orders in several magnetic domains which can be influenced by external magnetic fields. The behavior below T_C is too complex to be described in detail here, but is nevertheless interesting.

Antiferromagnetic materials follow the same behavior as ferromagnets, but with a change of sign in the expression and defined by the Curie-Weiss temperature, Θ:

$$\chi = \frac{C}{T + \Theta} \tag{8}$$

The Néel temperature, T_N, is not part of the expression, but the relation is nonetheless still only valid above T_N.

Θ (sometimes written as Θ_{CW}) characterizes the sign and strength of the magnetic interactions [6]. The reason for the change in sign is that Θ is negative for antiferromagnets. This is illustrated by the dashed curve in figure 2, but perhaps more clearly in figure 3: Often the susceptibility is depicted graphically by $\frac{1}{\chi}$, where Θ then becomes the point where the graph crosses the temperature axis. For ferromagnets this is at $T_C > 0$, but for antiferromagnets it occurs at $\Theta < 0$.

As indicated on figure 2 the behavior of the antiferromagnetic susceptibility below T_N is separated into two parts which is respectively perpendicular, $\chi_\perp$, and parallel, $\chi_\parallel$, to an external magnetic field [6]. This behavior is explained in e.g. [8], but will not be discussed further here.
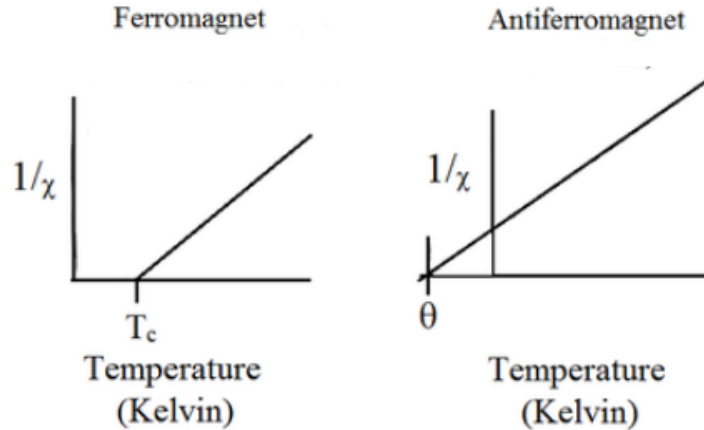
Figure 3: Rough sketch of temperature dependence on inverse susceptibility for ferromagnetic and antiferromagnetic systems, adapted from [7].

2.2   Magnetic interactions

The way neighboring spins interact in ordinary ferromagnets and antiferromagnets can be described by the Heisenberg Hamiltonian, which is valid for localized electrons in insulators [2]:

$$\hat{H} = -\sum_{ij} J_{ij} \boldsymbol{S}_i \cdot \boldsymbol{S}_j \tag{9}$$

Here $\boldsymbol{S}_i$ and $\boldsymbol{S}_j$ refer to two neighboring spins. Often it easiest to consider only nearest neighbor interactions, but sometimes contributions from next-nearest or third-nearest neighbors are considered as well. J_{ij} is called the exchange constant and is a measure of strength of the interaction between the two spins. The sign of J determines whether it is energetically favorable for neighboring spins to be parallel or antiparallel. For ferromagnets, the exchange interaction is positive, $J > 0$, whereas for antiferromagnets it is negative, $J < 0$ [2].

2.2.1   Dzyaloshinski-Moriya interaction

The Dzyaloshinski-Moriya (DM) interaction, antisymmetric exchange and anisotopic exchange are synonymous terms which describe an interaction that causes canting of otherwise (anti)parallel spins.
Derivation of the DM interaction is done using perturbation theory in combination with the spin-orbit coupling [9]. This yields the following formalism for the interaction:

$$\hat{H}_{\mathrm{DM}} = \sum_{ij} \boldsymbol{D}_{ij} \cdot (\boldsymbol{S}_i \times \boldsymbol{S}_j) \tag{10}$$

When used in calculations for a spin system this term is added to the already existing Hamiltonian for the system, e.g. the Heisenberg Hamiltonian.
In antiferromagnetic materials spin canting causes a slight ferromagnetic effect, as it results in a small net magnetization.

6

2.3 Magnetic excitations

Solids are subject to many types of excitations, some related to the lattice and some related to the spin structure. An example of a lattice excitation would be phonons, which correspond to vibrations in the lattice. Excitations in spin, i.e. the magnetic structure, could among others be spinons, magnetic domain walls, magnetic monopole-like excitations [10] and spin waves. Within frustrated systems it is possible that many more exotic types of excitations exists.
In the following sections the focus will mainly be on explaining the concepts of spin waves and frustration.

2.3.1 Spin wave theory

Spin waves are an excitation to the ordering of spins in a solid. Spin waves are also referred to as magnons, which is the quasiparticle description of the same phenomenon. Typically the term spin wave is used when describing the wave-like dynamics of the excitation and magnon is used when describing the overall qualities of the excitation.

Magnons are a type of Goldstone modes, which refer to a global symmetry being broken and in the process creating massless quasiparticles which require little to no energy to produce [2]. In the case of magnons it is the spin symmetry in the system which is broken since it is equivalent to flipping one spin from the ordered spin state. Magnons have spin 1 and are therefore bosons.
This flipped-spin-excitation travels through the lattice in a wave-like manner where successive spins advance in phase by a constant angle [8]. The spin wave concept is most easily displayed in the ferromagnetic lattice, seen in figure 4. The figure show the side and top view of how the spins advance in phase, showing how the movement corresponds to a wave.
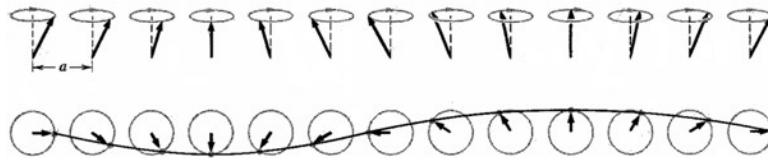

Figure 4: Spin wave in a ferromagnetic chain of spins. From [8].

Spin waves in an antiferromagnet behave similarly to those in a ferromagnet. The ordered ground state of a antiferromagnet where all neighboring spins are perfectly antiparallel is called the Néel state. As a spin wave travels through the lattice, the advance in phase happens in both the spin up and spin down sublattice, illustrated in figure 5.
The way a spin wave travels through a material is described by its dispersion relation. The dispersion relation for a simple antiferromagnetic chain of spins is derived in detail in [8] and [11] among others, yielding $\hbar\omega \propto 4JS|\sin(ka)|$ (for context the dispersion relation for spin waves in a simple ferromagnetic 1D chain is $\hbar\omega = 4JS(1 - \cos(ka))$). For small ka this relation is linear. The antiferromagnetic dispersion relation is shown in figure 5. Dispersion relations for more complicated systems are often much more difficult to obtain.
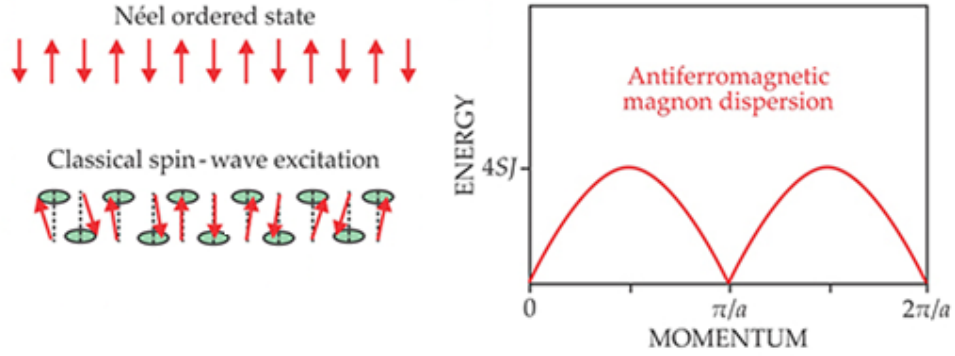
Figure 5: Spin wave in an antiferromagnetic chain of spins. Adapted from [12].

2.4 Frustrated magnetism

Since antiferromagnetic order is based on each spins relation to its neighbor, the arrangement of atoms in the lattice has a huge influence on the antiferromagnetic properties. The lattice can be arranged in such a way that the antiferromagnetic alignment of spins cannot be fulfilled - a concept referred to as geometric frustration.

The classic example of frustration is in the triangular lattice, illustrated in figure 6. The triangular layout makes it impossible for all three spins to be aligned antiferromagnetically, and the system ends up being 'frustrated'.
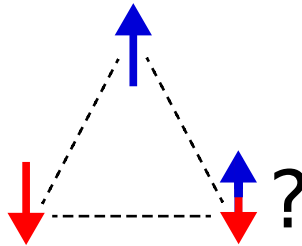

Figure 6: Illustration of the principle behind geometrical frustration on a triangular lattice: if two spins in the triangle are antiferromagnetically coupled, the third cannot be antiferromagnetically coupled to both of them, so the system is 'frustrated'.

Since a 'true' antiferromagnetic ground state cannot be achieved, multiple spin configurations which try to minimize the energy exist, i.e. the ground state becomes degenerate. This ground state degeneracy is considered the defining characteristic of a frustrated system [13]. The degeneracy suppress the Néel order, pushing T_N towards zero, and perfectly frustrated systems should not be able to order at all.

In general, frustrated systems are described by Hamiltonians with competing interactions, where the energy cannot be minimized for all interactions simultaneously [3].

A measure of frustration in a system is the frustration parameter, f, defined as $f = \frac{|\Theta|}{T_N}$, i.e. comparing the Curie-Weiss temperature with the temperature at which order freezes, T_N. If the frustration parameter has a higher value than 5-10, this generally indicates strongly suppressed ordering as a result of frustration [13]. For such systems the behav-

8

ior below T_N will be nongeneric and depend heavily of the compound in question, and the intermediate regime $T_N > T > |\Theta|$, called the cooperative paramagnetic regime, are generally dominated by weak correlations [14].

The different types of frustrated lattice structures can gives rise to different types of degeneracies, which are named according to their resemblance to ordering types in other natural phenomena, such as spin glass, spin ice, and spin liquid.

2.4.1 The kagomé lattice

The kagomé lattice is one of the systems which are subject to frustration, since it consists of corner sharing triangles. The system gets its name from a Japanese basket weave pattern with the same layout.
Since the spins in a kagomé antiferromagnet cannot fulfill the antiparallel ordering, they might find more unusual ways to order. The most common types of kagomé orderings is illustrated in figure 7.
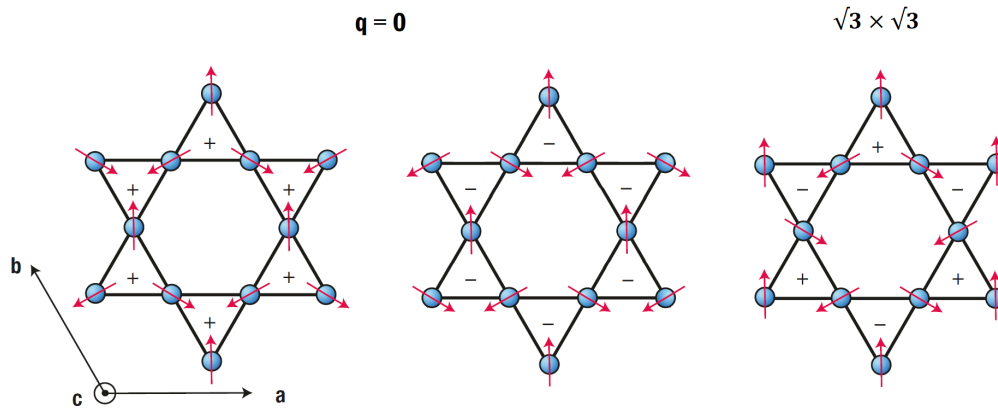

Figure 7: Illustration of possible spin ordering in a kagomé lattice. + and - denote positive and negative chirality of spins in the triangles. The first two orderings is both called $q = 0$ with positive and negative chirality respectively. The last ordering has mixed chirality and is called $\sqrt{3} \times \sqrt{3}$. Adapted from [15] and [16].

It is marked on each triangle whether it has positive or negative chirality. The chirality is positive if the spins rotate by 120 ° in the same direction as one traverses around the triangle, and negative if they rotate in the other direction [17].

Experimentally the $q = 0$ and $\sqrt{3} \times \sqrt{3}$ configuration is distinguished by the placement of magnetic Bragg peaks: in the $q = 0$ configuration the magnetic and structural unit cell are the same, so the structural and magnetic Bragg peaks will be at the same q-values. For the $\sqrt{3} \times \sqrt{3}$ configuration the magnetic and structural unit cell are not the same, so the Bragg peaks will differ.
Theoretically the $\sqrt{3} \times \sqrt{3}$ configuration should be favored at low temperatures [18], but studies of jarosites predominantly show the $q = 0$ configuration with positive chirality [19] [17].

If the spins in the kagomé lattice does not end up in an ordering at all, it might be classified as a spin liquid.

2.4.2 Quantum spin liquids

2D kagomé antiferromagnetic systems have the potential of being quantum spin liquids: a system with no static order and with highly correlated states, analogous to a liquid. A strict definition of quantum spin liquids is evasive in the current literature, but generally quantum spin liquids are thought of as systems with highly entangled spins and exhibiting long range correlations, but no long range order [13] [20].
Quantum spin liquids were first proposed by Phil Anderson, explained by resonating valence bonds [21].

An intriguing facet of quantum spin liquids is their theoretically predicted possibility of hosting excotic excitations with fractional quantum numbers and artificial gauge fields [13], as well as their potential use in quantum information [20].
A true quantum spin liquid is yet to be found experimentally [20], but are sought after extensively in e.g. layered kagomé structures like other types of jarosites and Herbertsmithite.

3 Jarosites

3.1 The jarosite family

Jarosites are members of the alunite supergroup of minerals ($AB_3(TO_4)_2(OH)_6$), which includes the alunite group, the beudantite group and the crandallite group. Jarosite belongs to the alunite group of sulfate minerals [22].

Jarosites have the general chemical formula $AB_3(SO_4)_2(OH)_6$, where A is a monovalent ion $A = Na^+, K^+, Rb^+, NH_4^+, Ag^+, H_3O^+, \frac{1}{2}Pb^{2+}$, and $B = Fe^{3+}, Cr^{3+}, V^{3+}$ [3]. In the referenced literature, the name 'jarosite' will usually refer to $KFe_3(SO_4)_2(OH)_6$, which is the Fe analog of alunite ($KAl_3(SO_4)_2(OH)_6$). Other minerals with 'jarosite' in their name therefore usually refer to minerals with $B = Fe^{3+}$, like natrojarosite ($NaFe_3(SO_4)_2(OH)_6$) or ammoniojarosite ((NH_4)$Fe_3(SO_4)_2(OH)_6$).

The jarosite investigated in this study is a variant of the common jarosite where the Fe^{3+} ion is replaced with Cr^{3+}, giving $KCr_3(SO_4)_2(OH)_6$, which will be referred to as chromiumjarosite, or simply Cr-jarosite.

Jarosites belong to space group $R\bar{3}m$, where R refers to the unit cell being a rhombohedral lattice system; 3 denotes that 3 two-fold rotations perpendicular to the principal axis exist; the bar indicates the existence of an inversion axis, and m refers to the existence of a mirror plane [23]. The space group also determines the reflection condition, used in both neutron and x-ray diffraction, which is $-h + k + l = 3n$, where n is an integer [17].

The lattice consists of 2D kagomé layers of the B-site ions in tilted BO_6 octahedra connected to SO_4 tetrahedra, with A-site ions between the layers. Magnetic interactions occur in the kagomé layers, where the transition metals are connected by OH groups. The jarosite crystal structure is illustrated in figure 8.
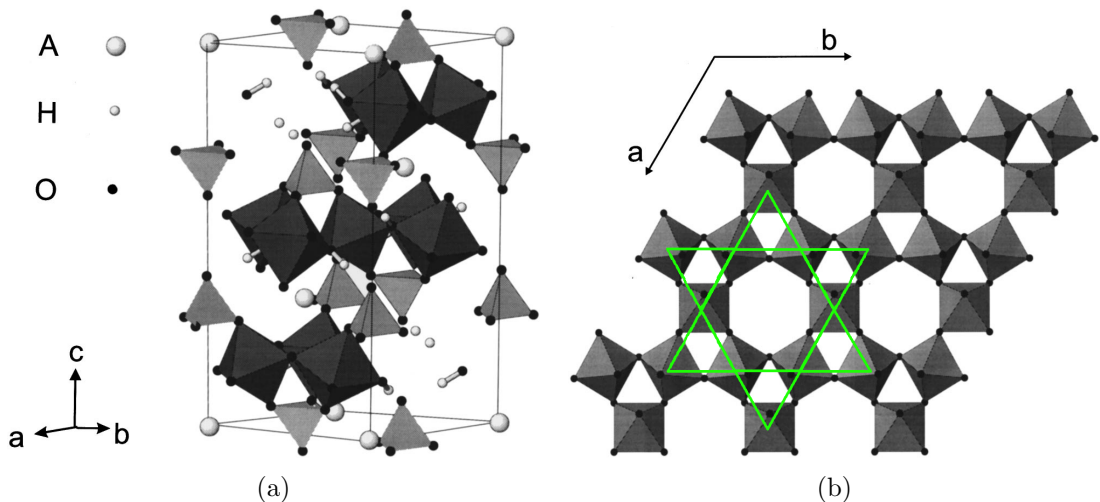
Figure 8: Crystal structure of jarosite. (a) Jarosite unit cell. B-site ions are in the middle of the octahedra, sulfur is in the middle of the SO_4 tetrahedra. A-site ions are positioned between octahedra layers. (b) Single layer of octahedra viewed along c axis, showing the kagomé pattern (green) of B-site atoms. Illustrations adapted from [24].

The kagomé lattice is structurally rigid, meaning that even if you switch the ions on the A^+ and M^+ sites, the bond lengths and bond angles are still the same (or at least very

close to the same). This means that even if we see changes in the magnetic properties between the different jarosite types, we know that this is due to phenomena in the spin physics, and not due to changes in the lattice structure.

The jarosite samples used in this study were produced synthetically in order to ensure the purity of samples, but jarosites can also be found in nature alongside other sulfate minerals. Naturally occurring jarosites are found in acidic and sulfate rich environments such as acid sulfate soils which are formed in waterlogged regions. This type of environment can be found in areas where mangrove forests have dried out, such as the coastline of Australia, but jarosites have also been found on Mars as a precipitate of depleted water deposits [25], [26]. In industrial production jarosites are found as a waste product in metal mines as a result of acid mine drainage [27].

3.2 Cr-jarosite

On the basis of Cr-jarosite being a 2D kagomé antiferromagnet, the compound is studied for its magnetic frustration and possible spin liquid behavior [20]. The magnetic ordering temperature is $T_N \approx 4K$ [17] [3].
Cr-jarosite is a $S = \frac{3}{2}$ system, which puts it somewhere between the quantum ($S = \frac{1}{2}$) and classical ($S \gg \frac{1}{2}$) limits [3]. This gives an opportunity to study what kind of phenomena exists between the two regimes.
The CrO_6 octahedra are not perfectly aligned with the ab-plane, but are each slightly tilted with respect to their neighbors, which gives rise to DM-interactions.

Cr-jarosite is much less studied than the Fe^{3+} counterpart, and only a few studies have used neutron scattering as a tool to uncover the magnetic properties [19], [17]. To the author's knowledge the use of Cr-jarosite is currently limited to academic research only.
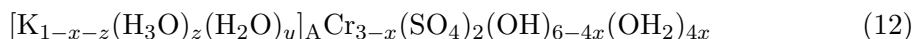
3.3 Defects

Crystallographic defects exist in many different forms, all of them being variations of atoms being added, subtracted or shifted in the crystal lattice. A vacancy is when an atom is missing from its position in the lattice. The space might then either be left empty or other atoms might substitute it.
B-site vacancies is a common defect in jarosites and B-site defects will affect the magnetic properties. The occurrence of this type of defect is described by [28], [29] and [30]. The mechanism is described by the reaction:

$$B(OH)_4O_2 + 3\,H^+ + H_3O^+ \rightarrow \square^+(OH_2)_4O_2 + H_2O + B^{3+} \tag{11}$$

$\square$ represents a B-site vacancy, shown in figure 9. In the absence of a B-site the stoichiometric B_2-OH group becomes $B-OH_2$ when the exposed OH^- groups bond to available hydrogen. An A-site defect could be the substitution of a desired A-site ion with an undesired A-site ion. The most likely substitution would be with H_3O^+ since this is present in all jarosite syntheses.

The general chemical formula for Cr-jarosite which considers possible defects is given by [29]:

$$[K_{1-x-z}(H_3O)_z(H_2O)_y]_A Cr_{3-x}(SO_4)_2(OH)_{6-4x}(OH_2)_{4x} \tag{12}$$
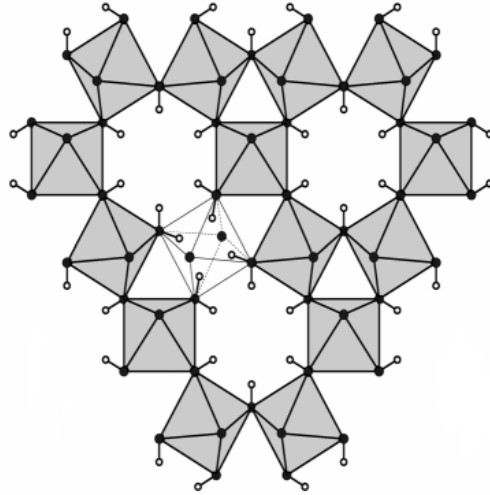
Figure 9: Illustration of a kagomé layer of jarosite with a B-site vacancy. Illustration from [30].

The square bracket subscripted by A denotes the occupants on the A-site. It is evident that if there are no defects ($x = 0$, $y = 0$, $z = 0$), the formula reduces to the chemical formula for stoichiometric Cr-jarosite. y is not related to K or Cr vacancies, indicating that water molecules can occupy the spaces between octahedral layers. x, y and z are not restricted to be integers.

4 Synthesis of Cr-jarosite

Documentation form more than 40 years of jarosite synthesis has shown that jarosites are notoriously prone to defects. This has fostered application of new and improved synthesis methods for jarosites.

The conventional way of synthesizing jarosites was by hydrothermal synthesis. As the name hints to, this method involves heating ("thermal") the reactants in an aqueous ("hydro") solution [31]:

$$3\,B_3{}^+ + 2\,A_2SO_4 + 6\,H_2O \longrightarrow AB_3(SO_4)_2(OD)_6\,(s) + 3\,A^+ + 6\,H^+ \tag{13}$$
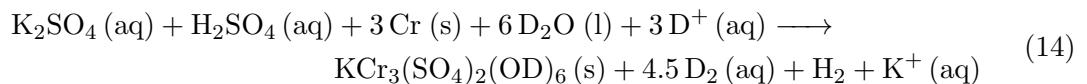
As the literature study from [32] show, table 1, this method produces varying occupancy on the B-site, and often the occupancy is not reported. Wills and Harrison (1996) [33] refer to a typical occupancy of 83-94 % for Fe-jarosites.

In 2002 a new hydrothermal synthesis method was presented by Grohol and Nocera [34] for producing vanadium jarosites $(AV_3(OH)_6(SO_4)_2$ $(A = Na^+, K^+, Rb^+, Ti^+, NH_4^+))$. Within this project this method has been applied to synthesize Cr-jarosite. This method was presented as a way to produce single crystal jarosites, but within this project the method has so far only produced jarosite powder. The key to this new redox hydrothermal method is to slowly produce $M_3{}^+$ from oxidation of metal pieces [35]. Introducing this slow redox reaction is what gives control over the precipitation process, which is crucial when trying to grow single crystals.
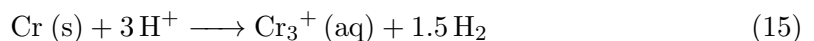
The redox hydrothermal method has proven to be a more reliable way to produce jarosites with few defects compared to the conventional method, and has effectively replaced earlier synthesis methods.

The Cr-jarosite powder is synthesized by combining pieces of chromium metal, potassium sulfate (K_2SO_4), concentrated sulfuric acid (H_2SO_4), and water. The water should be H_2O or D_2O depending on whether the powder should be hydrogenated or deuterated, respectively. The components are then placed in a hydrothermal vessel and heated.

The chemical reaction within the vessel will be (here shown for a deuterated sample):

$$\begin{aligned} K_2SO_4\,(aq) + H_2SO_4\,(aq) + 3\,Cr\,(s) + 6\,D_2O\,(l) + 3\,D^+\,(aq) \longrightarrow \\ KCr_3(SO_4)_2(OD)_6\,(s) + 4.5\,D_2\,(aq) + H_2 + K^+\,(aq) \end{aligned} \tag{14}$$

With the redox step:

$$Cr\,(s) + 3\,H^+ \longrightarrow Cr_3{}^+\,(aq) + 1.5\,H_2 \tag{15}$$

In 2011 Okuta et al. [36] presented allegedly defect free single crystals of Cr-jarosite grown by high pressure (150 MPa ≈ 1480 atm) and high temperature (450 °C) hydrothermal methods in the duration of one day. So far this promising synthesis method has not gained widespread usage.

Since this synthesis method requires highly specialized hydrothermal vessels it was not feasible to apply the method within this study.

Compound	Synthesis method	Temperature [°C]	Duration	B-site occupancy	Reference	Publication year
$KCr_3(OH)_6(SO_4)_2$ (A)	Conventional[a]	95-140	1.5-3 hours	100%	Lee et al. [19]	1997
$KCr_3(OD)_6(SO_4)_2$ (B)	Conventional[a]	95-140	1.5-3 hours	76(5)%	Lee et al. [19]	1997
$KCr_3(OH)_6(SO_4)_2$	Conventional[a]	95-140	1.5-3 hours	N/A	Townsend et al. [37]	1986
$KCr_3(OH)_6(SO_4)_2$	Conventional[a]	95-140	1.5-3 hours	N/A	Keren et al. [38]	1996
$KCr_3(OD)_6(SO_4)_2$	Conventional	280	55 hours	95.3%	Inami et al. [17]	2001
$KCr_3(OD)_6(SO_4)_2$	Conventional	300	1 week	N/A	Lengauer et al. [39]	1994
$KCr_3(OD)_6(SO_4)_2$	Conventional[b]	280	50 hours	N/A	Morimoto et al. [40]	2003
$KCr_3(OH)_6(SO_4)_2$	Conventional[b]	280	50 hours	N/A	Morimoto et al. [40]	2003
$KCr_3(OH)_6(SO_4)_2$[c]	High T	450	1 day	no defects	Okuta et al. [36]	2011
$KCr_3(OH)_6(SO_4)_2$[c]	High T	723	1 day	N/A	Okubo et al. [41]	2017
$AV_3(OH)_6(SO_4)_2$	Redox	200-205	3-7 days	100.3 ± 1.1%	Grohol and Nocera [34]	2002
$KB_3(OH)_6(SO_4)_2$[c]	Redox	200	72 hours	100 ± 1.5%	Nocera et al. [35]	2004
$AFe_3(OH)_6(SO_4)_2$	Redox	200-204	4 days	99.6 ± 0.2%	Grohol et al. [42]	2003
$AFe_3(OH)_6(SO_4)_2$	Redox	210	72 hours	100.0 ± 0.3%	Bartlett and Nocera [43]	2005

Table 1: Litterature study of synthesis methods of Cr-jarosite and related compunds. Table adapted from [32].
[a] Authors state that they follow the conventional method of Dutrizac and Kaiman [44] but do not give synthesis details, therefore the details in table is taken from article by Dutrizac and Kaiman (1976).
[b] Authors state that they follow methods of Lengauer et al. [39].
[c] Single crystals.

5 Experimental techniques

5.1 ^{2}H MAS NMR

Nuclear magnetic resonance (NMR) detects the local chemical environment of a nucleus by measuring the motion of the nuclear spins in response to an applied magnetic field. Most people will probably know the NMR technique from the field of medicine where it is used in order to map tissues in the body, and for semantic reasons the technique is these cases named magnetic resonance imaging (MRI).

^{2}H MAS NMR is a specific type of NMR where, as the name indicates, the chemical environments of deuterium (^{2}H) is studied, using a technique called magic angle spinning (MAS).

The concept behind NMR is the interaction between the magnetic moment of the nucleus of an atom and an external magnetic field.

The nuclear magnetic moment is defined from the nuclear spin, I [45]:

$$\boldsymbol{\mu} = \gamma \hbar \boldsymbol{I} \tag{16}$$

γ is the gyromagnetic ratio, defined as $\gamma = \frac{e}{2m_p} g = \frac{\mu_N}{\hbar} g$, and for deuterium this is $\gamma = 6.536 \frac{MHz}{T}$. m_p is the proton mass, g is the g-factor, and μ_N is the nuclear magneton. The g-factor is a dimensionless factor which relates the magnetic moment and angular momentum of a particle. The value of the g-factor depends on the particle or system of particles in question. The nuclear magneton is the unit used for magnetic moment of nucleons, and is defined as $\mu_N = \frac{e\hbar}{2m_p}$.

When exposed to an external magnetic field, B_0, the system experiences a Zeeman effect due to the interaction between the magnetic moment and the field. This Zeeman part of the Hamiltonian can be written as:

$$H_Z = -\boldsymbol{\mu} \cdot \boldsymbol{B_0} \tag{17}$$

From this we see that the energy will be minimized when the magnetic moment is aligned with the external magnetic field. By convention the external magnetic field is taken to be along the z direction, whereby we can write [45]:

$$H_Z = -\gamma \hbar I_z B_0 \tag{18}$$

From this we see how the Zeeman effect spits the energies due to the spin values being quantized: $I_z = m_I$, where m_I can take $2I + 1$ values, $m_I \in -I, -I + 1, ...I - 1, I$. With $2I + 1$ energy levels there is $4I$ possible transitions, since selection rules allow only $\Delta m_I = 0, \pm 1$. With the presence of an external magnetic field the magnetic moment vector precesses around the magnetic field with a frequency known as the Larmor frequency [2]:

$$\omega_0 = \gamma B_0 \tag{19}$$

Transitions between energy levels can be induced by electromagnetic waves with a frequency equivalent to the energy difference between levels, the resonance frequency. This means that the resonance frequency must be close to the Larmor frequency. Since the gyromagnetic ratio has a different value for each element, the frequency at which resonance occurs serves as a fingerprint for each element. NMR experiments use electromagnetic waves in the radio frequency (rf) range to induce transitions. As an electromagnetic

wave, the rf waves is associated with an oscillating magnetic field, $B_{rf}(t)$, applied perpendicular to B_0. The total magnetic field felt by the nucleus is thereby [45]:

$$B_{total}(t) = \boldsymbol{i}B_{rf}\,\cos(\omega_{rf}\,t) + \boldsymbol{k}B_0 \tag{20}$$

$\boldsymbol{i}$ is the unit vector along x and $\boldsymbol{k}$ is the unit vector along z. The direction of the unit vectors is determined from the NMR setup.

The basic setup for NMR experiments include a static magnetic field (3-22 T) from a superconducting magnet, and rf coils which can both emit and receive rf signals. As mentioned we define the direction of the static magnetic field as the z-axis, and the rf coils are in the xy plane.

The rf perturbations to the system are applied in pulses, or rather sequences of pulses, and the duration of the pulse determines how much the angle of the precessing spin changes. A so called 90° pulse will flip the magnetization 90° from the z-axis, meaning it will end up in the xy-plane. This is favorable since the rf coils can only pick up x and y components of the magnetization, and only x and y components take part in the precession. In principle it would be possible to produce pulses that flip the magnetization in all angles, but commonly only 90° and 180° pulses are used.

After being exposed to a rf pulse the magnetization will gradually return to its initial orientation in the positive z-direction, $\boldsymbol{M_0}$. The signal detected from the rf coils during this process is called a free induction decay (FID), illustrated in figure 10. The signal decays since the x and y components of the magnetization decrease until the magnetization is only along z. When a new rf pulse is induced, the signal goes up again.
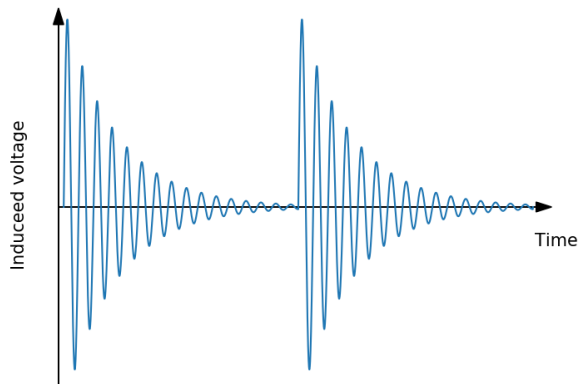

Figure 10: FID signal from two rf pulses. Oscillations correspond to Larmor precession.

The signal decay is described by two characteristic timescales called T_1, spin-lattice relaxation, and T_2, spin-spin relaxation. Spin-lattice relaxation refer to the magnetization along the z-axis returning to its initial value after being flipped by a rf pulse, illustrated in figure 11. This is in its essence just a case of having created an overpopulation of excited states which decay to the equilibrium value as soon as the rf pulse is gone. The name refers to the magnetization (i.e. spins in the system) reaching an equilibrium with it's surroundings (i.e. the lattice). Spin-spin relaxation is related to magnetization in the xy plane (transverse magnetization). Immediately after an rf pulse the phases of the transverse spins are in coherence. Inhomogeneities in the local and external magnetic

fields felt by the spins results in decoherence of the phases, which decrease the magnetization component in the xy-plane [46], [47], illustrated in figure 12.

The relaxation-effects on magnetization is described by the Bloch equations [48]:

$$
\begin{aligned}
\frac{dM_x}{dt} &= \gamma(\boldsymbol{M} \times \boldsymbol{B})_x - \frac{M_x}{T_2} \\
\frac{dM_y}{dt} &= \gamma(\boldsymbol{M} \times \boldsymbol{B})_y - \frac{M_y}{T_2} \\
\frac{dM_z}{dt} &= \gamma(\boldsymbol{M} \times \boldsymbol{B})_z - \frac{M_z - M_0}{T_1}
\end{aligned}
\tag{21}
$$

The cross products correspond to Larmor precession, so if we consider the expressions in a rotating frame these terms disappear since B_0 is no longer considered [47].
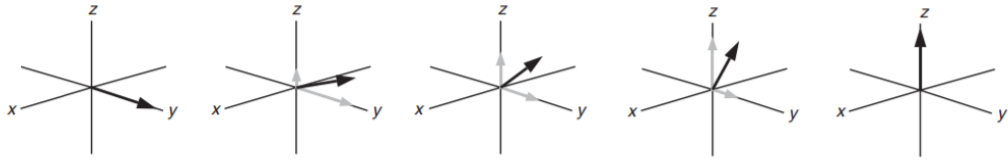

Figure 11: Illustration of T_1 relaxation in the rotating frame. After the rf pulse the magnetization vector recovers to be oriented along the z-axis. From [47].
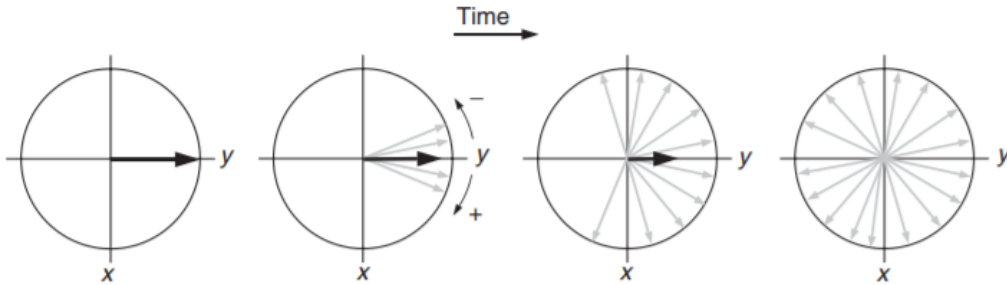

Figure 12: Illustration of T_2 relaxation in the rotating frame. Local and applied field inhomogeneities cause the spins to precess with different frequencies, reducing the total xy-plane magnetization. From [47].

Combining different rf pulses in specific sequences is a way to gain more information about the system, e.g. measuring T_1 and T_2 of a sample. T_1 can be measured through inversion recovery, T_2 is measured through spin-echo. Inversion recovery use a $180° \rightarrow \tau \rightarrow 90°$ pulse sequence, where τ denote the delay time between pulses. First $\boldsymbol{M_0}$ is flipped so it lies along the $-z$ direction (180° pulse), and will begin to relax back to its initial position along $+z$. After a short amount of time, τ, a 90° pulse is applied in order to flip the magnetization to the xy-plane, where the signal can be detected. Using this sequence with different delay times yield information about how far along the longitudinal relaxation process has come during as function of τ, whereby T_1 can be extracted.

The spin-echo sequence was developed by E. L. Hahn in 1950 (why it is sometimes

called a Hahn echo) [1]. The sequence is $90° \rightarrow \tau \rightarrow 180° \rightarrow \tau$, where τ is the echo time. First $\boldsymbol{M_0}$ is flipped to the xy-plane (90° pulse), where the individual spins will begin to dephase. After some time, T_E (the echo time), the spins are flipped 180°, still being in the xy-plane. Waiting the same amount of time after the flipping, τ, will cause the spins to get back to their phase coherence state, just now flipped by 180°. This cancels out contributions from inhomogeneities in the external magnetic field, but not the microscopic contributions from the local spin environment. In this way the 'true' T_2 can be extracted, since it is the characteristic time of the microscopic phase decoherence from the local magnetic field [47].

Spin-echo is also used in order to get better signal from the experiment. Since we get an echo of when the signal is strongest (right after 90° flip), more signal is recorded per unit of time in this type of sequence. This is especially important since receivers often have a dead time in which they cannot record any signal. This dead time occurs right after the rf pulse is emitted (the receiver is usually also a rf pulse transmitter), when the FID signal has the highest amplitude, and can last from 5-100 μs. Depending on the duration of the FID signal, the dead time might introduce a significant loss of information. An echo therefore yields a second opportunity to record the initial part of the signal. For single pulses the problem with dead time is overcome by having a receiver with a short dead time, compared to the duration of the FID signal.

Each spin-echo sequence can produce multiple echos, if we wait τ after the first echo, apply a 180° pulse, and wait T_E again, a second echo will be produced. Every time a new echo is produced the signal intensity is a bit lower, since relaxation is still occurring throughout this process. For solid state NMR we have the relation $T_1 \gg T_2$ (with $T_1 \geq T_2$ for liquid NMR) [46].

So far we have only looked at the effect of the external magnetic fields B_0 and B_{rf}, but there are phenomena within the atom that affect the effective magnetic field felt by the nucleus. The type and strength of these effects are all related to the chemical environment of the atom, and this is the exact reason why NMR is useful.

As mentioned above, each element should in principle resonate with one characteristic frequency. But as it turns out, there is a number of effects which can change the resonance frequency of a molecule. Those of most importance to this project will be explained below.

5.1.1 Chemical shift

When an atom is exposed to a magnetic field, the nuclear spins are affected, as we know. But the electrons respond to the external field as well. The external field causes the electrons to circulate around the atom, and these circulating currents produce a small internal magnetic field which can add or subtract from the external field, changing the effective field felt by the nucleus [50], [45].

The nucleus is said to be 'shielded' from the external field by the electrons. The number of electrons determines the strength of the shielding effect. Since different chemical environments have different electron densities, the effective magnetic field felt by the nucleus will differ slightly in different compounds. The measured nuclear response to the field now yield several resonance frequencies, each corresponding to a certain type of chemical environment.

---

[1] The original Hahn echo is a $90° - 90°$ sequence [49] , but nowadays most authors use spin-echo and Hahn echo almost synonymously, although spin echo is more common.

If the electron distribution (and thereby the shielding effect) was spherically symmetric, it could be described by one number, since the magnitude would be the same in all directions. But since most electron distributions are not spherically symmetric, a shielding tensor, $\boldsymbol{\sigma}$, is used to describe the shielding effect. It can be favorable to express the shielding tensor in a frame of reference that fits the shape of the electron distribution. This can be pictured by imagining the electron distribution as an ellipsoid, with the principal axis of the ellipsoid defining one of the axis in this frame of reference, illustrated in figure 13. For this reason this frame of reference is called the principal axis frame (PAF). The PAF can be related to the lab frame of reference (where B_0 is along z) by the angles: θ, which relates to the z-axis, and ϕ, which relates to the xy plane. Since we normally only consider effects in the direction of the magnetic field, only θ will be of importance to describe the system [45].

The contribution to the resonance frequency from chemical shielding can be calculated by [45]:

$$\omega_{\text{cs}}(\theta) = -\omega_0 \sigma_{\text{zz}} \frac{1}{2}(3\cos^2(\theta) - 1), \tag{22}$$

where ω_0 is the Larmor frequency, i.e. what the resonance frequency would be if there was no shielding effects, and σ_{zz} is the z component of the shielding tensor, measured in ppm [51].

In order to determine the different chemical environments for one type of element in a sample, the experiment needs to be calibrated with a sample of said element in a well known chemical environment. The so called chemical shift is calculated by:

$$\delta = \frac{\nu - \nu_{\text{ref}}}{\nu_{\text{ref}}} \tag{23}$$

where ν is the frequency of that element in the sample and ν_{ref} is the frequency from the reference compound [45].

5.1.2 Quadrupolar coupling

Nuclei with spin $I > 1/2$ have an ellipsoid charge distribution, as opposed to the spherical charge distribution of spin $I = 1/2$ or $I = 0$ nuclei. This asymmetric charge distribution is described by the nuclear electric quadrupole moment (eQ). The quadrupole moment interacts with the electric field gradient of the atom (electron density distribution) and its surroundings, an interaction which is called the quadrupole coupling [52]. The quadrupole Hamiltonian which describes the interaction between the nuclear electric quadrupole moment and the electric field gradient can be written as [45] :

$$\hat{H}_Q = \frac{eQ}{6I(2I-1)\hbar} \boldsymbol{I} \cdot e\boldsymbol{q} \cdot \boldsymbol{I} \tag{24}$$

e is the proton charge, Q is the nuclear quadrupole moment, and $\boldsymbol{q}$ is the electric field gradient. The size of Q is related to the asymmetry of the nuclear charge distribution and determines the strength of the quadrupolar interaction.

For a nucleus in an applied field the effect of the quadrupolar coupling on the resonance frequency is given by (to first order) [45]:

$$\omega_{\text{Q}}(\theta) = \omega_0 - \frac{3}{8}\left(\frac{2m-1}{I(2I-1)}\right)\chi(3\cos^2(\theta) - 1), \tag{25}$$
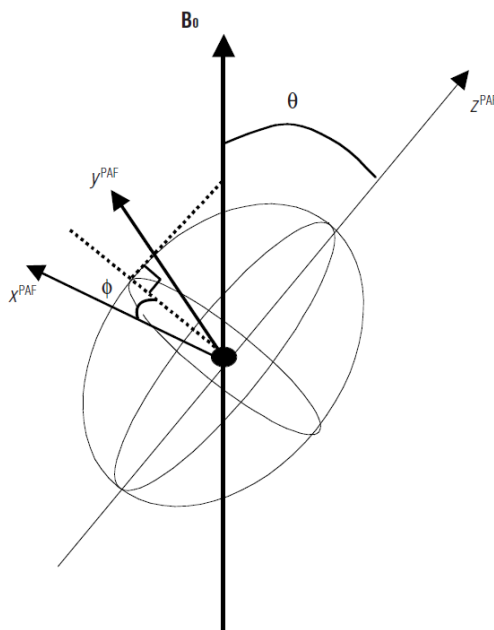
Figure 13: Illustration of the orientation in the principal axis frame (PAF). Illustration from [45].

where ω_0 is the resonance frequency without the effect of quadrupolar coupling, $\chi = \frac{e^2 q_{zz}^{PAF} Q}{\hbar}$ is the quadrupole coupling constant where q_{zz}^{PAF} is the z component of the electric field gradient tensor expressed in the principal axis frame [45], and I and m are the quantum numbers for the affected state $|I, m>$.

It is reasonable to use the quadrupolar coupling only to first order to describe deuterium, since the quadrupolar coupling constant/electric quadrupole moment of deuterium ($\sim$KHz) [53], [54] is small compared to the Larmor frequency ($\sim$MHz) [55].

Just like with the chemical shift anisotropy, the quadrupole coupling has a $3\cos^2(\theta) - 1$ dependency. This term is responsible for the lineshape and broadening effects seen in solid state NMR spectra. The following section presents an experimental technique called magic angle spinning which counteracts these effects.

5.1.3 Magic angle spinning

In solution NMR the effects of anisotropies from nuclear interactions is averaged out due to random tumbling of the molecules in the solution. This produces NMR spectra with sharp resonance peaks.

With solid state NMR we are not so lucky. The nuclear interactions broadens and distort the resonance peaks to such an extent that they fuse together and become unrecognizable broad humps.

The solution to this is a technique known as magic angle spinning. The "magic" of the magic angle is that it produces solution-like spectra from solid state NMR. As formerly explained, the chemical shift anisotropy and quadrupolar coupling effects are proportional to $3\cos^2(\theta) - 1$, and at a certain angle, the so called magic angle at $54.74°$, the term becomes zero and the anisotropic effect vanishes.
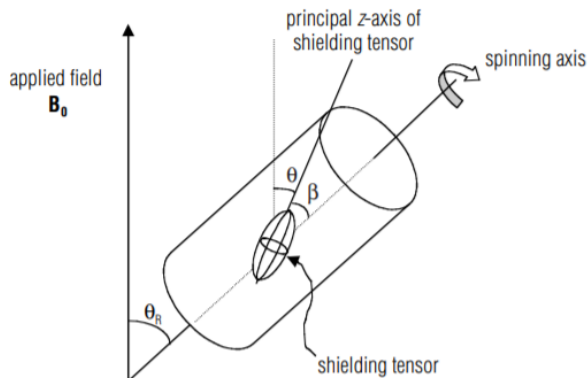
Figure 14: Schematic drawing of a MAS experiment setup. The sample is packed in a cylindrical rotor which is spun around an axis oriented at the magic angle ($\theta_R = 54.74°$), with respect to the applied field. Illustration from [45].

Spinning the sample around an axis which is tilted θ_R with respect to B_0, leads to θ varying with time, figure 14. The effect of spinning is calculated as the time average of $3\cos^2(\theta) - 1$, which is shown to be [56]:

$$\langle 3\cos^2(\theta) - 1 \rangle = \frac{1}{2}(3\cos^2(\theta_R) - 1)(3\cos^2(\beta) - 1), \tag{26}$$

where β is the angle between the spinning axis and principal axis of the shielding ellipsoid. The expression is zero when θ_R is set to 54.74° .

The effect of MAS is illustrated in figure 15 for a glycine powder sample. Note that in order to get the best resolution it is not enough to just use MAS, but the spinning must be fast as well.

Figure 15 d) show how MAS has transformed the broad peaks from the static signal to multiple resonance peaks which follow the same overall shape from the static signal. Not all these peaks are genuine resonance peaks, most ot them are what is referred to as spinning sidebands. These are 'shadows' of the static anisotropic signal, spaced by the spinning speed frequency from the primary peak. By spinning the sample at higher frequencies the spinning sidebands are spaced out, in the end leaving only the primary resonance peak if spun at sufficiently high frequencies [45].

Although MAS greatly reduces the effect of the chemical shift anisotropy and quadrupolar coupling it does not remove the effects completely. Although it might look promising to first order, higher order terms of the quadrupolar coupling will not be averaged to zero [45].

Figure 14 illustrates the experimental setup for MAS. The sample is packed tightly in a cylindrical sample holder, placed at the magic angle relative to the external field, and spun at 1-100 kHz frequencies. The sample holder is made from a ceramic material (typically zirconia, ZrO_2 or silicon nitride, Si_3N_4) in order to withstand the friction heat from spinning.

An example of a ^2H MAS NMR spectrum can be seen in figure 16 of deuterated sodium acetate, CD_3COONa. The x axis is a measure of the chemical shift in units of parts per million (ppm). The resonance of the reference compound ($Si(CD_3)_4$) is set to 0 ppm, and any resonances from the sample is measured relative to the reference compound. The
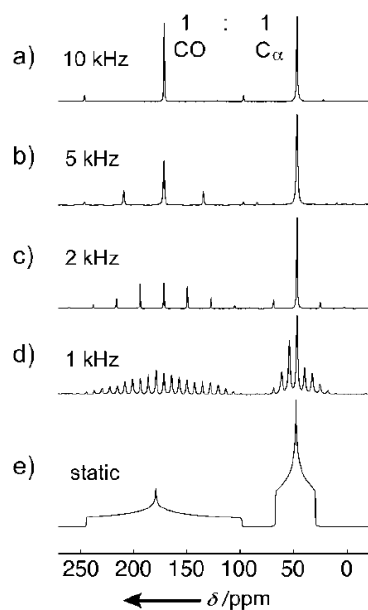
Figure 15: Effect of magic angle spinning on a glycine powder sample. e) show the static case (no MAS) where the resonance lines are broadened. d)-a) show the spectra with MAS at increasing spinning speeds, which increase the resolution (fewer spinning sidebands). Figure from [50].

chemical shift is measured in ppm relative to the reference compound in order to get a standardized measure of the chemical shift which is not dependent on the spectrometer frequency, which it would otherwise be if the chemical shift was shown in units of Hz.

Deuterated tetramethylsilane $Si(CD_3)_4$ is used as reference compound in most ^{2}H MAS NMR. In this compound, all deuterium atoms have the same chemical environment, so there is only one resonance, which is set to $\delta = 0$ ppm.

From the spectrum in figure 16 the primary resonance peak is the one with the highest intensity (this is not always the case, but for this spectrum it is), marked by a *. The spinning sidebands are the peaks with gradually lower intensity, evenly spaced prom the primary peak. The peaks at lower intensities are resonance peaks (and associated spinning sidebands) from defects in the sample.

The isotropic chemical shift is found as the ppm value of the primary peak. In order to find the primary peak one can superimpose two NMR spectra of the same sample recorded at different frequencies. The primary peak is the one that does not chance position (only spinning sidebands shift as function of spinning frequency), so in the case of figure 16 the chemical shift is around 1 ppm.

^{2}H NMR spectra were recorded on a JEOL 500 MHz NMR spectrometer with a 11.7 T Oxford Magnet. The sample holder is a 3.2 mm MAS NMR probe made of zirconia.
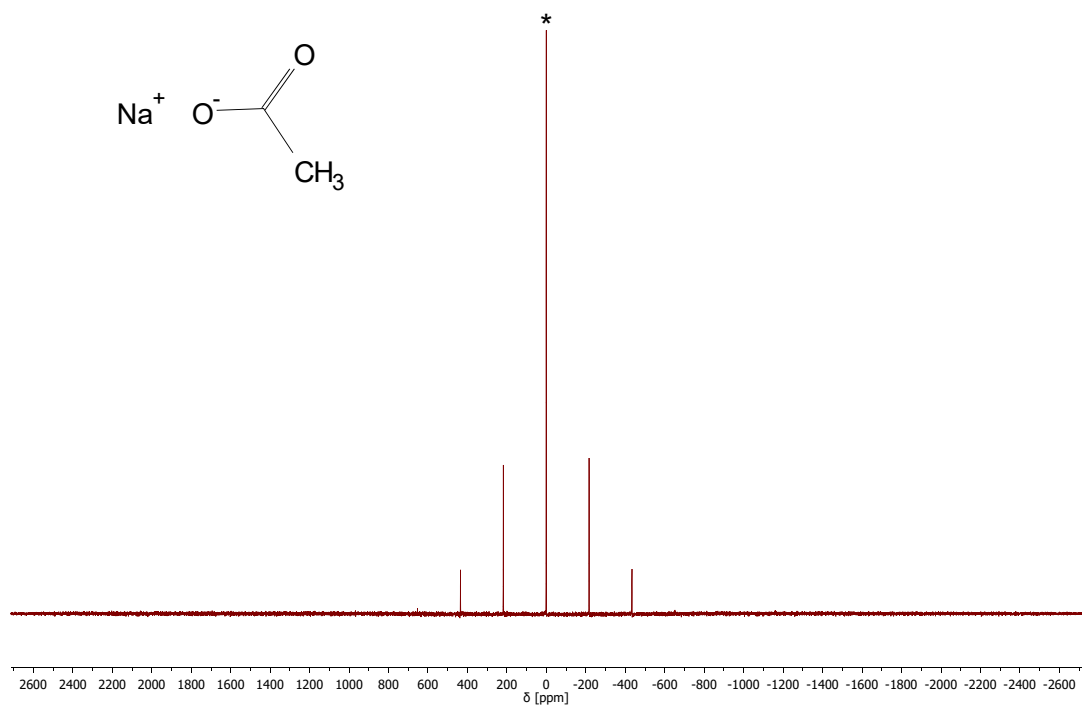A picture of the NMR instrument can be seen in figure 17.

Figure 16: NMR spectrum of deuterated sodium acetate (CD$_3$COONa) at 21 kHz. The chemical shift at 1 ppm is marked by *. The chemical structure of sodium acetate is shown on the left-hand side.

Figure 17: The JEOL 500 MHz NMR spectrometer with a 11.7 T Oxford Magnet at SDU, which has served as the primary NMR instrument for this study.

5.2 Thermogravimetric analysis

Thermogravimetric analysis (TGA) is a form of thermal analysis where the sample is gradually heated whilst the mass of the sample is measured. Depending on the constituents of the sample, the sample will decompose at specific temperatures. Decomposition is observed as a mass loss from which the chemical composition can be inferred. The disadvantage of TGA is that the sample is destroyed during measurement. Luckily only a relatively small amount of sample (10-30 mg) is needed to perform the analysis.

Approximately 30 mg sample is placed in a thermocouple inside a ceramic furnace. A thermocouple is made from thermoelectric materials in order to utilize the thermoelectric effect to measure the temperature of the sample [57]. A constant flow of nitrogen gas is heated by an electric heating element, thereby heating the furnace much like a convection oven. Time, mass and temperature are continuously recorded during the process.
Samples were heated from 35°C to 900°C, at a rate of 10°C per minute. With this type of program, TGA measurements usually last a few hours.
The temperature is recorded in two places: at the heating element and at the thermocouple which contains the sample.

Experiments were performed on a PerkinElmer TGA 4000 machine at SDU. This instrument use a top-loading pan balance system to measure the sample mass. The balance system has a precision of 0.01%, and a capacity of up to 1500 mg sample [57].

5.3 Infrared spectroscopy

Infrared spectroscopy (IR) is an experimental technique used to determine functional groups in molecules and solids. If a molecule is exposed to infrared radiation, absorption occurs if the IR frequencies match the vibrational modes of the chemical bonds within the molecule. The molecular structure can therefore be inferred from the IR spectrum. In this thesis IR is used in order to identify that the correct functional groups are present in the jarosite samples, namely the OH-groups.

Molecules consist of two or more atoms which are bound together by their electrons in chemical bonds. The atomic nuclei are separated by some distance, determined by the sum of forces between atoms. The classic description of molecular motion is to imagine the atoms as point particles tied together by springs. The easiest describable system is a diatomic molecule, which are a reasonable approximation for the OH-groups in the jarosite structure. This system can be described as a simple harmonic oscillator, with the atoms vibrating around their equilibrium state. The system can classically be modeled by Hooke's law: $F = -kx$, where F is the force between the atoms, x is the displacement from the equilibrium position, and k is the 'spring' constant. The sign is negative since the restoring force acts in the opposite direction of the displacement. This simple classical model is nice but do not suffice to fully describe the behavior of atoms. For this we need quantum mechanics, namely the quantum harmonic oscillator described by the Schödinger equation. Quantum mechanics explore the wave/particle duality of particles, which are described by wavefunctions ψ. The one-dimensional Schödinger equation for a diatomic molecule is given by [58]:

$$-\frac{\hbar}{2m_{\text{eff}}}\frac{d^2\psi}{dx^2} + \frac{1}{2}m\omega^2 x^2\psi = E\psi \tag{27}$$

$m_{\text{eff}} = \frac{m_1 m_2}{m_1 + m_2}$ is the effective mass (reduced mass) of the system, x is the displacement, $\omega = \sqrt{\frac{k}{m_{\text{eff}}}}$ is the angular frequency of the harmonic oscillator, and E is the energy. This system can be solved exactly, revealing quantized energy levels given by the energy eigenfunctions:

$$E_n = \hbar\omega\left(n + \frac{1}{2}\right), \tag{28}$$

where $n = \{0, 1, 2, 3...\}$. The energy levels are illustrated in figure 20a.

Transitions between these energy levels can only occur when the system is exposed to a source of energy which match the energy interval between levels $\Delta n = \hbar\omega$. The frequency of molecular vibrations are approximately in the order 10^{13} Hz, which corresponds to electromagnetic radiation in the infrared range, $10^{11} - 10^{15}$ Hz (1 meV $\approx 2.4 \cdot 10^{11}$ Hz). Infrared radiation can only probe a vibrational state if the system is infrared active, which require that the molecule has a dipole moment [58]. A molecule has a dipole moment if its electron distribution is asymmetric, that is to say it is polarized.

The selection rule for transitions in molecular vibrations can be found by analyzing the transition dipole moment for the one-dimensional harmonic oscillator, yielding the restriction $\Delta n = \pm 1$ [58]. Put into words, that means that only transitions to the neighboring energy level are allowed.

In the IR spectrometer the sample is exposed to an array of frequencies, typically in the range 10^{13}Hz to 10^{14}Hz. Frequencies which correspond to molecular vibrational modes are absorbed by the sample and the remaining array of frequencies is recorded by the spectrometer. This leaves a frequency spectrum with absorption bands corresponding to the molecular bonds in the sample.

IR spectra show the intensity of the absorption peaks as function of wavenumber $\bar{\nu}$ $\left(\bar{\nu} = \frac{1}{\lambda} = \frac{frequency}{c}\right)$ in the units cm^{-1} (1 meV ≈ 8 cm^{-1}). An example of an IR spectrum is shown in figure 18.

IR spectra can roughly be divided into two regions: the fingerprint region (< 1500cm^{-1}) and the functional group region (≥ 1500cm^{-1}) [31]. The fingerprint region contains many absorption bands and is normally not analyzed in great detail but is rather used to compare with reference compounds, since the multitude of peaks often hinders precise identification of each individual vibration. Functional groups are groups of atoms within a molecule which are responsible for characteristic chemical properties independent of the specific molecule they are attached to. For Cr-jarosite the relevant functional group are OH-groups.

Molecular vibrations exist in many different forms with the most common types being stretching and bending. A stretching vibration can be imagined as the bond behaving like a spring between two atoms which oscillate lengthwise. A bending vibration is when the angle between two bonds is changing. The principle of stretching and bending is illustrated in figure 19. Following the terminology of [60] and [59] stretching vibrations are denoted by $\nu(X)$ and bending vibrations by $\delta(X)$. Subscripts come from the classification of symmetries within group theory and are used to denote whether the motion is symmetric (1) or antisymmetric (2) [60].
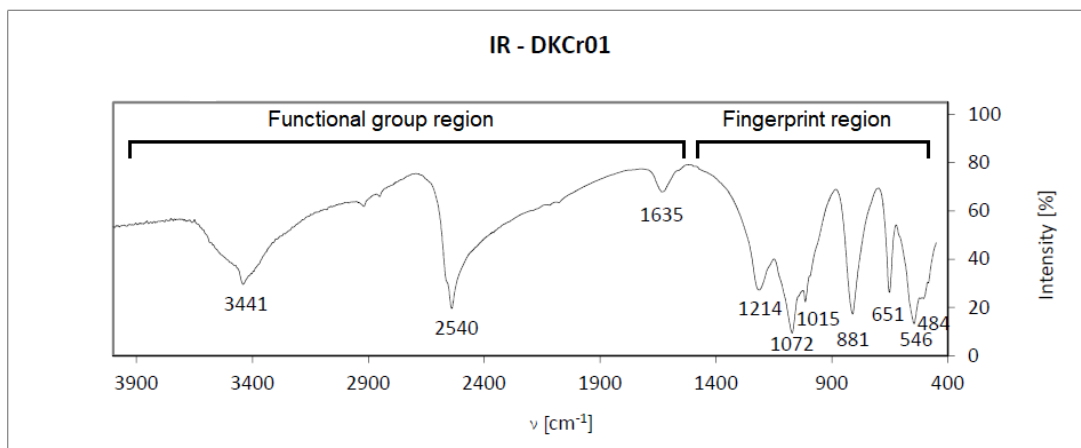
Figure 18: Example of an IR spectrum. This spectrum is from [59] for a deuterated Cr-jarosite sample. The extent of the functional group region and fingerprint region is indicated. Peak positions are given in the bottom of each peak.
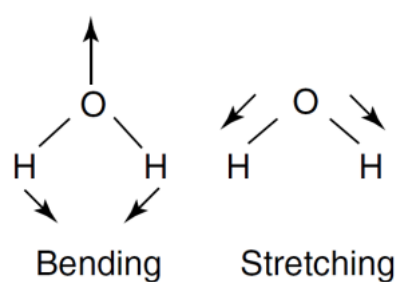

Figure 19: Illustration of bending and stretching vibrations in a water molecule. Figure adapted from [61].

28

Table 2 shows the possibly relevant IR absorption bands for Cr-jarosite.

IR absorption bands	
Assignment	$\bar{\nu}$ [cm^{-1}]
$\nu(H_2O)$	~ 3550
$\nu(OH)$	$3300 - 3500$
$\nu(OD)$	~ 2500
$\delta(H_2O)$	$1625 - 1645$
$\delta(H_3O^+)$	~ 1580
$\nu_2(SO_4^{2-})$	$1050 - 1230$
$\delta(OH)$	$1005 - 1028$
$\nu_1(SO_4^{2-})$	$990 - 1030$
$\delta_2(SO_4^{2-})$	$623 - 670$
$\delta_1(SO_4^{2-})$	$404 - 438$

Table 2: Common IR absorption bands of alunite-group minerals. Based on data from [62], [60], [63] and [59]. ν indicate a stretching mode, δ indicate a bending mode.

The one-dimensional harmonic oscillator model is a nice and simple way to describe molecular vibrations. But evidently, there is some aspects where the model falls short. One essential shortcoming is that the model does not include dissociation of molecules. The restoring force is not always proportional to the displacement since the chemical bond can only be stretched so far before it breaks. This behavior is best described as an anharmonic oscillator, illustrated in figure 20b. This type of anharmonic potential is also referred to as a Morse potential [58].

The energy levels of this system are given by [58]:

$$E_v = \hbar\omega \left(n + \frac{1}{2} \right) - \frac{\left(\hbar\omega \left(n + \frac{1}{2} \right) \right)^2}{4D_e} \tag{29}$$

D_e is the dissociation energy, i.e. the required energy to break the diatomic bond. Compared to equally spaced energy levels of the harmonic oscillator, the negative term ensures that the distance between energy levels grow smaller at higher energies, converging as they reach the dissociation energy.

The selection rule for the harmonic oscillator model is not applicable in the anhamonic case. Although $\Delta n = \pm 1$ transistions might be the most common $\Delta n = \pm 2, \pm 3, ...$ are equally allowed. Transitions with $|\Delta n| > 1$ are called overtones and are seen in the spectra as low intensity absorbtion bands. Overtones bands from small Δn are observed at approximately integer multiples of the $n = 0 \rightarrow n = 1$ transition, so the first overtone is observed at approximately two times the original wavenumber etc.

Overtone bands are not illustrated in the example spectra, but they appear in the IR spectra for the samples.

IR measurements were performed on a Perkin Elmer Spectrum 65 FT IR Spectrometer at SDU.
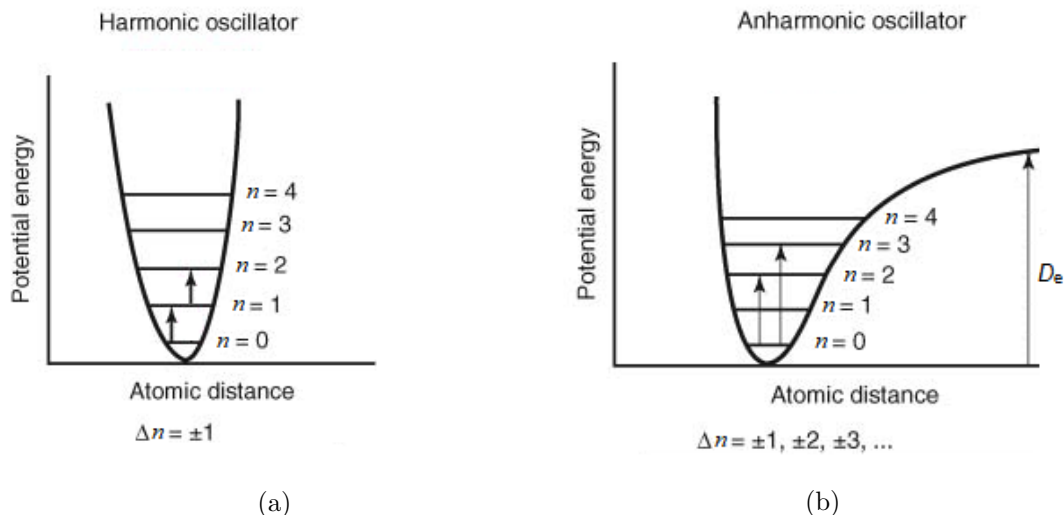
Figure 20: Drawing of the harmonic an anharmonic oscillator potentials, adapted from [64]. v refer to the energy level. Selection rules are given by Δv for each case. In (a) there is equal distance between energy levels, whereas for (b) the distance decrease as the energy levels converge towards the dissociation energy, D_e.

5.4 Powder x-ray diffraction

Powder x-ray diffraction (PXRD) is a commonly used characterization technique which is both quick and inexpensive: PXRD instruments are standard equipment in most chemistry laboratories, and preparation and measurements can usually be performed within an hour. Furthermore, PXRD is non-destructive, meaning that the sample can be reclaimed after measuring.

X-ray diffraction utilize Bragg scattering of x-rays from the lattice planes in the sample. From Bragg's law, we can relate the scattering angle to the distance between lattice planes:

$$2d\sin(\theta) = n\lambda \tag{30}$$

d is the distance between lattice planes, λ is the wavelength, n is an integer and θ is the angle marked on figure 21. The scattering angle is normally referred to as 2θ.
In a powder, all lattice planes are observed since the powder grains will be randomly oriented.
Figure 21 illustrate the concept of Bragg's law. The waves make constructive interference when their path difference is $n\lambda$. On the diffraction spectra this is seen as high intensity peaks. The resulting diffraction pattern will be characteristic for the material in question. The diffraction pattern is compared to crystallographic tables and/or databases in order to characterize the material in the sample.

X-rays occupy the space in the electromagnetic spectrum between ultraviolet radiation and gamma rays, having a wavelength of $\sim 1\,\text{Å}$ ($10^{-10}\,\text{m}$), corresponding to energies in the order of keV.
X-rays are produced when accelerated electrons hit a metal target. Inside a vacuum tube, a hot cathode (usually a tungsten filament) releases electrons due to thermionic
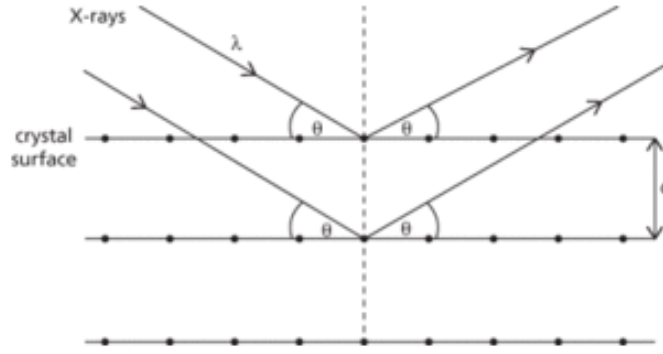
Figure 21: Illustration of Bragg's law, from [65].

emission. The electrons are accelerated towards an anode by applying an electric potential of ~ 30 kV. The accelerated electrons have enough energy to knock off an electron from the inner shell of the anode atoms. When this is done, an electron from one of the outer shells will occupy the lower energy level thereby releasing energy in the form of a photon. The wavelength of the released photon is characteristic of the anode material. In powder x-ray diffraction (PXRD) instruments the anode is typically made of copper. For copper the knocked off $1s$ electron is replaced by an electron from the $2p$ or $3p$ orbital, named the $K\alpha$ (1.5418 Å) and $K\beta$ (1.3922 Å) transition respectively. The $K\beta$ transition happens rarely compared to the $K\alpha$ transition, which shows as a much lower intensity in the spectrum. The $K\alpha$ transition is in fact a doublet, consisting of $K\alpha_1 = 1.5405$ Å and $K\alpha_2 = 1.5443$ Å. The doublet exists as a result of the energy difference between the two different spin states [31].

Apart from the characteristic x-rays all x-ray emission spectra contain a continuum of wavelengths from bremsstrahlung, which is when an electron radiates a photon as a result of decelleraton when deflected by another charged particle. The continuum has lower intensity than the characteristic x-rays and is not used in the x-ray spectroscopy process.

PXRD spectra provides information about the bulk sample, since multiple crystal planes contribute to the diffraction pattern, as opposed to the local information one gets from x-ray crystallography on a single crystal.

Diffraction can be performed with neutrons as well, but in most cases x-rays is far more practical. X-rays interacts with the electron cloud of the atoms in the material, as opposed to neutrons which interact with the nuclei. This makes x-rays less sensitive of lighter atoms.

The advantage of neutron diffraction is that it can probe the magnetic structure, since neutrons have a magnetic moment. Unlike the structure of the lattice, the magnetic structure change as a function of temperature. Using neutron diffraction, i.e. elastic neutron scattering, while varying the temperature of the sample will therefore reveal the magnetic Bragg peaks. The subject of neutron scattering will be discussed further in section 5.7.

The most straightforward method of analyzing PXRD spectra is by comparing them to a reference spectrum. Discrepancies in peak placement and intensity between the two spectra will be a telltale sign of defects in the sample, provided that the given ref-

erence spectrum is a good representation of the stoichiometric compound.

A less straightforward way of analyzing the spectra is by a method called Rietveld refinement. This is where a theoretical peak profile is fitted to the spectrum using a non-linear least squares algorithm. In the least squares method, the squared difference between the measured and predicted values are sought to be minimized by varying the parameters one wishes to estimate. For non-linear problems, this process is iterative and requires input parameters which are fairly close to the 'true' value [66]. Rietveld refinement can therefore not be used 'blindly', and to be fair, few techniques can, but it can be powerful when you have at least approximate knowledge of the sample you wish to investigate. Rietveld refinement yield estimated parameters about the sample structure, such as lattice parameters and defects.

The spectra were recorded using a Rigaku MiniFlex PXRD instrument. The analysis was performed with the PXRD data analysis program PDXL 2 and reference spectra was found in the related database.

5.5   Scanning electron microscopy

Scanning electron microscopy (SEM) measurements of the sample was performed and provided thanks to Dr. Tae-Hyun Kim, University of Southern Denmark.

SEM uses a focused electron beam to probe the surface of a sample in order to produce detailed images of the surface. In a scanning electron microscope (likewise abbreviated as SEM) an electron gun, made from a heated cathode filament, produces a beam of electrons which is focused through a series of lenses to a beam width of a few nanometers. The basic setup in a SEM is illustrated in figure 22.

In order to prevent buildup of surface charge when scanning samples, non-conductive samples are coated with a thin layer (5-15 nm) of conductive material such as gold [67].
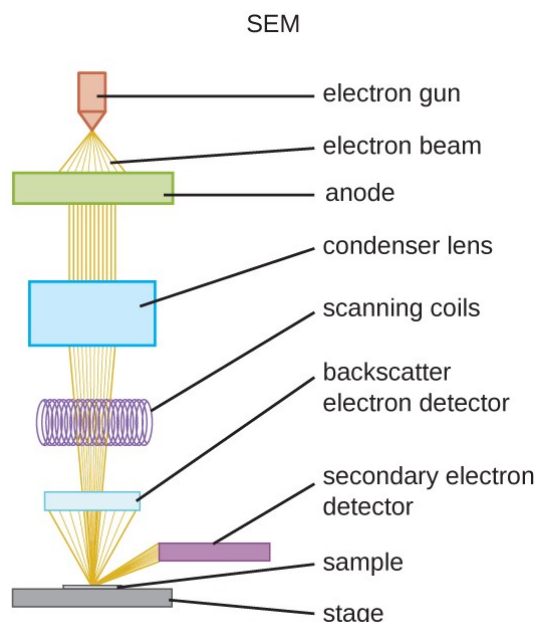

Figure 22: Schematic illustration of a SEM setup, from [68].

The scattering which occurs when the electron beam hits the sample is a combination

of secondary electrons, back-scattered electrons and characteristic x-rays. It is primarily the secondary and to a smaller degree back-scattered electrons which contribute to the topographic images of the sample surface. Secondary electrons stem from inelastic scattering where electrons are ejected from within the atoms in the sample as a result of kinetic energy transfer from collision with electrons from the beam. Secondary electrons originate from the immediate surface layer (5-50 nm) and by backtracking the scattering path from detector to sample the surface topology can be inferred. Back-scattered electrons are elastically scattered from 50-300 nm within the sample and can provide information about the composition contrast of the sample, whereas characteristic x-rays gives information about the elemental composition [67].

5.6   Energy-dispersive x-ray spectroscopy

Energy-dispersive x-ray spectroscopy (EDS) measurements of the sample was performed and provided thanks to Dr. Tae-Hyun Kim, University of Southern Denmark.
EDS is a technique for chemical analysis which detects the elemental composition of the sample. The sample is exposed a beam of electrons which can eject en electron from an inner shell of an atom in the sample. The hole left by the ejected electron will be filled by an electron from an outer shell, emitting energy in the form of a photon in the process. The emitted photons from this process are known as characteristic x-rays since their energy depends on the atomic structure from which they are emitted, and the observed x-ray spectrum is therefore a representation of the elemental composition [67].
EDS instruments are typically an integrated part of other machinery such as electron microscopes.

5.7   Neutron scattering

Neutron scattering is a tool used in solid state science, used in order to reveal the inner 'workings' in the sample of interest. Neutron scattering is closely related to the similar and more common technique of x-ray scattering, and since neutron scattering facilities is much more rare and expensive than their x-ray counterparts one should only opt for neutrons when other methods are insufficient.
Like x-rays, neutrons can be used to obtain structural information about solids. But unlike x-rays, which is photons interacting with matter through the electrons of an atom, neutrons interact only with the nucleus of the atom. The use of neutrons therefore enables study of isotopic effects, facilitate study of the bulk sample and allow for samples to be stored in a wide array of environments during experiments due to the high permeability of neutrons [11]. But the most unique aspect of neutrons, or at least the most useful regarding this thesis, is their ability to probe the magnetic properties of materials, due to their magnetic moment. Elastic magnetic scattering yields information about the lattice and magnetic structure (statics) in the sample, where inelastic magnetic scattering yields information about magnetic excitations (dynamics) [69].

Neutron experiments are performed at large neutron scattering facilities, where neutrons are produced either from nuclear fission or from spallation. This is referred to as a reactor source and spallation source, respectively. Reactor sources provide a continous steady beam of neutrons, where spallation sources provides pulses of neutrons.

In nuclear fission neutrons are released as a byproduct of the fission process. Research reactors are smaller than the nuclear reactors used in nuclear power plants and similarly use ^{235}U as fuel source, although the enrichment level may vary depending on the purpose. When the uranium in the reactor is inflicted with neutrons from a neutron source such as ^{252}Cf (spontaneous fission), the following fission process will be [11], [70]:

$$^{235}\text{U} + n \rightarrow \text{D}_1 + \text{D}_2 + 2\text{--}3\,n + Q \tag{31}$$
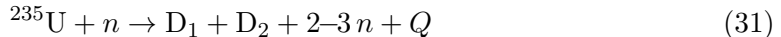
The uranium splits into daughter products, and in the process releases on average 2.7 neutrons and energy $Q \approx 200$ MeV [70], [69]. The released neutrons then go on to continue the chain-reaction within the reactor, but for the purpose of research reactors the excess neutrons provide the neutron source for scattering experiments.

Spallation sources function by accelerating protons to bombard a heavy metal target, e.g. tantalum or tungsten, thereby producing neutrons by splallation. The term spallation generally describes how fragments is ejected from a material due to an impact. For nuclear physics purposes the term is used to describe the process where a heavy nuclei is injected with a high energy proton which initiates an intranuclear cascade followed by evaporation: emission of 20-30 neutrons [69]. Figure 23 illustrates the spallation process.
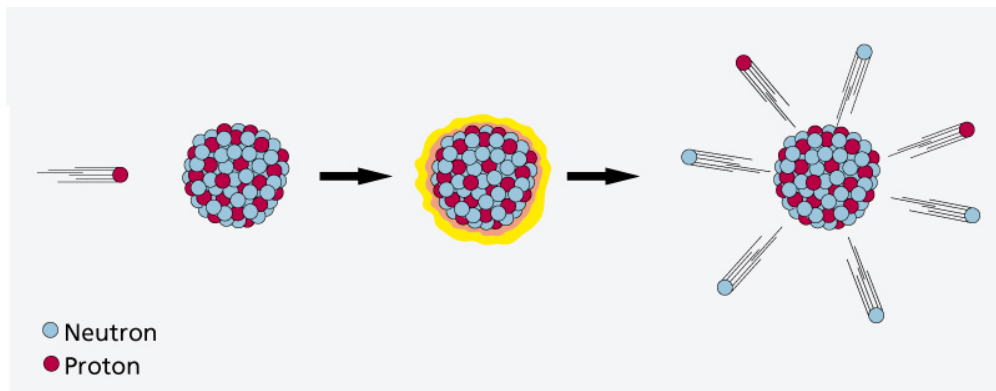

Figure 23: Illustration of the spallation concept, adapted from [71]. A proton hits a heavy nuclei whereafter the nuclei undergoes intranuclear cascade and then evaporation.

The produced neutrons, whether from reactor or spallation sources, have energies in the order of MeV which must be reduced to meV in order for the neutrons to be useful in scattering experiments. This is because the neutrons must have energies in the same order as the feature they aim to probe (phonons, magnetic structure, etc.). Moderators serve the purpose of reducing the neutron energy by slowing down the neutrons as they collide with the moderator medium. Many moderators contain hydrogen-rich substances, since hydrogen has a relatively high scattering cross section.

After passing through the moderator the neutrons are led toward each neutron instrument through a neutron guide. The inside of the guide tube is covered by a material which reflects neutrons well, such as nickel [69]. The neutrons pass through the guide by total external reflection, allowing the neutrons to travel long distances (10-100 m) without loosing intensity.

The neutron experiments for this thesis were performed at the ISIS Neutron and Muon Source, located at the Rutherford Appelton Laboratory in the UK. ISIS is a spallation

source and currently host over 30 neutron and muon instruments [72]. Experiments were performed on the neutron spectrometers MARI and LET.

Neutron experiments at large neutron scattering facilities is colloquially called 'beam-times', referring to the experimenter having been allowed a specific time interval to perform their experiments at the neutron beam. Beamtimes usually last 3-7 days, but can vary widely depending on the nature of the experiment and the instrument. The beamtime at MARI lasted 4 days whereas the beamtime at the newer and higher flux instrument LET lasted only ~ 12 hours.

5.7.1 Inelastic neutron scattering

The explanation of inelastic neutron scattering given below is based largely on [69].

The nature of inelastic neutron scattering is to measure magnetic excitations based on the difference between the initial energy, E_i, and final energy, E_f, of the scattered neutrons, $\hbar\omega = (E_i - E_f)$. Instead of the energies, it is usually instructive to describe the neutrons by their initial and final wave vector, $\boldsymbol{k}_i$ and $\boldsymbol{k}_f$, and the difference between them, called the scattering vector:

$$\boldsymbol{Q} = \boldsymbol{k}_i - \boldsymbol{k}_f \tag{32}$$

The scattering vector $\boldsymbol{Q}$ is a central quantity in all of scattering theory since it describes the momentum transfer. The size of $\boldsymbol{Q}$ can be found as $Q = \frac{4\pi\sin(\theta)}{\lambda}$, where λ is the wavelength and θ is half the scattering angle, since the scattering angle is referred to as 2θ. Combined with Bragg's law, Q and the lattice spacing d between lattice planes is related by $d = \frac{2\pi}{Q}$.
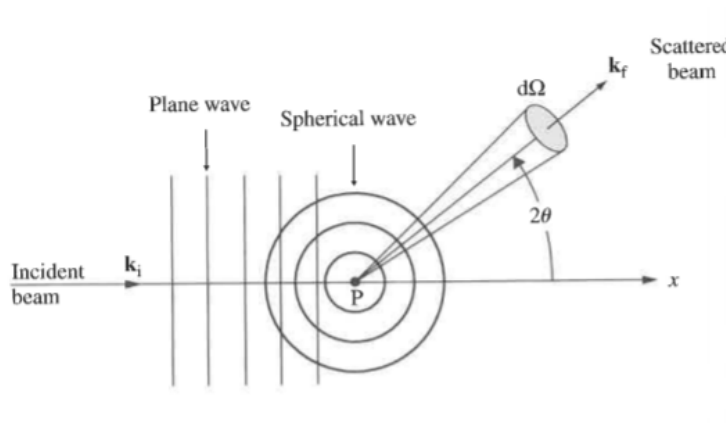

Figure 24: Illustration of neutron scattering, adapted from [69]. Plane waves scatter of a single nucleus located at P, generating spherical waves.

The concept of how neutrons scatter from a sample is illustrated in figure 24. Generally one could say that neutrons behave as particles when they are detected and created in nuclear processes, but behave as waves when they are scattered.

The incident neutrons travels as plane waves:

$$\psi_i = \mathrm{e}^{ik_i x} \tag{33}$$

When scattered from the nucleus located at the point P (in figure 24) the neutrons travel as spherical waves:

$$\psi_f = -b\frac{e^{ik_f r}}{r} \tag{34}$$

r is the radius from the scattering point P and b is the scattering length of the nucleus. The scattering length is a measure of how likely the neutron is to scatter with the nucleus, and vary widely by element and isotope with no apparent pattern, which is why they are measured experimentally. Scattering lengths are in the order of femtometers ($10^{-15}m$), and can obtain both positive and negative values.

The scattering length is useful in defining a quantity known as the cross-section, or total cross-section. There exist many kinds of cross-sections in neutron scattering theory so it is important to know what each of them represents. The total cross-section is a measure of the number of neutrons scattered in all directions per second, divided by the incident flux. The flux is simply the number neutrons per second per area, and can be found as $I = |\psi|^2 v$, where v is the velocity of the neutrons. The total cross-section can therefore be expressed as:

$$\sigma_{\text{total}} = \frac{I_f}{I_0} A_{\text{total}} = \frac{\left(\frac{b^2}{r^2}\right)v}{v} 4\pi r^2 = 4\pi b^2 \tag{35}$$

Here I_f is the scattered flux, I_0 is the incident flux and A_{total} is the area extended by the scattered neutrons which is a sphere. Defining the cross-section from the scattering length makes it clear that the cross-section is a measure of the systems ability to scatter neutrons [11].

On figure 24 a quantity indicated by $d\Omega$ is shown. This is the solid angle, defined as $d\Omega = \frac{dA}{r^2}$, where dA is the shaded area marked on the figure.

The solid angle is used in the definition of the double differential cross-section, which is the quantity measured in a neutron scattering experiment. The meaning of the double differential cross-section can be expressed as:

$$\frac{d^2\sigma}{d\Omega dE_f} = \frac{\text{number of neutrons scattered per second into a solid}}{\text{angle } d\Omega \text{ with final energy in the inertval } E_f \text{ to } E_f + dE_f}{I_0 d\Omega dE_f} \tag{36}$$

In physical formalism the double differential cross-section can be expressed as:

$$\frac{d^2\sigma}{d\Omega dE_f} = b^2 \frac{k_f}{k_i} N S(\boldsymbol{Q}, \omega) \tag{37}$$

N is the number of atoms in the system. $S(\boldsymbol{Q}, \omega)$ is known as the scattering function or dynamic structure factor, which express the probability that scattering changes k_i to k_f.

In textbooks, derivation of cross-sections and structure factors are often separated into coherent and incoherent parts. Here the concept of coherent and incoherent scattering will be explained briefly and without derivation.

Coherent scattering stems from interference effects between the scattered neutron waves, thus yielding information about the overall structure and dynamics. Incoherent scattering stems from individual atoms, no interference, and due to slight deviations in e.g.

scattering lengths, this type of scattering yields incohesive information about the sample. In experiments, coherent scattering is responsible for the structural and dynamic features in the data, where incoherent scattering generates a uniform background.

5.7.2 Time of flight spectroscopy

Inelastic neutron scattering experiments are most commonly performed with triple-axis or time-of-flight (TOF) neutron instruments, which use a continuous beam and pulsed neutrons respectively. Triple-axis spectrometers excel at measuring excitations at given direction of Q (useful when using single crystals), whereas TOF spectrometers gives an overview of excitations in most of (Q, ω) space (useful when using powders) [69]. Since the sample is a powder, both of the neutron instruments used in this thesis is of the TOF type.

The TOF spectrometer setup can be either direct-geometry, where the incident energy, E_i, is known in advance, or indirect-geometry where the final energy, E_f, is known in advance. The direct-geometry setup is used in both MARI and LET. The direct-geometry spectrometer setup is illustrated in figure 25. The desired E_i is chosen by the use of a chopper, illustrated as a Fermi chopper in the figure but it could be another kind of chopper or multiple choppers. Choppers are rotating devices placed on the neutrons pathway designed to block most of the incoming neutrons, except for those allowed to pass through the chopper through strategically placed slits or holes. The width of slits and speed of rotation determines which neutron velocities (i.e. energies) can pass through and continue towards the sample. With the incident energy selected the neutrons scatter off the sample, and the final energy can be measured [69]. The time it takes the incident neutrons to travel from the chopper to the sample is:

$$\tau_i = \frac{L_1}{v_i}, \tag{38}$$

where L_1 is the distance from the chopper to the sample and v_i is the velocity of the incident neutrons. The time it takes the neutrons to travel from the sample to the detector is the difference between the total flight time and incident flight time:

$$\tau_f = \tau_{total} - \tau_i, \tag{39}$$

where the total flight time (chopper to detector) is directly measured in the experiment. τ_f can be defined in the same manner as τ_i, $\tau_f = \frac{L_2}{v_f}$, with L_2 being the distance from sample to detector and v_f being the velocity of the scattered neutrons. v_f can be expressed in terms of momentum $m_n v_f = \hbar k_f \Leftrightarrow v_f = \frac{\hbar k_f}{m_n}$, making it possible to isolate for k_f if the expression for the final flight time:

$$k_f = \frac{m_n L_2}{\hbar \tau_f} \tag{40}$$

Knowing the value of the final wave vector, the final energy is simply $E_f = \frac{\hbar^2 k_f^2}{2m_n}$. The value of Q is found from the wave vectors by:

$$Q^2 = k_i^2 + k_f^2 - 2k_i k_f \cos(\phi) \tag{41}$$

where ϕ is the angle displayed in figure 25.

Figure 26 illustrate how a TOF spectrometer works with respect to time. At the initial pulse all neutrons have approximately the same location, but as time goes the wavelength bands gets spread out since the short wavelength neutrons are 'fast' and the long
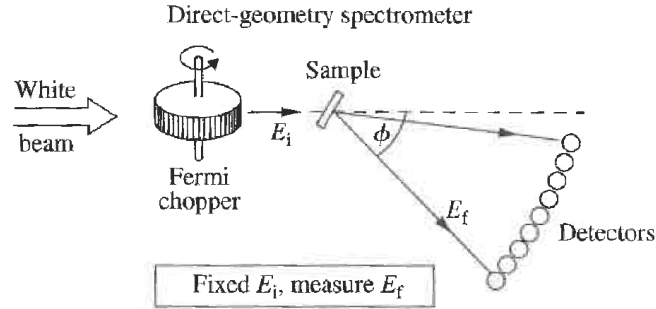
Figure 25: Illustration of a direct-geometry TOF spectrometer, from [69].

wavelength neutrons are 'slow'. The choppers aid to select the desired neutron energies and confining the beam by filtering out any deviating neutrons. When a segment of neutrons scatter with the sample some neutrons will be scattered elastically and some will be scattered inelastically. This is illustrated in the figure by three diverging lines originating from the same scattering time at the sample position. The middle line is a continuation of the initial flight path, referring to the elastically scattered neutrons which have the same energy (i.e. velocity) as before they were scattered. The two lines on either side of the elastic scattering line confines the wavelength band of the inelastically scattered neutrons, as inelastic scattering can happen by either gaining or losing energy which translates to getting faster and slower respectively.

Apart from the general concept of TOF spectrometers, figure 26 likewise illustrate the repetition rate multiplication (RRM) technique [73]. This technique is also referred to as multiple wavelength operation, which more clearly describes the function: separating the neutron pulse into multiple wavelength regions (five in this case, marked by $\lambda_1 - \lambda_5$), where conventional TOF instruments use only one wavelength per source pulse. This way of investigating multiple neutron energies at the same time vastly increases the efficiency of scattering experiments.
The important (and difficult) part of RRM is to properly separate the neutrons from one scattering incident from the previous, as this would cause scattered neutrons to be misidentified (spurions). The separation is done via a sequence of choppers, as the chopper rotation frequency is typically much higher than the source pulse frequency [73].
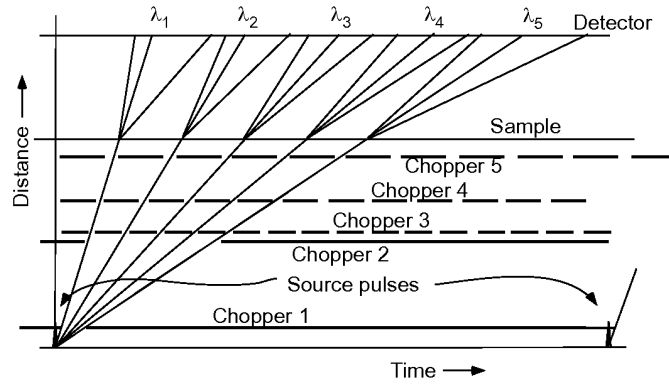
Figure 26: Illustration of the TOF principle and rate multiplication, from [73]. Horizontal lines indicate the placement of neutron instrument components whereas diagonal lines indicate how a neutron pulse travels trough the instrument.

5.7.3 MARI

The neutron experiments at the MARI spectrometer at ISIS was performed from 14/3/2019 to 17/3/2019. The spectrometer is illustrated in figure 27.

Figure 27: Illustration of the MARI spectrometer at ISIS, from [74].

The moderator used at MARI is a liquid-methane (CH_4) moderator working at around 105 K [75].

MARI uses multiple choppers to select the incoming neutron energies. First is a T_0 chopper which blocks off the beamline. The chopper is synchronized with the production of neutron pulses, and selects the initial range of wavelengths appropriate for the neutron instruments at hand, especially blocking the shortest wavelength (i.e. highest energy) neutrons [76].

After the T_0 chopper a set of two disc choppers is applied. Both the disc choppers and T_0 chopper are fairly simple in their construction, as they are discs made from a neutron absorbing material with a slit for the selected neutrons to pass through.

Lastly the neutrons are filtered through a Fermi chopper, made of curved layers of gadolinium. The curvature (in combination with the speed of rotation) determines

which neutron energies can pass through the chopper. Gadolinium is used because it is a good neutron absorber.

The detectors at MARI cover a wide array of angles ($3°$ to $134°$), making it ideal for studying powder samples which express all crystal plane orientations [74]. 20 % of the detectors had been upgraded the day prior to the experiment which was fortunate in terms of having new state-of-the-art equipment, but unfortunate in terms of normalization issues, but these were luckily resolved.

The powder sample was packed in a sheet of aluminum foil and placed along the inner perimeter of a cylindric aluminum can. The packing was performed in a helium atmosphere to exclude hydrogen from the sample environment, as hydrogen has a large scattering cross section and therefore might increase background.
The aluminum canister was placed at the end of a rod in order to be inserted in the cryostat. The canister was shielded from potential backscattered neutrons from the rod by a neutron absorbing boron nitride (BN) plate. The BN plate was chipped which caused concern of its shielding properties, but the compromised shape of the BN-plate was deemed to contribute insignificantly to the background, why it was used throughout the entirety of the experiment.
The cryostat could go to temperatures as low as 2.3 K and was operated up to $\sim$300 K.

5.7.4 LET

The neutron experiments at the LET spectrometer at ISIS was performed from 4/6/2019 to 5/6/2019. The experiment was carried out as an Xpress beamtime, where an ISIS instrument scientist performs the experiment within a short time frame, in this case 12 hours.

The moderator at LET is a liquid hydrogen (H_2) moderator working at around 18 K, which enables more cold neutrons (< 25 meV) at LET compared to MARI [77]. This is an advantage when the aim is to probe low energy excitations.
Neutrons enter the LET instrument by a straight guide whereupon they encounter a setup of five chopper segment. The first and last segments each consist of a set of counter rotating disc choppers. These choppers rotate fast and aim to monochromate the incident pulses, control E_i, and the resolution. The three slower choppers in the middle respectively limit time frame overlap from slow neutrons, limit pulse overlap, and stop decaying neutrons from the moderator. Overall the middle choppers prevents potential spurions and time frame contamination [78] [79]. The chopper setup at LET has been specifically designed for RRM, which, in combination with a higher flux, is why the experiment at LET was completed in only a fraction of the time of the experiment at MARI.

Using the RRM feature at LET four incoming energies were investigated simultaneously $E_i = 2.2$ meV, 3.7 meV, 7.6 meV and 22.3 meV.

The detectors cover $180°$ in the horizontal plane and $\pm30°$ vertically [79].

6 Results and discussion

6.1 Synthesis of Cr-jarosite

The synthesis followed that of Grohol and Nocera [34] (method 3), but with Cr instead of V. This synthesis procedure was used for all samples. Any deviations from the procedure is noted in the description of each sample in appendix A.

K_2SO_4 powder was dissolved in water. The dissolution was slower in D_2O compared to H_2O, so the deuterated solutions were heated while stirred. Concentrated H_2SO_4 (96%) was then added, and lastly Cr pieces was added to the solution.

The mixture was put in a 80 mL Teflon lined cylindrical hydrothermal vessel, as seen in figure 28, and heated in a Binder oven to 210 °C. The hydrothermal vessel remained in the heated oven for five days. After five days the hydrothermal vessel was removed from the oven, and cooled to room temperature during the course of approximately one day.

After cooling, the mixture was filtered using suction filtration, and rinsed with water (either D_2O or H_2O, depending on what was appropriate for the sample). Filtration yielded a dark powder which was then dried on a watch glass in an oven at approximately 65 °C for at least a couple of hours.

In total seven syntheses were performed, six of which were deuterated. The synthesis products are named SLL-1 to SLL-7 (where SLL-2 to SLL-7 are deuterated). Synthesis details for each synthesis is found in table 3. Remaining visible pieces of Cr metal was removed from all samples. On 5/3/2019 the six deuterated samples were combined into one collective sample of 6.9 g, leaving approximately 0.05 g of each of the original samples. The samples from each synthesis will be referred to as subsamples if they are not mentioned by their individual name, whereas the large sample will be referred to as simply the sample. Details about mass contributions from each subsample to the sample is found in appendix A.

The samples are not sensitive to air, but are still kept in sealed containers to prevent possible $D \rightarrow H$ exchange when stored for long intervals.

Figure 28: Picture of a disassembled stainless steel hydrothermal vessel and an assembled one, respectively. This vessel can contain 80 mL, and is custom made by the workshop of Department of Physics, Chemistry and Pharmacy at University of Southern Denmark.

Sample	Compound				Yield	
	K$_2$SO$_4$ [g]	Cr [g]	D$_2$O [mL]	H$_2$SO$_4$ [mL]	Amount [g]	% of max. yield
SLL-1 [a]	4.6497	0.6790	42	2	1.6389	85%
SLL-2	4.6596	0.6835	42	2	1.5052	77%
SLL-3	4.6578	0.6960	42	2	1.4238	72%
SLL-4	4.6710	0.6775	43	2	1.4403	75%
SLL-5	4.6657	0.6760	42	2	1.6017	83%
SLL-6	4.6670	0.6715	42	2	1.72	90%
SLL-7	4.6818	0.6740	42	2	1.6	84%

Table 3: Amount of reactants used in each synthesis, resulting yield of each synthesis, and yield percentage compared to maximal theoretical yield. [a] Synthesis performed with H$_2$O instead of D$_2$O.

6.2 NMR

The ^{2}H NMR spectra for the sample can be seen in figure 29. Spectra for the subsamples is in appendix B. Data analysis of ^{2}H NMR spectra was performed with the programs MestReNova and Python.

Cr-jarosites have only one type of deuterium environment and should therefore, in theory, show only one type of resonance in the ^{2}H NMR spectrum. In practice of course, things rarely work out as they should in theory. Any additional resonances are therefore a result of defects or impurities in the sample.
The spectra shows four distinctive resonances with each their set of spinning sidebands. The four resonances are marked in the figure at their respective chemical shifts. NMR results for all samples are found in table 4.

The most intense resonance in the spectrum corresponds to the stoichiometric Cr$_2$–OD environment. This environment will be referred to as Cr$_2$–OD (K$^+$), since the A-site is occupied by K$^+$. The chemical shift is at 818 ± 2 ppm, where Grube et al. [28] report $\delta = 855.4 \pm 8$ ppm and Janas et al. [80] report $\delta = 825 \pm 3$ ppm (average) for similarly produced Cr-jarosites. Since the discrepancies between the chemical shifts are not too large, the discrepancies are likely explained by temperature differences whilst spinning the samples [80], meaning that the reported chemical shifts are in agreement with the one measured here.
The resonance at $\delta = 872 \pm 5$ ppm is attributed to the Cr$_2$–OD environment as well, but where D$_3$O$^+$ substitutes K$^+$ on the A-site, in correspondance with Janas et al. [80] who find a similar resonance at $\delta = 868 \pm 7$ ppm (average). The intensity of this resonance (which will be denoted Cr$_2$–OD (D$_3$O$^+$)) constitute $\sim 2\%$ of the combined intensity in the spectrum.

Knowing that jarosites are prone to B-site vacancies, the resonance at 227 ± 2 ppm is attributed to resonances of Cr–OD$_2$ groups, which is the result of a Cr vacancy where excess deuterium has bonded to the available oxygen. This agrees with the Cr–OD$_2$ groups measured in [80] at 228 ± 2 ppm.
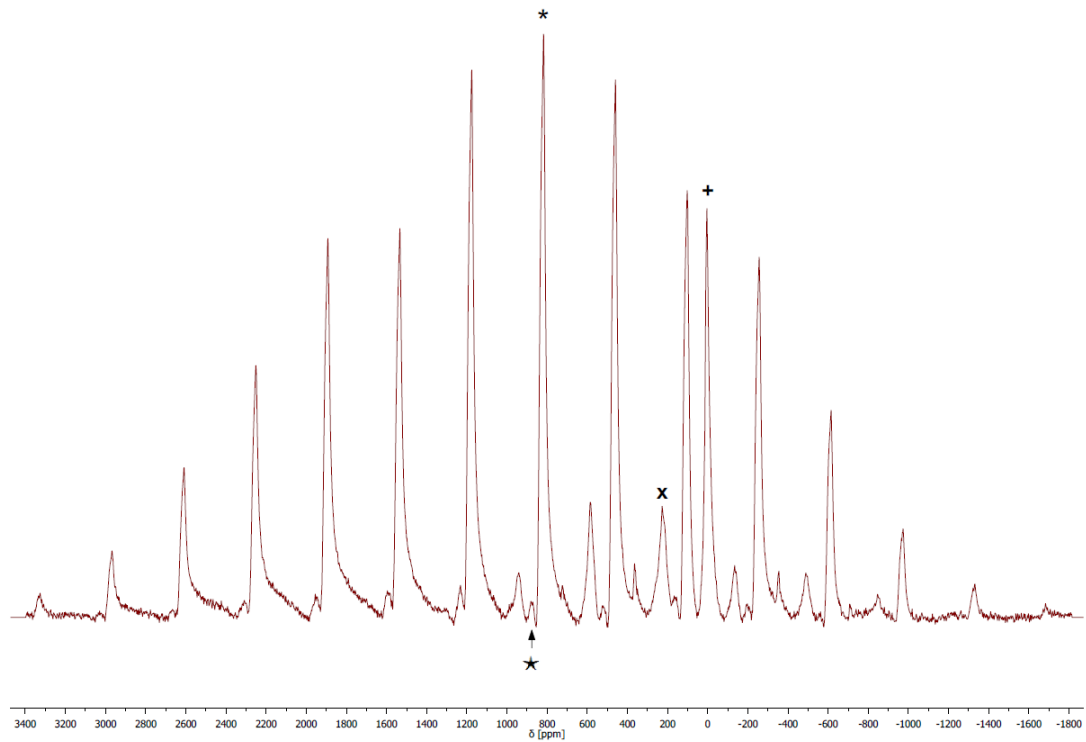
Figure 29: NMR spectrum of the sample recorded at 33 kHz. Symbols mark the chemical shift of the different deuterium environments. * indicate the chemical shift for the stoichiometric Cr_2-OD (K^+) environment at $\delta = 818 \pm 2$ ppm . The chemical shift for the defect environments are marked by $\mathbf{x}, +$ and $\star$, corresponding to $Cr-OD_2$ at 227 ± 2 ppm, D_2O/D_3O at 4 ± 2 ppm and Cr_2-OD (D_3O^+) at 872 ± 5 ppm respectively.

The resonance with chemical shift at 4 ± 2 ppm corresponds to some type of D_nO environment, likely a mixture of D_3O^+ and D_2O [80]. The presence of water could indicate that the sample has not dried sufficiently, but additional drying of a subsample (SLL-4 $\rightarrow$ SLL-4T) showed no significant reduction of this resonance, making this explanation unlikely. The D_nO environments are therefore most likely defects in the lattice, which fits with the general observations of defects in jarosites (section 3.3).

While the type of defect is determined from the chemical shift, the amount of defects is estimated by comparing the amount of signal from defect resonances to the signal from Cr-jarosite resonances. The amount of signal is simply the area of each resonance peak. This is found in Mestrenova by taking the integral of the signal in a manually set range. It is not only the signal at the chemical shift which is included, but also all spinning sidebands associated with a specific signal. In order to limit the effect of manual errors in the integration process, resonance integration was performed three times for each data set. The amount of defects found from integrated intensities is reported as the average of these three integration processes, and the reported error is the standard error of the mean. The amount of Cr vacancies are found by [29]:

$$4x = 6 \frac{\frac{1}{2}I(\mathrm{Cr-OD_2})}{I(\mathrm{Cr_2-OD}) + \frac{1}{2}I(\mathrm{Cr-OD_2})} \tag{42}$$

Here x is the concentration of vacancies, $I(\mathrm{Cr_2OD})$ and $I(\mathrm{CrOD_2})$ refer to the integrated intensities of the $\mathrm{Cr_2-OD}$ and $\mathrm{Cr-OD_2}$ resonances respectively. $I(\mathrm{Cr_2-OD})$ covers the combined intensities of the $\mathrm{Cr_2-OD}$ (K^+) and $\mathrm{Cr_2-OD}$ (D_3O^+) environment. The factor of $\frac{1}{2}$ in front of the $\mathrm{Cr-OD_2}$ intensity is due to the fact that this signal comes from two deuterium nuclei. The factor of 4 is due to the four OD groups which is affected by a Cr vacancy. The factor of 6 refers to the six OD groups in $\mathrm{KCr_3(SO_4)_2(OD)_6}$, and likewise the found x value should be divided by 3 to find the Cr vacancy percentage since there are three chromium atoms in the chemical formula. The found Cr vacancy of the sample is 2.4 ± 0.1 %. This is higher than the vacancies found in [32], which followed the same synthesis method, and also higher than the reported vacancies from most of the other similar studies, see table 1. The Cr vacancy for all samples are given in table 4. The Cr vacancy of the sample is smaller than what is estimated by the weighted average of Cr vacancies from the subsamples, which predicts a Cr vacancy of $\sim 4\%$. The reason for this discrepancy is unknown.

The vacancy formula (equation 42) assumes that all vacancies are isolated, ie. no vacancy is nearest neighbor to another vacancy. This is a reasonable assumption when few vacancies is present. Each Cr atom in the lattice has four Cr neighbors, so with the Cr vacancy of 2.4 %, the probability of a vacancy having at least one other vacancy as nearest neighbor is approximately 0.2 %, indicating that the assumption is reasonable for this system. This is calculated by $(1-a)^4 = 1-b$ where a is the vacancy probability of a Cr atom, $(1-a)$ is the occupancy probability of a Cr atom, $1-b$ is the probability that the four Cr neighbor positions are all occupied, and b is the probability that at least one of the four neighboring Cr positions is vacant. $a \cdot b$ is then the probability that a Cr atom and at least one of its four neighbors are vacant.

The average number of deuterons can be calculated in a similar manner to how the Cr vacancies are calculated [29]:

$$n = 6\frac{I(\mathrm{D}_n\mathrm{O})}{I(\mathrm{Cr}_2{-}\mathrm{OD}) + \frac{1}{2}I(\mathrm{Cr}{-}\mathrm{OD}_2)} \tag{43}$$

n is the average number of deuterons, $I(\mathrm{D}_n\mathrm{O})$ is the integrated intensity of the $\mathrm{D}_2\mathrm{O}/\mathrm{D}_3\mathrm{O}$ resonance at 4(2) ppm. The denominator is identical to that of equation 42. $n = 2$ or $n = 3$ correspond to full A-site occupancy by $\mathrm{D}_2\mathrm{O}$ or $\mathrm{D}_3\mathrm{O}$ respectively, whereas $n = 0$ corresponds to full K occupancy.

n for the sample is found to be 0.56 ± 0.03, indicating an A-site occupancy primarily by K, but with some substitution by $\mathrm{D}_2\mathrm{O}$ or $\mathrm{D}_3\mathrm{O}$. Values of n for all samples can be found in table 4.

The K vacancy can be calculated from the Cr vacancy and the amount of $\mathrm{D}_n\mathrm{O}$ present, as given by the defect formula in equation 2. The amount of K vacancies caused by Cr vacancies is simply the Cr vacancy multiplied by 3, since it is equivalent to x in equation 2 and 42. For the combined sample this equates to 7.2 ± 0.3 % K vacancy, caused by the Cr vacancy.

The amount of substitution of K with $\mathrm{D}_3\mathrm{O}$ can be estimated by n. Since n covers both $\mathrm{D}_3\mathrm{O}^+$ and $\mathrm{D}_2\mathrm{O}$, and the ratio between these are unknown, we can only estimate the maximal $\mathrm{D}_3\mathrm{O}$ substitution, by assuming that none of the contribution to the n-value stems from $\mathrm{D}_2\mathrm{O}$. If only $\mathrm{D}_3\mathrm{O}^+$ contributes to the n-value of the sample of $n = 0.56 \pm 0.03$, and all $\mathrm{D}_3\mathrm{O}^+$ ions are occupied on the A-site, it is equivalent to $18.7 \pm 1.0\%$ occupancy by $\mathrm{D}_3\mathrm{O}^+$. If only $\mathrm{D}_2\mathrm{O}$ contribute to the n-value, it corresponds to $28.0 \pm 1.5\%$ occupancy by $\mathrm{D}_2\mathrm{O}$ on the A-site. This is in the same range as the K vacancies found in Janas et al. [80].

Sample	$\delta(\mathrm{Cr}_2{-}\mathrm{OD}\,(\mathrm{K}^+))$	$\delta(\mathrm{Cr}_2{-}\mathrm{OD}\,(\mathrm{D}_3\mathrm{O}^+))$	$\delta(\mathrm{Cr}{-}\mathrm{OD}_2)$	$\delta(\mathrm{D}_n\mathrm{O})$	Cr vacancy [%]	n
SLL-2	810 ± 16	858 ± 22	227 ± 42	3 ± 40	4.4 ± 0.0	0.74 ± 0.02
SLL-3	816 ± 14	-	220 ± 38	-2 ± 32	4.7 ± 0.2	0.49 ± 0.05
SLL-4	809 ± 13	855 ± 24	230 ± 37	0 ± 32	2.4 ± 0.1	0.45 ± 0.01
SLL-5	814 ± 20	-	220 ± 36	-3 ± 35	3.9 ± 0.3	0.52 ± 0.01
SLL-6	809 ± 17	857 ± 21	225 ± 43	2 ± 33	3.6 ± 0.1	0.55 ± 0.01
SLL-7	809 ± 11	857 ± 17	226 ± 40	-1 ± 27	3.0 ± 0.2	0.60 ± 0.01
Combined sample	817 ± 30	875 ± 30	227 ± 40	4 ± 20	2.4 ± 0.1	0.56 ± 0.03

Table 4: Isotropic chemical shift, Cr-vacancy, and average number of deuterons (n) of sample and subsamples. The chemical shifts are given in units of ppm and the error is given as FWHM of the resonance. The reported error on the Cr-vacancy and n is found as the standard error of the mean.

6.3 TGA

In figure 30 the sample temperature is plotted versus the mass percentage, i.e. remaining sample mass in the furnace. Similar plots and tables for the subsamples are shown in appendix D. Most samples, except for SLL-4, have four mass losses. The mass loss has been estimated through manual assessment of the mass loss regions, whereafter the mass loss percentage has been calculated using Python. Details about the mass loss steps are found in table 5. It is beyond the scope of this project to determine what chemical decomposition causes each mass loss step, instead the focus is on the overall mass loss. This is also why there is no useful estimate of why the mass loss steps in SLL-4 differ from the rest.
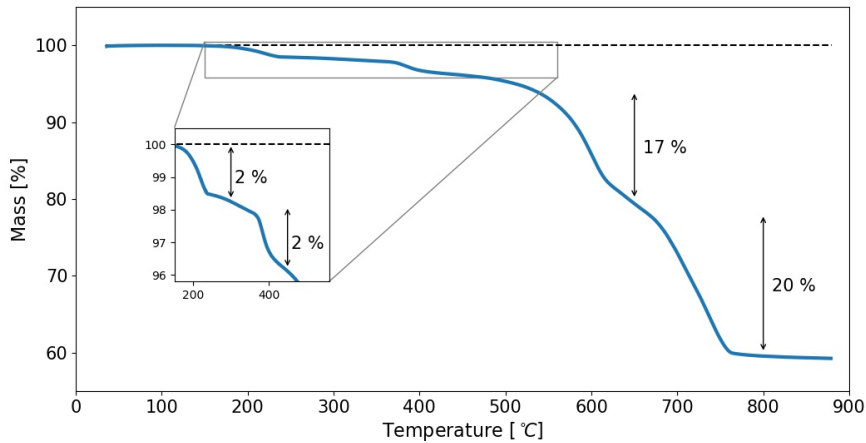
Figure 30: TGA curve for the collective sample. Arrows indicate the four mass loss steps together with the mass loss percentage for each region (rounded numbers) . The cutout region shows the TGA curve from 150 $°C$ to 560 $°C$. The dotted line indicates the original sample mass percentage.

Mass loss no.	Temperature [$°C$]	Remaining mass [mg]	Mass percentage [%]
1	300$°C$	45.31	98.2
2	450$°C$	44.33	96.1
3	650$°C$	36.61	79.4
4	800$°C$	27.47	59.6

Table 5: Quantification of the four mass losses in TGA of the sample.

Assuming that the sample is pure Cr-jarosite the thermal decomposition could be:

$$KCr_3(SO_4)_2(OD)_6 \, (s) \longrightarrow$$
$$0.5 \, K_2O \, (s) + 1.5 \, Cr_2O_3 \, (s) + 2 \, SO_2 \, (g) + 3 \, D_2O \, (g) + O_2 \, (g)$$
$$(44)$$
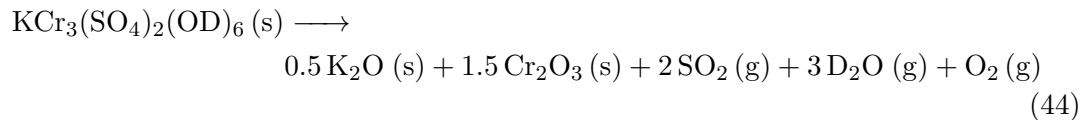
This suggests that K_2O and Cr_2O_3 will remain as solids after the reaction, whereas SO_2, D_2O and O_2 will have evaporated. As Cr-jarosite has a molar mass of 443.310 $\frac{g}{mol}$ and the remaining products ($0.5 \, K_2O + 1.5 \, Cr_2O_3$) have a combined molar mass of 275.084 $\frac{g}{mol}$, the TGA should show a remaining mass percentage of 62.1 %.
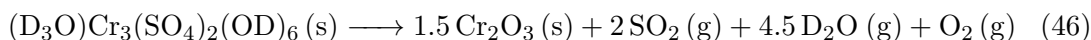
46

The sample shows a remaining mass percentage of 59.6 %, which suggests that the proposed decomposition might be wrong or that there might be impurities in the sample which could lower the remaining mass percentage. ^{2}H MAS NMR suggests that the sample contains Cr-vacancies, and some hydronium and/or water.

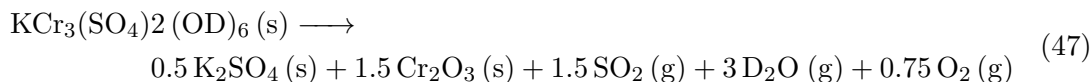The thermal decomposition of a Cr-jarosite molecule with one Cr vacancy could be:

$$\text{Cr}_2(\text{SO}_4)_2(\text{OD}_2)_4(\text{OD})_2\,(\text{s}) \longrightarrow$$
$$\text{Cr}_2\text{O}_3\,(\text{s}) + 2\,\text{SO}_2\,(\text{g}) + 5\,\text{D}_2\text{O}\,(\text{g}) + \text{O}_2\,(\text{g}) \tag{45}$$
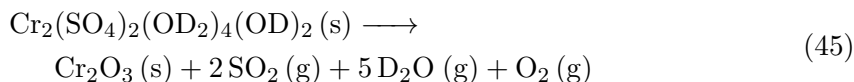
The defect Cr-jarosite has a molar mass of 402.19 $\frac{g}{mol}$ and the remaining Cr_2O_3 have a molar mass of 151.99 $\frac{g}{mol}$, resulting in a remaining mass percentage of 37.8 %. To get the experimentally found mass percentage of 59.6 % from pure Cr-jarosite and defect Cr-jarosite would require approximately 10% of the sample to be defect jarosite, which from the NMR results seems unlikely. In order to fit the NMR result of 2.4 % Cr vacancies, either the thermal decomposition of pure Cr-jarosite in equation 44 is incorrect, or the sample contains additional impurities which would lower the remaining mass percentage significantly.

From ^{2}H MAS NMR it is evident that the sample contains at least some hydronium jarosite, $(\text{D}_3\text{O})\text{Cr}_3(\text{SO}_4)_2(\text{OD})_6$, which could contribute to lowering the remaining mass percentage. Lengauer et al [39] similarly measured a lower remaining mass percentage than expected for their Cr-jarosite samples, which they attributed to water, and hydronium on the A-site. The molar mass of hydronium jarosite is 426.25 $\frac{g}{mol}$, so if the thermal decomposition is as follows, the remaining mass percentage is 53.5 %:

$$(\text{D}_3\text{O})\text{Cr}_3(\text{SO}_4)_2(\text{OD})_6\,(\text{s}) \longrightarrow 1.5\,\text{Cr}_2\text{O}_3\,(\text{s}) + 2\,\text{SO}_2\,(\text{g}) + 4.5\,\text{D}_2\text{O}\,(\text{g}) + \text{O}_2\,(\text{g}) \tag{46}$$

This result seems reasonable since it would contribute to a lower remaining mass percentage than for pure Cr-jarosite. But again, if the presence of hydronium jarosite should account for the observed remaining mass percentage of 59.6%, it would require the sample to consist of 29% hydronium jarosite, which is conflicting with the results from other characterization methods. Therefore a proper percentage of hydronium-jarosite in the sample cannot be estimated from TGA results.

Another thermal decomposition of pure Cr-jarosite could be the one suggested by [81] for Fe-jarosite, here rewritten to the chromium analogue:

$$\text{KCr}_3(\text{SO}_4)2\,(\text{OD})_6\,(\text{s}) \longrightarrow$$
$$0.5\,\text{K}_2\text{SO}_4\,(\text{s}) + 1.5\,\text{Cr}_2\text{O}_3\,(\text{s}) + 1.5\,\text{SO}_2\,(\text{g}) + 3\,\text{D}_2\text{O}\,(\text{g}) + 0.75\,\text{O}_2\,(\text{g}) \tag{47}$$

This would result in a remaining mass percentage of 71.1 %, which is not consistent with the experimental results since it suggests an unsustainable amount of impurities ($> 30\%$) for it to be plausible.

The Cr-vacancy for each sample is found from the ^{2}H NMR measurements, and is plotted in figure 31 as a function of the remaining mass percentage found from TGA. Plotting a parameter as function of another parameter is a way to visualize the correlation between them. If the plotted points follow a trend, this indicates that the parameters are correlated. Except SLL-5, the points seem to indicate a negative trend where lower Cr-vacancy corresponds to higher remaining mass percentage, which is in

agreement with the theoretical predictions.

Linear correlation between two variables, x and y, is measured by the Pearson correlation coefficient [66]:

$$\rho = \frac{\overline{xy} - \bar{x}\bar{y}}{\sigma_x \sigma_y} \tag{48}$$

$\bar{x}$ and $\bar{y}$ is the mean of each variable and $\overline{xy}$ is the mean of the product of the two variables. σ_x and σ_y is the standard deviation of each variable. The numerator is the same as the covariance. The correlation coefficient is a number between +1 and -1, where ± 1 indicates 100 % correlation and 0 indicates 0% correlation.

The correlation coefficient for the Cr-vacancy and remaining mass for all samples is -0.38, which indicate a weak negative correlation. If SLL-5 is not included then the correlation coefficient is -0.82, indicating a strong negative correlation. There is nothing inherently off with SLL-5 which would qualify it to be excluded, apart from it not following the trend indicated by the other samples. One should therefore be reluctant to exclude it, but in the following, both the cases where SLL-5 is included and where it is excluded are considered. By making a linear fit to all samples and to all samples except SLL-5 it is seen that the slope of the fit excluding SLL-5 is more similar to the slope of the theoretical prediction than the fit including SLL-5. The theoretical prediction is determined from the proposed decompositions in equation 44 and equation 45. The reason behind the significant offset between observation and the theoretical prediction can be explained by the existence of some impurity in the sample. Some of this impurity is most likely water and/or hydronium, which is supported by ^{2}H MAS NMR results.
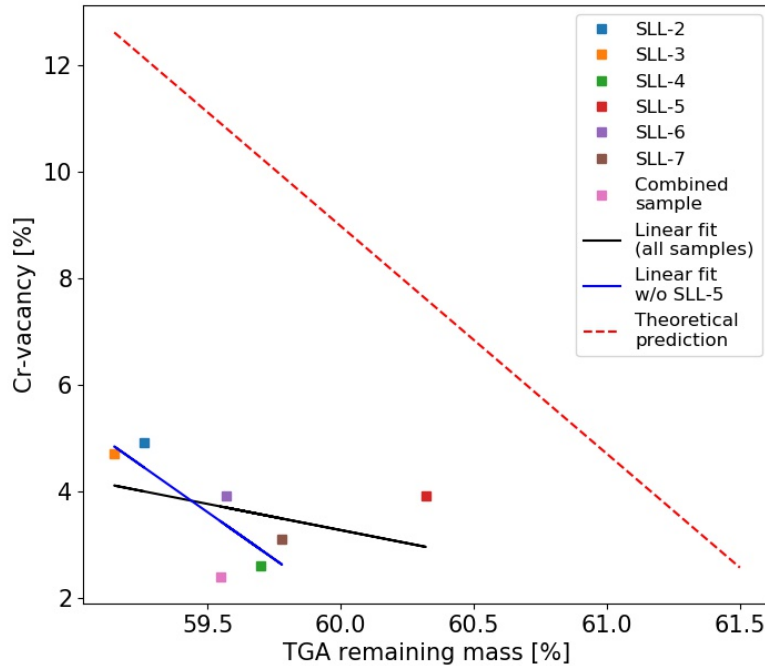
Figure 31: Cr-vacancy found from NMR measurements plotted as functions of the mass loss found from TGA.

6.4 IR

Figure 32 shows the IR spectra of a hydrogenated (SLL-1) and a deuterated (SLL-3) sample. The IR spectra of all subsamples is found in appendix C

Differences between hydrogenated and deuterated samples are seen in the spectrum as a shift in the position of absorption peaks from functional groups with hydrogen. Since the wavenumber depends on the effective mass of the group $\nu = \frac{\omega}{2\pi c} = \frac{1}{2\pi c}\sqrt{\frac{k}{m_{\text{eff}}}}$, the wavenumber decreases if the effective mass is increased. This is observed in the spectra in figure 32 as the absorption peak for the OH group is shifted from approximately 3500 cm^{-1} in SLL-1 to approximately 2500 cm^{-1} for SLL-3.

The ensemble of small peaks around 2100 cm^{-1} is possibly overtone bands of the peaks observed between $950-1250$ cm^{-1}, which can be attributed to $\nu_2(\text{SO}_4^{2-}) \approx 1190$ cm^{-1} and 1070 cm^{-1}, $\delta(\text{OH}) \approx 1010$ cm^{-1}. The fingerprint region looks similar for all deuterated samples, and is consistent with the results of [59] for a deuterated Cr-jarosite sample, seen in figure 9.

The deuterated samples show a slight remnant of $\nu(OH)$ around 3500 cm^{-1}, most notably in the spectrum of SLL-3 and SLL-7. This indicates that the subsamples are not completely deuterated which could be due to the presence of hydrogenated reactants. Generally the peak intensities cannot be used for quantitative estimates of concentration of functional groups since the intensities depends on the specific combination of bond and vibration type. But since the stretching modes of the OH- and OD-groups are quite similar, the relative intensities of the two peaks indicate that the samples are only slightly hydronated.
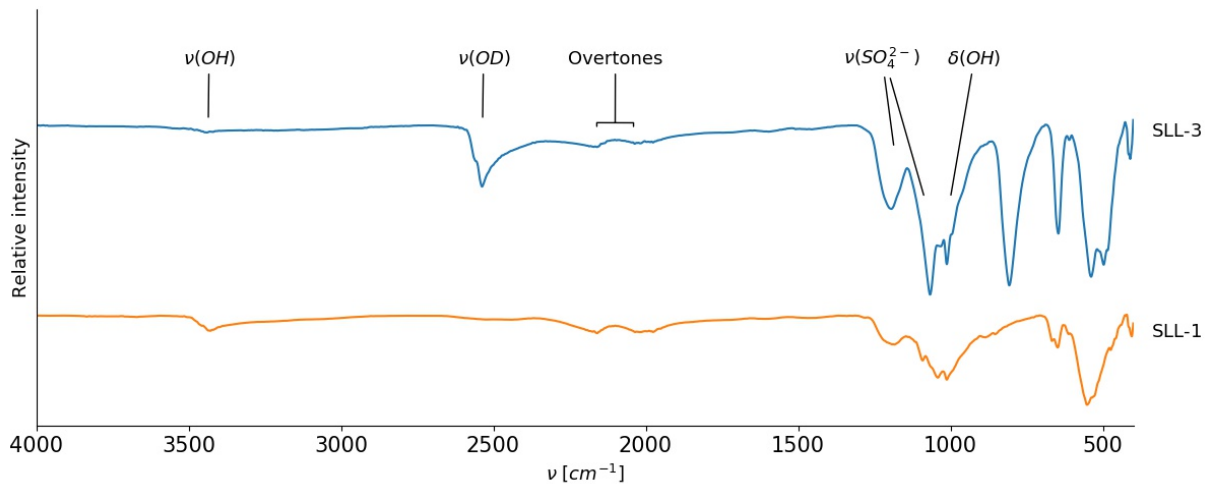
Figure 32: IR spectra of the hydronated sample SLL-1 and deuterated sample SLL-3. Assignment of the bands are shown in the figure. The spectra have been offset for comparison.

6.5   PXRD

Figure 33 shows the PXRD spectrum of the sample plotted with the peak position of a reference Cr-jarosite from [39]. The peak positions of the measured spectrum generally fit well with those of the reference spectrum, although the intensities are somewhat off. Generally the peak positions are of higher importance than the intensities.
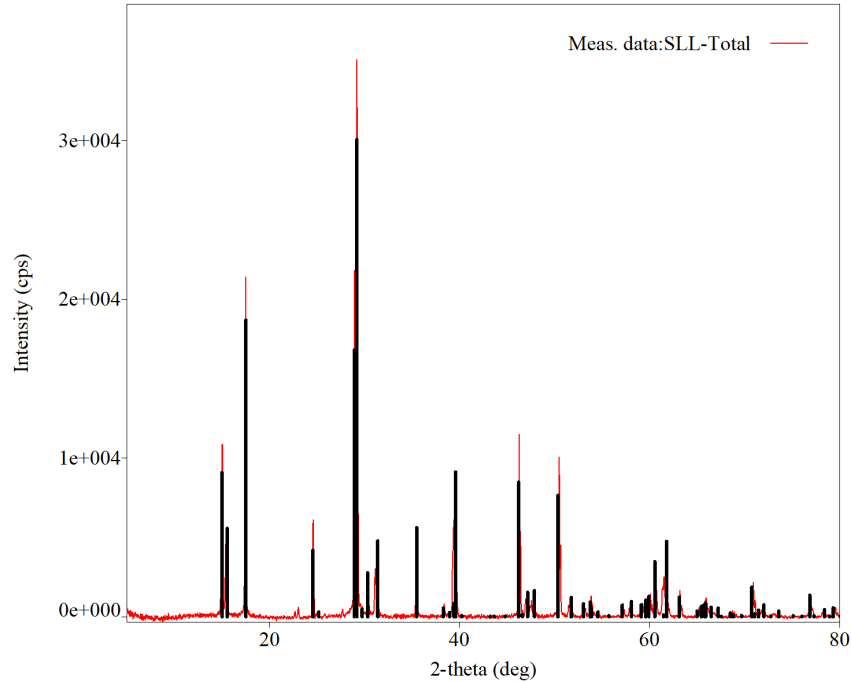

Figure 33: PXRD spectrum of the sample (red) with reference peak positions (black) from [39].

The two peaks at $2\theta \sim 23°$ and $2\theta \sim 26°$, seen more clearly on the subsample spectra in appendix E, are not accounted for by the reference spectrum. Comparing possible compounds from the PDXL 2 database, potassium sulfite K_2SO_3 seemed as the best candidate to explain the unaccounted peaks. If potassium metabisulfite $K_2S_2O_5$ is made from potassium sulfate K_2SO_4 due to lack of oxygen in the hydrothermal vessel during Cr-jarosite synthesis, it is plausible that potassium metabisulfite could decompose during the synthesis (it decomposes at 190 °C) to form potassium sulfite:

$$K_2S_2O_5\,(s) \longrightarrow K_2SO_3\,(s) + SO_2\,(g) \tag{49}$$

Discrepancies in intensity between the sample spectra and reference spectra might be caused by inadequate packing of the sample in the PXRD sample holder, or by inconsistencies with the reference sample since it was synthesized by conventional hydrothermal methods.

Rietveld refinement of the PXRD spectra for the combined sample was performed under instruction of PhD student Anders Bruhn Arndal Andersen, University of Southern Denmark, using the program FullProf Suite. The best Rietveld fit was found by varying five parameters: the unit cell lengths a and c, the occupancy on the K and Cr site, and

50
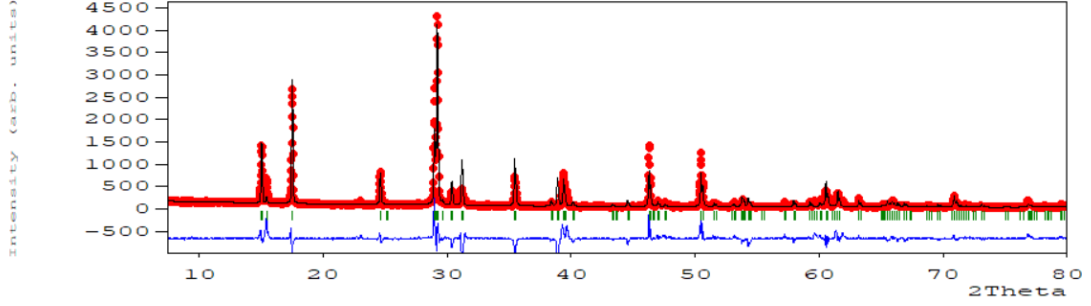
Figure 34: Rietveld refinement of PXRD spectra for the sample. The recorded data is shown as red dots, the Rietveld fit by the black line. Peak positions are indicated by the green lines and the blue line shows the residuals.

the overall scale factor of the fit.

The graphical result of the Rietveld refinement can be seen in figure 34. Overall the fit seems to be good, with some slight discrepancies in some of the intensities.

The refinement yielded reasonable estimates of the occupancy and cell parameters, given in table 6. The found values are close to the findings of [28] and [32], who use the same synthesis method and find $a = 7.229(1)$ Å, $c = 17.232(9)$ Å and $a = 7.2205(1)$ Å, $c = 17.2079(2)$ Å (average), respectively.

The value R_{Bragg} is a measure of how good the Rietveld fit is, and should ideally be close to 1. A value of 31.4 might therefore seem alarming, but based on how the fit looks visually, the high value might be explained by the discrepancies in intensity between observation and fit. Based on the visual fit and value of the refined parameters the refinement is reasonably good.

Table 6: Rietveld refined parameters for the sample

Crystal system	Trigonal
Space group	$R\bar{3}m$
Unit cell parameters [Å]	
$a = b$	7.22079(21)
c	17.17945(98)
Occupancy [%]	
K	93(1)
Cr	98(1)
R_{Bragg}	31.4

In Janas et al. [80] they characterize Cr-jarosites prepared by similar methods. Their Rietveld refinement showed discrepancies between the fit and Bragg peaks with large l values, since these peaks have an asymmetric shape.

Closer examination of the Rietveld fit show that the same phenomenon is true for the sample in this thesis, where discrepancy and asymmetry is observed for the Bragg peaks: (006) at $2\theta = 31.4°$, (20-4) at $2\theta = 35.5°$, (107) at $2\theta = 39.5°$ and (4-26) at $2\theta = 60.5°$. Janas et al. display the asymmetry and variance of the (107) peak across all samples, and comparison of the same peak from this study yields a similar result, seen in figure

35. The x-axis of 2θ is converted to q by Braggs law and $q = \frac{2\pi}{d}$. Although there might seem to be a little less variance in the peak shapes from this study, there is still no clear trend to the variations. Janas et al. state that the distorted shape of high l-value Bragg peaks is related to complex stacking disorder of the kagomé planes along the c-axis, which is likely caused by D_3O^+ on the A-site. Since it is known from the NMR results that D_3O^+ is present in some amount, this is a likely explanation here as well.

The disordered stacking also shows in the value of the c parameter, as the size of the A-site ion determines the distance between the kagomé planes. The c-value is lowered by the presence of D_3O^+ or H_3O^+, based on the results from Lengauer et al. [39]. They find $c = 17.08$ Å in a hydrogenated Cr-jarosite sample which likely hosts significant amounts of hydronium jarosite. Compared to what is likely the most stoichiometric value of $c = 17.232(9)$ Å from Grube et al. [28], the found value of $c = 17.17945(98)$ Å is likely a confirmation of some D_3O^+ content in the sample, which influences the stacking.
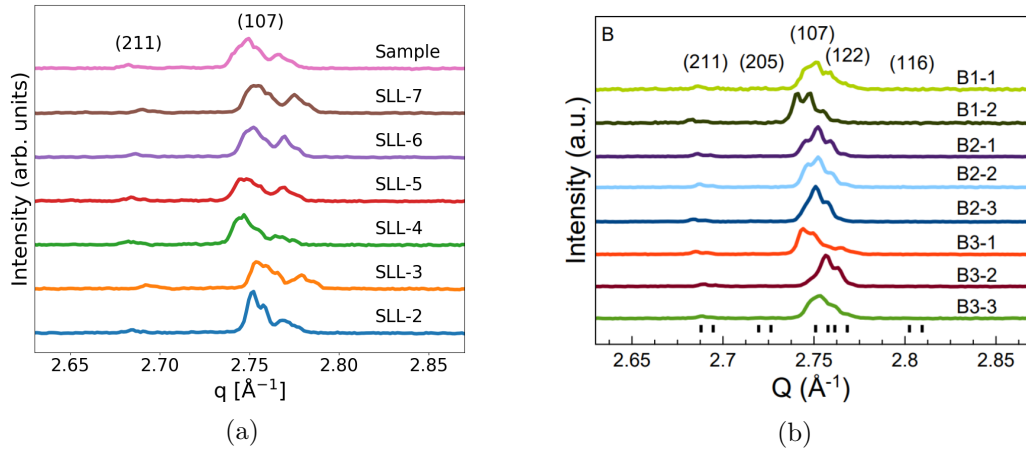
Figure 35: The (107) peak shape (a) from this study and (b) from Janas et al. [80].

6.6 SEM

Figure 36 shows two pictures from the SEM analysis. The full set of SEM pictures is provided in appendix F. The pictures show granules of the sample: Based on the provided length scale the granules are estimated to be 5-50 μm.
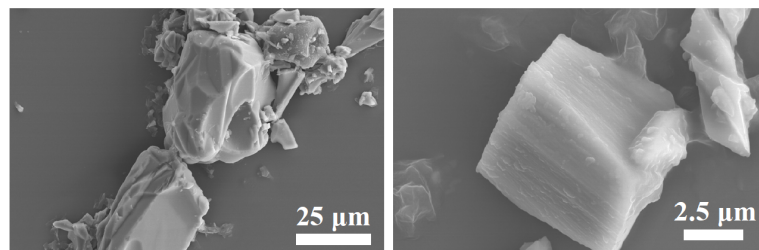
Figure 36: SEM pictures from two areas in the sample. The length scale for each picture is provided in the bottom right corner.

6.7   EDS

EDS measurements were taken at five randomly chosen areas in the sample. The data from the five measurements as well as the average of these is found in appendix G. Table 7 shows the atom percentage (at%) average and standard deviation ($\sigma_{at\%}$) from the EDS measurements. The values have been normalized to S = 2. The atom percentage is a measure of the number distribution of atoms for the constituting elements of the sample. In this case the atom percentage has been normalized to accommodate S = 2 in order to more easily compare the results to the elemental content designated by the chemical formula for Cr-jarosite. It is assumed that there are no defects on S (equation 2), therefore it can be used for normalization purposes.

For oxygen, the EDS measurement is not consistent with the expected value. This is most likely due to EDS being inherently unreliable in detection of lighter elements. Therefore the EDS value for oxygen will not be considered any further.

EDS measurements yield an average of K = 1.00 ± 0.21 and Cr = 3.29 ± 0.70 which is in agreement with the stoichiometrically expected values of 1 and 3, within the error. The value for the Cr content is higher than expected, the explanation probably being that some of the Cr has not reacted and lies as Cr pieces in the sample. This is reasonable since granules of Cr was found in the powder samples after synthesis. [82] also offers an explanation of possible traces of an amorphous phase containing Cr.

Element	Stoic. value	at%	$\sigma_{at\%}$
O	14	10.92	1.22
S	2	2.00	0.32
K	1	1.00	0.21
Cr	3	3.29	0.70

Table 7: Averaged and normalized (S = 2) atom percentage (at%) for the five EDS measurements, found in appendix G. $\sigma_{at\%}$ is the standard deviation of the measurements. Stoic. value refers to the stoichiometrically expected value.

Table 8 shows the K/S/Cr ratio for each of the five measurements, after normalizing by S = 2. Measurement 2 and 5 significantly pull up the average for Cr, possibly due to a Cr piece being in the area of measurement, but all measurements show at least some excess of Cr. The K content is fairly close to the stoichiometrically expected value, but the average is somewhat increased by measurement 5. The most realistic estimate for K occupancy from the measurements is probably measurement 1, which has the least amount of excess Cr: here the estimated occupancy is 94% for K.

Measurement	K/S/Cr
1	0.94/2/3.03
2	0.98/2/3.44
3	0.98/2/3.24
4	0.98/2/3.11
5	1.09/2/3.53

Table 8: Normalized (S = 2) atom percentage (at%) for the five EDS measurements, found in appendix G, displayed as the K/S/Cr ratio which stoichiometrically should be 1/2/3.

6.8 Discussion of defects and vacancies

There is overall agreement between characterization techniques that the majority of the sample consist of stoichiometric Cr-jarosite.

NMR, PXRD and EDS all give an estimate of the K and Cr occupancy, and it would only be reasonable to compare these results. The occupancy estimates are given in table 9. The EDS results have been converted to occupancy percentages.

Site	Estimated occupancy [%]		
	NMR	PXRD	EDS
K	72.0 ± 1.5 to 81.3 ± 1.0	93 ± 1	99.8 ± 20.7
Cr	97.6 ± 0.1	98 ± 1	109.8 ± 23.4

Table 9: Estimated Cr and K occupancy from different characterization techniques.

NMR and PXRD estimates are in agreement on the Cr occupancy, but EDS estimates significantly higher values. All EDS estimates of the Cr occupancy is probably not useful due to excess Cr in the sample, as mentioned.

There is a large discrepancy between the techniques for estimates of the K occupancy. As mentioned, the more reasonable EDS estimate for the K occupancy is likely that of measurement 1 of 94%, rather than the average.

Of the three techniques NMR is likely the most accurate, as well as the most precise, since PXRD analysis is sensitive to the fit with a reference spectrum and/or the quality of the Rietveld refinement, and EDS measurements is sensitive to local variances in the sample.

NMR shows the presence of OD_2 groups when Cr is vacant, as well as the presence of some D_2O/D_3O^+, where D_3O^+ is a likely substitute of K. TGA confirms that the presence of Cr vacancies and hydronium jarosite is a likely explanation of the lowered remaining mass percentage, although a fitting estimate of the defect level could not be found.

The presence of hydronium jarosite is further accentuated by the signs of disordered stacking indicated by the c-value from the PXRD analysis, since the disorder is likely caused by D_3O^+ on the A-site.

The discrepancy between the predicted Cr and n occupancy in the subsamples and

combined sample from the NMR results is peculiar at best. One might suspect that the time interval between NMR measurements of the subsamples and the combined sample (~ 6 months) might be at fault, but other jarosite samples which have been stored for many years have shown no sign of change. The only thing that has changed between the subsamples and the combined sample is that the combined sample has experienced two beamtimes, but it is doubtful that these events should have chanced the chemical composition of the sample.

6.9 Neutron scattering

Inelastic neutron scattering data are collected from two beamtimes, using the same sample. The first beamtime at MARI, ISIS (14/3/2019 to 17/3/2019), and the second as an express beamtime at LET, ISIS, (4/6/2019 to 5/6/2019).

Figure 37 shows intensity (q, E) maps from MARI at the lowest temperature measurement, 2.3 K, and at the highest temperature measurement, 100 K. The high intensity horizontal line along zero energy transfer corresponds to elastic scattering from the sample. Any signal not on the the elastic line stems from inelastic scattering. The interval of the color scale is chosen so that visualization of the magnetic excitations is optimized, which makes the elastic line look identical at all temperatures since the intensities of this region exceeds the chosen interval by a factor of ~ 50.

The white almost vertical streaks in the intensity map are the result of gaps between the detector plates, hence no neutrons are detected in these areas, corresponding to curves in (Q, E)-space.

Figure 37 shows some of the data from the MARI beamtime. Figure 37b shows the high temperature measurement (100 K), which shows no signs of magnetic excitations since this is well above the Néel temperature, $T_N \approx 4K$.

In figure 37a there is a magnetic excitation ($q \approx 1.2 \, \text{Å}^{-1}$, $E \approx 0.5$ meV) just above, and fusing into, the elastic line. The intensity seems to extend upward from the magnetic excitation, which could be indicative of a spin wave, but this signal is too diffuse to make a detailed quantitative analysis.

Since the data from MARI revealed the need of better resolution in order to properly examine the magnetic excitations, it was fortunately possible to get an additional beamtime at the newer ISIS instrument LET. Measurements on LET were carried out over the course of ~ 12 hours, compared to the three days on MARI, but yielded a much better resolution and intensity.

The LET measurements were performed with an array of different incoming energies: $E_i = 2.2$ meV, $3.7 \, \text{meV}$, $7.6 \, \text{meV}$ and $22.3 \, \text{meV}$. Figure 38 shows the 1.8 K data for the different incoming energies. Further inspection of the data in figure 38d shows slight indications of an acoustic phonon around $q \approx 3 - 5 \, \text{Å}^{-1}$ and $E \approx 5 - 15$ meV, but this observation will not be considered further in this thesis.

Visual inspection of the data deemed that data for $E_i = 7.6$ meV had the best balance of intensity and resolution for observing the magnetic excitation.

Intensity maps for $E_i = 7.6$ meV from LET for various temperatures are found in figure 39. Having data from a multitude of temperatures makes it possible to follow the progression of magnetic excitations.

Just like the data from MARI, there is no sign of excitations at 100 K. The 100 K and 70 K intensity maps are practically indistinguishable, whereas at 55 K there is a slight rise in intensity close to $q = 1.1 \, \text{Å}^{-1}$, which gets more pronounced as the temperature approaches 1.8 K. This observation is in general accordance with the Curie-Weiss temperature being ~ 60 K [80], [41].

The excitation is most clearly defined at 1.8 K, where the highest intensity area is seen as a circular shape, with a slight gap between it and the elastic continuum. The excitation and gap is more clearly visible in figures 38a and 38b. Some features extend from the high intensity point, one in the vertical direction forming almost a V-shape, and one in
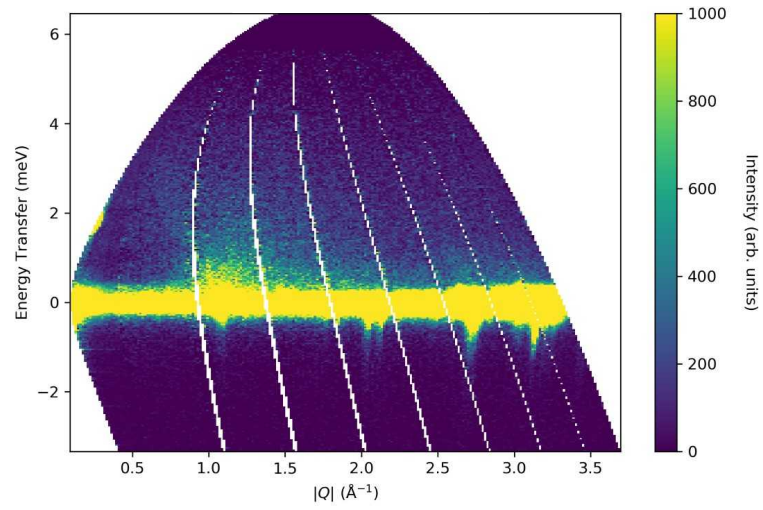
(a) 2.3 K
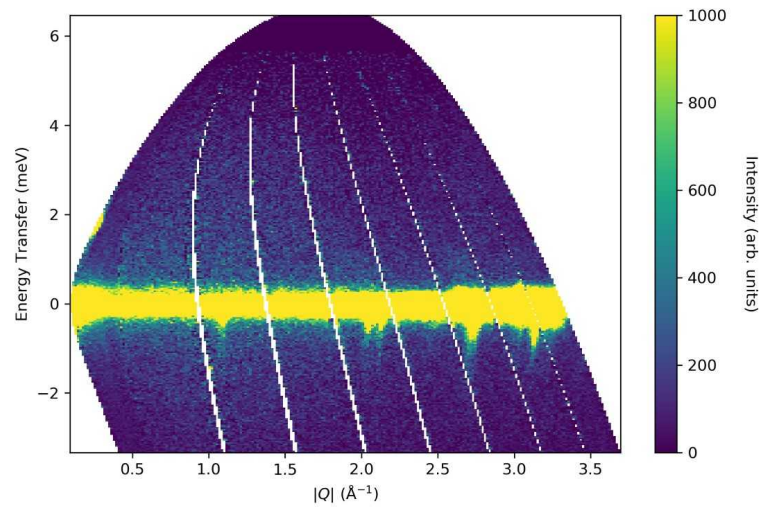
(b) 100 K

Figure 37: Intensity (q, E) maps of the Cr-jarosite sample from inelastic neutron scattering at MARI, $E_i = 6.67$ meV.

(a) $E_i = 2.2$ meV

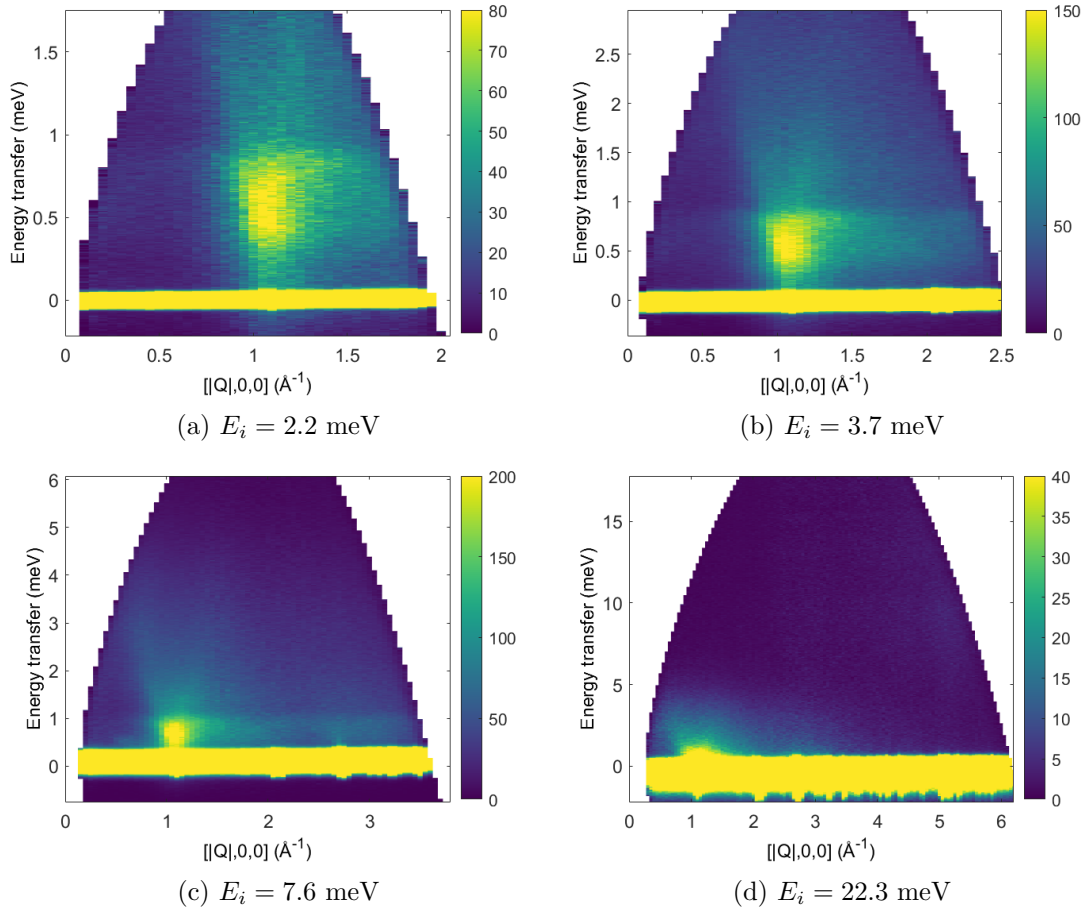(b) $E_i = 3.7$ meV

(c) $E_i = 7.6$ meV

(d) $E_i = 22.3$ meV

Figure 38: Intensity (q, E) maps for of the Cr-jarosite sample from inelastic neutron scattering at LET, four different incoming energies at 1.8 K. The color scale differs between all cases, and that the colorbar shows the intensity in arbitrary units. The color scale shows better digitally than on paper.

(a) 1.8 K   (b) 3 K   (c) 4 K

(d) 8 K   (e) 15 K   (f) 35 K

(g) 55 K   (h) 70 K   (i) 100 K
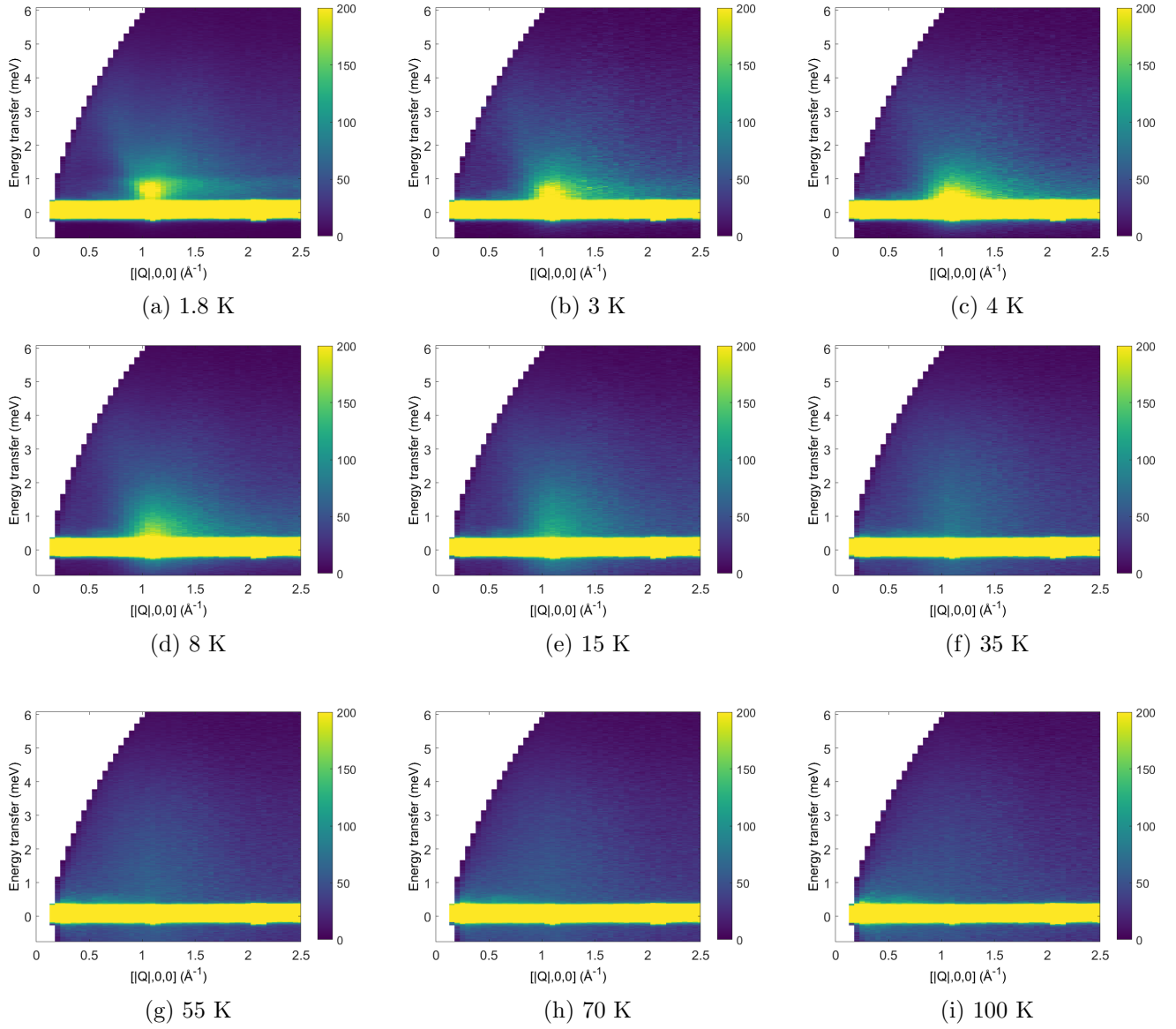
Figure 39: Intensity (q, E) maps for of the Cr-jarosite sample from inelastic neutron scattering at LET, $E_i = 7.6$ meV at nine different temperatures. The colorbar shows the intensity in arbitrary units. The color scale shows better digitally than on paper.

59

the horizontal direction. The vertical feature is most likely a spin wave, judging from the V-shaped features reminiscent of the spin wave dispersion relation. The sample is a powder which means that the data will show the average features of all crystal plane orientations. Since the spin wave dispersion relation looks almost like a V when viewed along one crystal orientation, the average from all orientations corresponds to a cone shape. This notion is in agreement with what is observed on the intensity map, which shows a slightly elevated intensity between the dispersion curves.

The horizontal feature extending from $q \approx 1\,\text{Å}^{-1}$ towards higher q values is probably a sign of a spin-wave affected by the DM interaction. In [16] the spin-wave spectrum of Fe-jarosite is explored, where the DM interaction is shown to contribute to a gapped spin-wave with a flatter curve than the rest. The existence of a DM interaction in Cr-jarosite is confirmed by Okubo et al. [41], Okuta et al. [36], and Janas et al. [80], which further accentuate the indication that the same phenomena is observed here.

Intensity maps are useful for getting an overview of the data at hand, but sometimes they can be a bit tricky to analyze since they can trick the eye by obscuring or enhancing features, depending on the color scheme. For this reason the chosen color scheme is linear, as to limit enhancement of certain intensities.

6.9.1 Structural data

In order to analyze the details of specific features in the intensity map it is conducive to make 'cuts' in the intensity map, meaning that only a specific section of data from the intensity map is displayed.

An example of such a cut is seen in figure 40. Here the cut is made at constant energy transfer, thereby displaying the intensity as a function of q at a certain energy.

Figure 40 shows a constant-E cut at $E = 0$, displaying the distribution of intensities in the elastic line. This is in order to visualize the Bragg peaks (both structural and magnetic). Since Bragg reflections are much more intense than magnetic excitations, the intensity scale goes to much higher values in this case.

The figure shows the intensity of Bragg peaks for the 1.8 K case and the 100 K case. The peaks with highest intensity have been labeled by their (hkl) plane on the basis of crystallographic information for deuterated Cr-jarosite [83], processed in the program VESTA [84]. Most of the peaks remain identical between the two cases, indicating that they are not affected by temperature and are therefore structural Bragg peaks. Since the magnetic behavior depends on temperature, the magnetic Bragg peaks occur below the magnetic phase transition. A magnetic Bragg peak is indicated in the figure by an arrow, this a magnetic Bragg peak from the $(hkl) = (012)$ plane, calculated to be at $q = 1.24\,\text{Å}^{-1}$. This magnetic Bragg peak does not coincide with any structural Bragg peaks since this possible structural peak is forbidden by the space group symmetry [80].
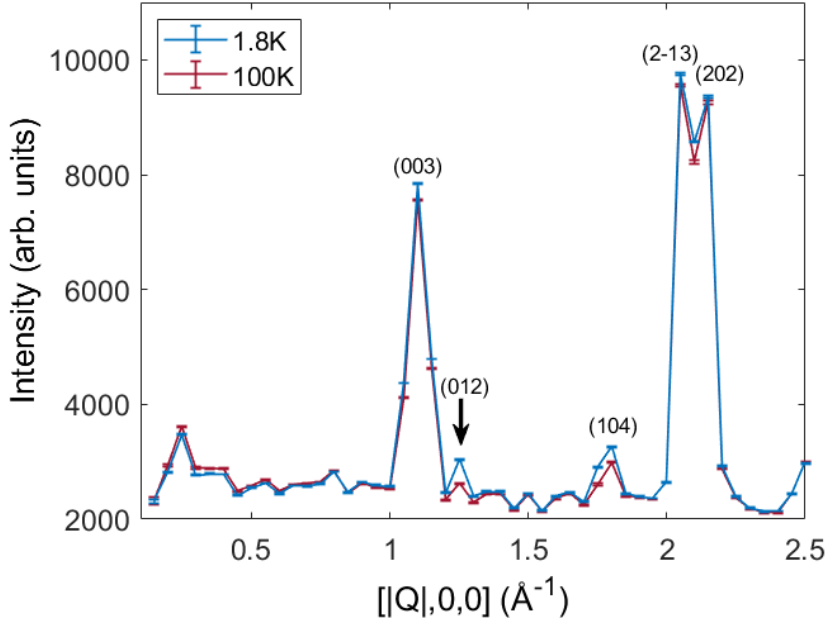
Figure 40: Constant-E cut at $E = 0$ for LET data, $E_i = 7.6$ meV. Both high temperature (100 K) an low temperature (1.8 K) data are displayed. Some peaks are labeled with the (hkl) plane from which they originate. The y-axis shows the intensity in arbitrary units.

6.9.2 Lower energy excitations

Figure 41 shows a constant-E cut at 1.8 K, through the magnetic excitation at $E = 0.7 \pm 0.1$ meV, in order to better determine the position in q. The peak in intensity is around $q = 1.07 \, \text{Å}^{-1}$. The peak is broad, $\Delta q \approx 0.3 \, \text{Å}^{-1}$, compared to e.g. the Bragg peaks, $\Delta q \approx 0.1 \, \text{Å}^{-1}$, in figure 40. A broad peak is an indication of short range correlations, since the Fourier transform of something narrow will be broad. The q value of the excitation should expectedly coincide with the position of the magnetic Bragg peak at (012), but here we observe that the peak intensity is at a lower q value.

In [85] the magnetic properties of hydronium jarosite $(D_3O)Fe_3(SO_4)_2(OD)_6$ is explored where a similar peak is found. The peak express the Warren line shape which is indicative of two-dimensional spin correlations [86], and it would be reasonable to assume the same phenomenon is at play in Cr-jarosite.

The Warren line shape is found from considering 2D, (hk), features in 3D, (hkl), reciprocal space. The original derivation by Warren [87] involves lengthy integration of reciprocal parameters, which is difficult to follow and understand. The following derivation is based on a more intuitive understanding of the parameters in reciprocal space.

Let us imagine q as the radius of a sphere in 3D reciprocal space, and the 2D Bragg peak as a rod along l, through ($hk0$). 2D features are represented by rods since they do not depend on the l-dimension, whereas 3D features are represented by points since they depend on all three dimensions. The sphere made from q represents all possible scattering points, of equal intensity, due to the sample being a powder. The shape of the 2D peak, a.k.a. the Warren line shape, corresponds to the overlap between the rod and the shell of the sphere. The center of the sphere has the coordinates $q = (0, 0, 0)$
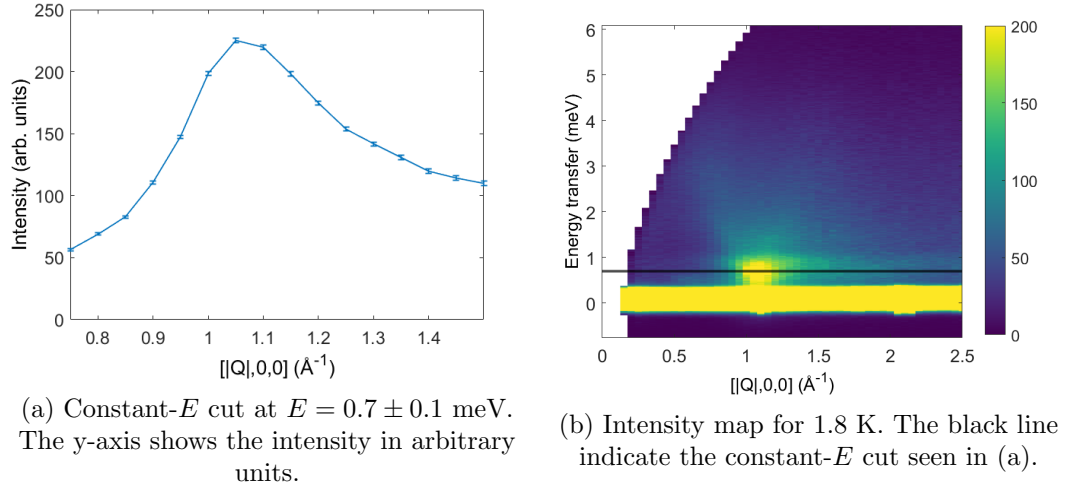
(a) Constant-E cut at $E = 0.7 \pm 0.1$ meV. The y-axis shows the intensity in arbitrary units.

(b) Intensity map for 1.8 K. The black line indicate the constant-E cut seen in (a).

Figure 41: Constant-E cut at $E = 0.7 \pm 0.1$ meV from the intensity map in figure 49a (1.8 K, $E_i = 7.6$ meV). The color scale shows better digitally than on paper.

and the rod has $q_m = (h, k)$. The width and depth of the rod are equal and are denoted dw. The width of the spherical shell is denoted dq and is related to the resolution of the scattering instrument.

(a) 2D projection of a spherical shell overlapping with a rod.

(b) Zoom in of the overlap region, for better visualization of parameters.
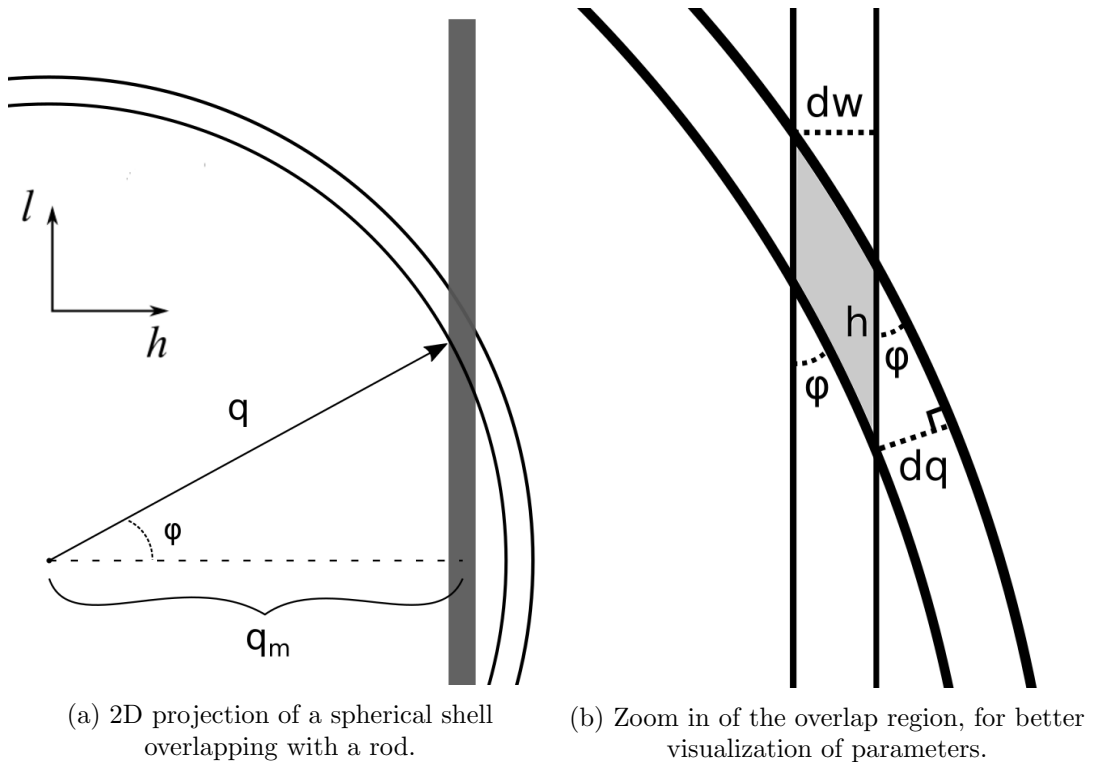
Figure 42: Illustration of how a powder scattering sphere in q space overlaps with a rod representing 2D features.

Figure 42 shows an illustration of the 2D layout of the rod and sphere. The shaded area on figure 42b marks the overlap between the shell and the rod, and must be multiplied by

the width of the rod, dw, to find the overlap volume (which in turn defines the observed intensity). The area has dimensions approximately equivalent to $A = h\,dw$, where h is marked on the figure. h is the hypotenuse in the right-angled triangle, suspended between the rod, the shell, and the width of the shell. This configuration assumes that this section of the shell can be approximated as a straight line. h is then found as $h = \frac{dq}{\sin(\phi)}$. $\sin(\phi)$ can be written in terms of q and q_m by observing that $\cos(\phi) = \frac{q_m}{q}$ and using the Pythagorean trigonometric identity to obtain:

$$\sin^2(\phi) + \cos^2(\phi) = 1 \Leftrightarrow \sin^2(\phi) = 1 - \cos^2(\phi) \Rightarrow \sin^2(\phi) = 1 - \frac{q_m^2}{q^2}$$

$$\Leftrightarrow \sin^2(\phi) = \frac{q^2}{q^2} - \frac{q_m^2}{q^2} \Leftrightarrow \sin^2(\phi) = \frac{q^2 - q_m^2}{q^2} \Leftrightarrow \sin(\phi) = \sqrt{\frac{q^2 - q_m^2}{q^2}} \tag{50}$$

The observed volume of the overlapping region is then:

$$V_{\text{overlap}} = A_{\text{overlap}}\,dw = h\,dw^2 = \frac{dq\,dw^2}{\sin(\phi)} = dq\,dw^2\sqrt{\frac{q^2}{q^2 - q_m^2}} \tag{51}$$

The Warren line shape is then found by normalizing the overlapping volume with the volume of the spherical shell. Assuming $dq \ll q$, the volume of the shell can be approximated as $V_{\text{shell}} = 4\pi q^2 dq$ [88]. The Warren line shape is then:

$$\text{Warren l.s.} = \frac{V_{\text{overlap}}}{V_{\text{shell}}} = \frac{dq\,dw^2}{4\pi dq}\frac{\sqrt{\frac{q^2}{q^2 - q_m^2}}}{q^2} = \frac{dw^2}{4\pi}\frac{1}{\sqrt{q^2 - q_m^2}\,q} \tag{52}$$

For the purpose of this thesis, dw^2 can be considered as a constant which will be accounted for by a scaling factor.

The approximations used to obtain this derivation causes the line shape to diverge at $q = q_m$, which is more sharp than what is reasonable to assume. One way to account for this is by convolution of the Warren line shape with a normal distribution, which will smear the line shape a bit. Convolution is a mathematical operation which yields the observed distribution from an initial distribution, $f(x)$, and a smearing function, $g(x)$. The convolution is performed by [89]:

$$(f * g)(x') = \int_{-\infty}^{\infty} f(x)g(x' - x)dx \tag{53}$$

In practice this was performed by summation of the product $f \cdot g$, where g is evaluated at each point x' along the interval. The function $f(x)$ is always the same, whereas $g(x' - x)$ changes as x' changes. The interval of interest in this case is $q = [0.7 \ldots 1.5]$, as seen on figure 41. In this case $f(x)$ corresponds to the Warren line shape, now denoted as $f(q)$, and $g(x' - x)$ is a normal distribution with a fixed standard deviation, σ, in the same interval of interest: $g(q) = \frac{1}{\sigma\sqrt{2\pi}}e^{-\frac{(q-\mu)^2}{2\sigma^2}}$. In this way $g(q)$ 'travels' along the interval, modifying the shape of $f(q)$. The result is convoluted function expressed as a vector where each element corresponds to the sum of $f(q) \cdot g(q')$.

A normal distribution is used as the folding function, $g(q)$, since this is the standard way of describing peak broadening. Peak broadening is a finite size effect from the grain size of the powder sample or the size of magnetic domains. The width of the normal distribution, σ can be approximately related to the size of the powder grains by [11]:

$\sigma \approx \frac{2\pi}{L}$, where L is the average diameter of a grain. For the functions plotted in figure 43 and 44 the value of σ is $\sigma \sim 0.1 - 0.2\,\text{Å}^{-1}$, which corresponds to $\sim 30 - 60\,\text{Å}$. This length scale corresponds to the size of the magnetic domains, since the lengths are inconsistent with the size of the powder grains, which from SEM is found to be $\sim 5-50\,\mu\text{m}$.

Figure 43 shows the same data as displayed in figure 46, superimposed with a convoluted Warren line shape. We have used the 2D version of the (012) Bragg reflection, which is simply (010), since the l component is ignored. The q value for this 2D reflection would be at $q = 1.008\,\text{Å}^{-1}$, but using the convoluted Warren line shape the predicted peak position of the excitation is shifted to $q = 1.073\,\text{Å}^{-1}$, which, as seen on figure 43, aligns almost perfectly with the observed peak position. In addition, the line shape of the excitation gives an almost perfect match. The position of the theoretical 3D Bragg peak is displayed for comparison.
The line shape deviates slightly from the data at the tails, this might be a result of the approximation of the convolution falling short, or, on the right-hand side, contributions in the measurements from features at higher q-values.
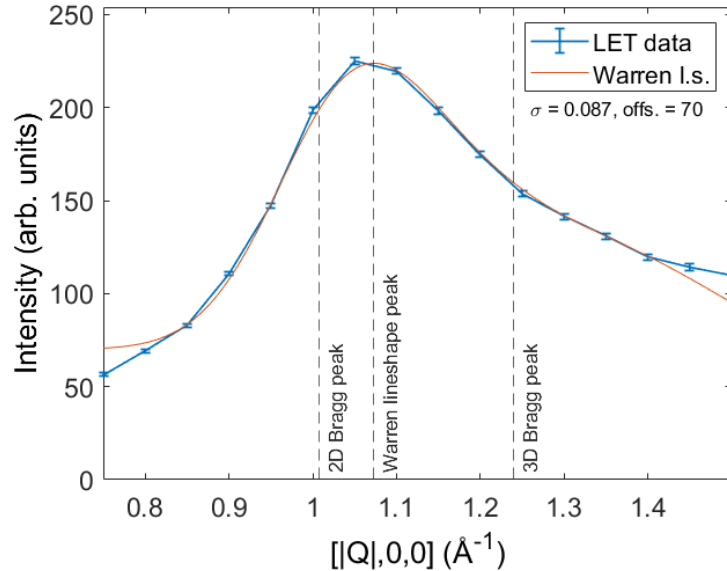
Figure 43: Constant-E cut at $E = 0.7 \pm 0.1$ meV for 1.8 K, overlayed with a convoluted Warren line shape. σ is the standard deviation of the convoluting normal distribution, in units of Å^{-1}, and 'offs.' is the offset in intensity, representing background. The dashed lines indicate the peak of the Warren line shape ($q = 1.073\,\text{Å}^{-1}$), the position of the 2D Bragg peak from which the line shape is constructed ($q = 1.008\,\text{Å}^{-1}$), and the position of the 3D Bragg peak from (012) at $q = 1.245\,\text{Å}^{-1}$.

Figure 44 shows constant-E cuts for four temperatures, 3 K, 4 K, 8 K, and 15 K, superimposed with a convoluted Warren line shape. These temperatures were picked because they, together with the 1.8 K data, display the excitation with significant intensity. The Warren line shape has been visually fitted to the data by adjusting the offset and standard deviation to the outline of the data. All four temperatures show overall agreement with the Warren line shape, again with some deviation in the tails.
Observing that the Warren line shape fits the excitation above the Néel temperature,

$T_N \sim 4\text{K}$, is further confirmation of the 2D nature of the excitation, since T_N is related to 3D ordering in the structure.
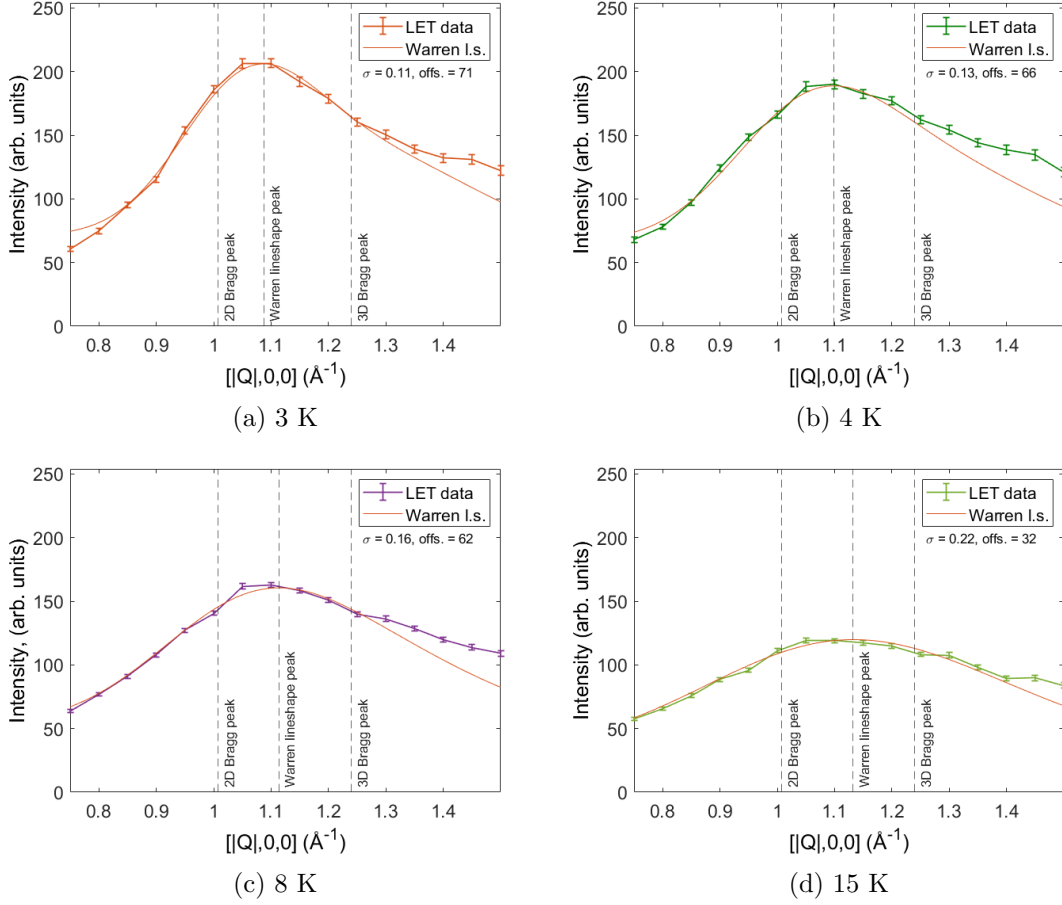

Figure 44: Similar to figure 43, constant-E cuts at $E = 0.7 \pm 0.1$ meV for four temperatures, overlayed with a Warren line. σ is the standard deviation of the convoluted normal distribution, in units of Å^{-1}, and 'offs.' is the offset in intensity, representing background.

Figure 45 shows how the magnetic domain size (L, found from σ), depends on the temperature. The magnetic domain size increases as the temperature decreases, and seems to diverge as T approaches zero. This behavior resembles critical scattering, and is similar to the results found by Janas et al. [90], who observe diverging correlation lengths. Theory of critical scattering predicts that critical phenomena follows a power law, and for the correlation length, ξ, the relation is $\xi \propto t^{-\nu}$ (for $T > T_C$), where t is the reduced temperature $t = \frac{T - T_C}{T_C}$, and ν is the associated critical exponent [91].

Fitting the data points in figure 45 to a power law yields an estimate of the critical exponent of $\nu = 0.37$. This is lower, but comparable to, what is found for the XY ($\nu = 0.669$) and Heisenberg ($\nu = 0.707$) models [91].

The fit estimates $T_C = 0.54$ K, which is reasonable considering the Mermin-Wagner theorem which states that 2D systems cannot have spontaneous breaking of continuous symmetries at finite temperatures [2], meaning that theoretically T_C should be zero for a 2D criticality phenomena.
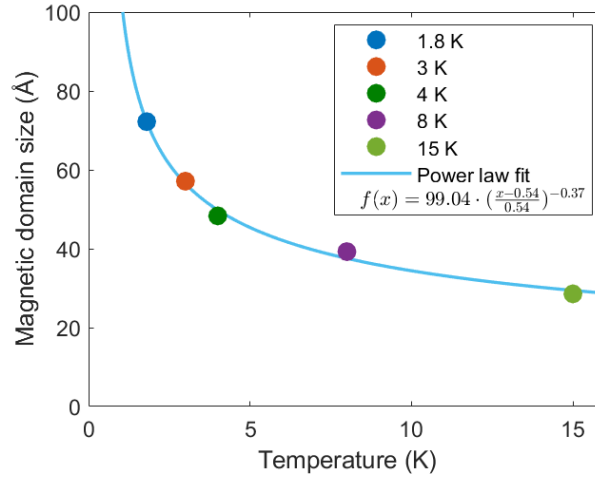
Figure 45: Magnetic domain size as function of temperature. The data is fitted with a power law.

Figure 46 compares a constant-E cut at $E = 0.7$ meV for all temperatures. The position, width, and evolution of the magnetic excitation throughout the temperatures is easy to follow, compared to the intensity maps in figure 39. Here we can quantitatively see how the intensity drops as the temperature increases, and the peak position remains the same throughout. At 55 K, effectively no signal from the peak remains.
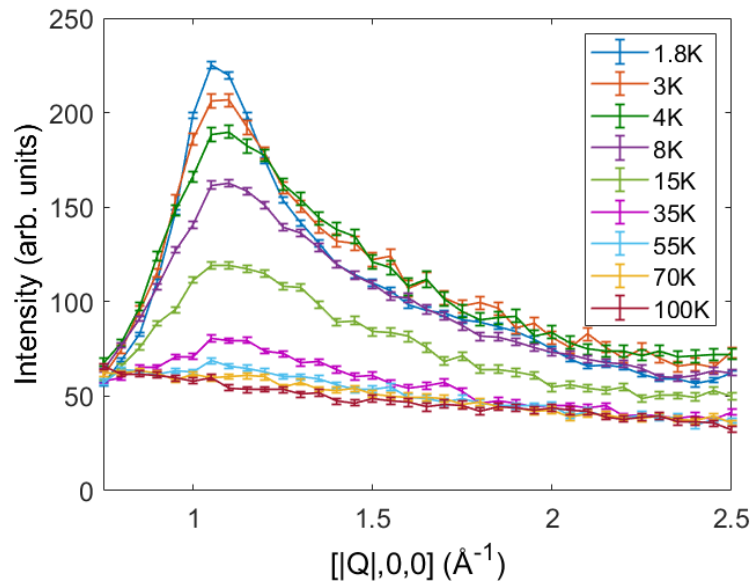
Figure 46: Constant-E cut at $E = 0.7 \pm 0.1$ meV from the intensity maps in figure 39.

Figure 47 compares a constant-q cut through $q = 1.10 \pm 0.05\,\text{Å}^{-1}$ for all temperatures. The cut is made through the highest intensity point in the magnetic excitation, and just like the constant-E cut in figure 46 it shows how the intensity rises as the temperature is lowered. The graph for 1.8 K shows a dip in intensity around 0.45 meV which is indica-

tive of a gap between the elastic continuum and the excitation. At higher temperatures the gap closes: one might argue that there is a slight remnant of a gap still present at 3 K, but at 4 K all signs of a gap is gone. Indications of the gap might be seen more clearly in the constant-q cuts for for $E_i = 2.2$ meV and $E_i = 3.7$ meV in figure 11 and 12 in appendix H.

The gap is clearly not related to the 2D dynamics as the gap disappears above T_N, but the 2D features persists. The origin of the gap could be from some sort of anisotropy, eg. the DM interaction in the ordered phase, but is not further quantified here.
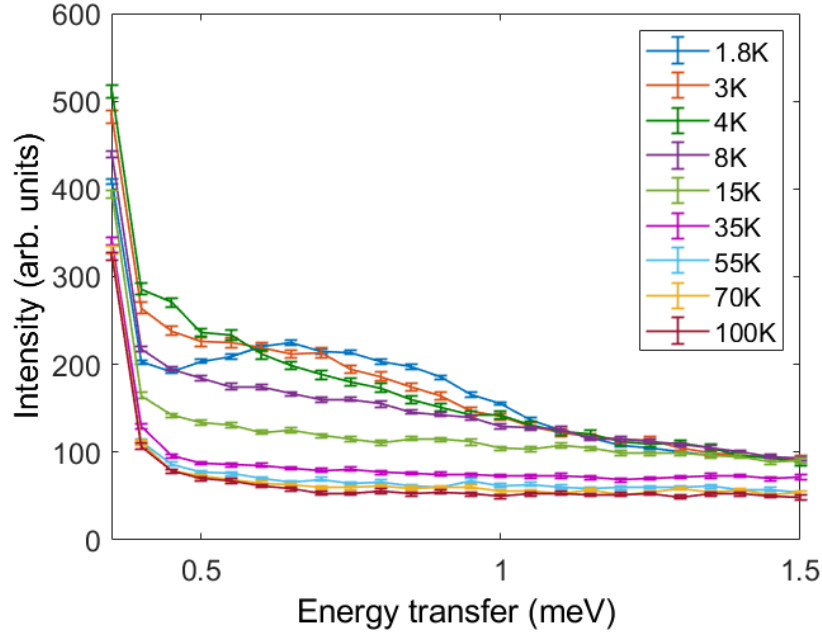
Figure 47: Constant-q cut at $q = 1.10 \pm 0.05 \, \text{Å}^{-1}$ from the intensity maps in figure 39.

6.9.3   Higher energy excitations

Figure 48 shows constant-q cuts, made in order to more closely examine the spin wave features. The aim is to look at the V-shaped and flat feature, marked by dashed lines in the figure, by making cuts at $q = 0.70 \pm 0.05 \, \text{Å}^{-1}$ and $q = 1.70 \pm 0.05 \, \text{Å}^{-1}$ respectively. Both cuts show only a slight indication of the features, but with too little signal to facilitate any quantitative analysis.

The dashed lines of the dispersion-like V-shape, which were visually fitted to the intensity map, can provide an estimate of the slope of the dispersion, which is equivalent to the spin wave velocity. The slope of the drawn dispersion is 7.2 meV·Å. This parameter might be useful in further analysis of the spin wave, but will not be considered further in this thesis.

(a) Constant-q cuts for 1.8 K. The y-axis shows the intensity in arbitrary units.

(b) Intensity map for 1.8 K. Black dashed lines indicate the spin wave features.
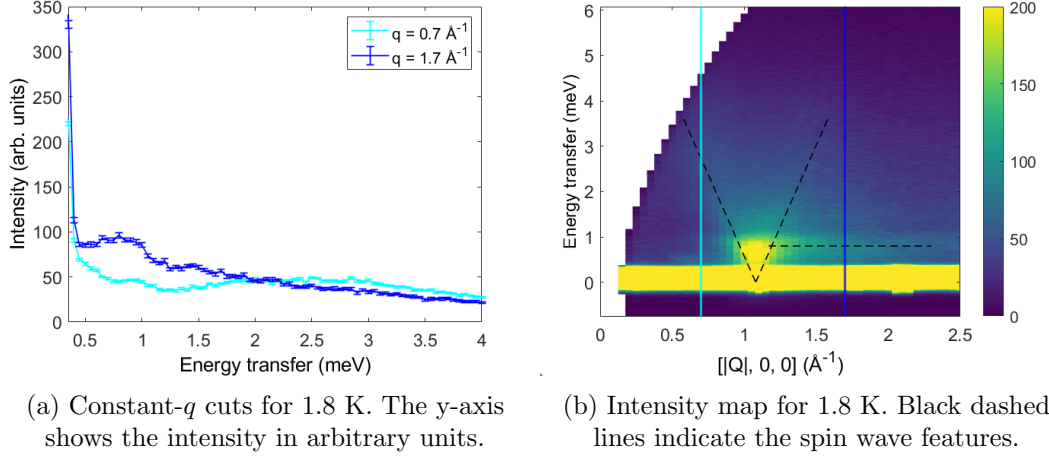
Figure 48: Constant-q cuts from the intensity maps in figure 39. The cyan and blue lines indicate the $q = 0.70 \pm 0.05\,\text{Å}^{-1}$ and $q = 1.70 \pm 0.05\,\text{Å}^{-1}$ cuts, respectively. The color scale shows better digitally than on paper.

6.9.4 Background subtraction

A way to reduce fuzziness of features in the intensity maps is by doing a background subtraction. Background measurements are performed at temperatures well above any critical temperature to ensure the absence of any magnetic features. In this case the 100 K measurement is considered to be purely background.

In order to do a proper background subtraction we need to be able to properly compare the two datasets. Therefore they need to be normalized in some way. Since the excitations seen in the scattering spectrum is caused by bosons (i.e. primarily phonons at high temperatures and magnons at low temperatures) we need to consult Bose-Einstein statistics. Here the Bose factor, n_B, is used to account for the distribution of particles at each energy at a given temperature, since the scattering intensity is proportional to $n_B + 1$ (the plus one represents the intensity when there is no Bosons in the system). Normalization is thus achieved by dividing the background (high scattering intensity) with $n_B + 1$, or alternatively, multiplying the low temperature data (low scattering intensity) with $n_B + 1$. The Bose factor is [2]:

$$n_B = \frac{1}{e^{\frac{E}{k_B T}} - 1},$$
(54)

where E is the energy, T is the temperature and k_B is Boltzmans constant.

Figure 49 shows what the intensity map for the lowest temperature looks like without and with background subtraction. The spin-wave features now look more defined on the intensity map, e.g. the gap between the magnetic excitation and the elastic continuum is a bit clearer.

Figure 50 compare the unsubtracted data to the data with subtracted background for constant-E and constant-q cuts. The y-axis is still proportional to the intensity, but after normalizing the data with the Bose factor it is more accurate to describe it as χ'', the imaginary part of the susceptibility. This can be found from linear response theory, more specifically the fluctuation-dissipation theorem, which shows that intensity $\propto S(q, \omega) \propto \chi''$ [92]. The background subtracted data in figure 50b make the gap

(a) 1.8 K

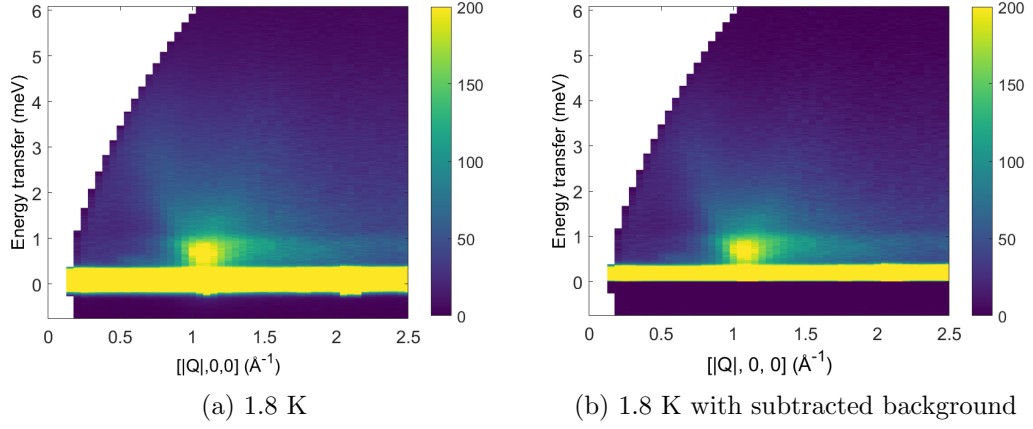(b) 1.8 K with subtracted background

Figure 49: Color plots for $E_i = 7.6$ meV at 1.8 K where (a) is identical to 39a and (b) has the background subtracted. The colorbar shows the intensity in arbitrary units. The color scale shows better digitally than on paper.

at ~ 0.45 meV slightly more noticeable, but otherwise the difference between the two datasets is generally insignificant compared to the size of the features we aim to analyze. This notion is true not only for the specific 1D cuts shown here, but also for all other cuts that were explored. Since it was found that background subtracted data show no significant improvements to the unsubtracted data, all previous figures display the unsubtracted data.

(a) Constant-E cut at $E = 0.7 \pm 0.1$ meV for 1.8 K, identical to the constant-E cut in figure 41a, respectively with and without subtracted background.

(b) Constant-q cut at $q = 1.10 \pm 0.05 \, \text{Å}^{-1}$ for 1.8 K, respectively with and without subtracted background.
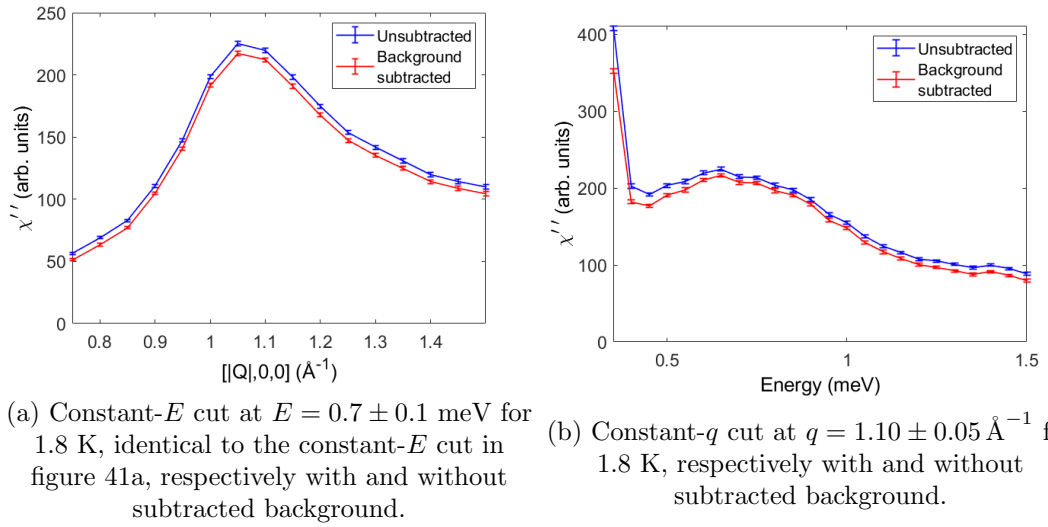
Figure 50: The effect of background subtraction for 1.8 K data, shown by constant-E and constant-q cuts.

6.10 Discussion of magnetic properties

Susceptibility measurements performed by PhD student Sofie Janas yielded $\Theta \simeq -58$ K and $T_N \simeq 3.7$ K for subsample SLL-4, which gives a frustration parameter of $f \simeq 15$, meaning that the sample falls well within the category of frustrated materials. This is just a confirmation of a fact that has already been established in many studies [80], [41], [40], [19]. The ordering temperature is comparable to that found in other studies [80], [41], [40], [93], [17].

Since both the susceptibility measurements and neutron scattering data shows 3D magnetic order, it is safe to say that this system cannot be classified as a spin liquid, as it was speculated it might have been.

If a sample is subject to a lot of defects it would generally be expected that this would diminish frustration effects and make it easier for the system to order. Since it was found that this sample has few Cr vacancies, it is not expected that this should have a significant effect on the magnetic properties in this case.

Since the system orders, it might be relevant to consider what type of spin configuration occurs. As seen from figure 40 the magnetic and structural Bragg peaks coincide, which indicates the $q = 0$ configuration. It is not possible to say whether it is the configuration with positive or negative chirality.

The ordering of the sample resembles that of classical ($S \ll \frac{1}{2}$) systems like Fe-jarosite ($S = \frac{5}{2}$) [3], [94], which also display ordering in the $q = 0$ configuration, rather than quantum systems ($S = \frac{1}{2}$), like Herbertsmithite or $(CH_3NH_3)_2NaTi_3F_{12}$, the latter of which have not shown long-range magnetic order down to 0.1 K [95].

Janas et al. [80] studied similar Cr-jarosite samples, produced with identical synthesis methods, which had comparable Curie-Weiss temperature, Néel temperature, and defects. They similarly conclude that the systems shows 3D magnetic order under $T_N = 3.8$ K, and compare it to Fe-jarosite.

In the study of Cr-jarosite by Lee et al. [19] they found weak long range antiferromagnetic order, and similarly compared their results to $S = \frac{5}{2}$ jarosite systems. The reason they found only weak long-range order might be due to vacancies, as they report only 76 ± 5 % occupancy by Cr on one of their samples. One would think that vacancies would rather make it easier for a frustrated system to order, but with such high vacancy it might cause the Cr atoms to be too scattered to achieve long-range order.

Lee et al. also hypothesized that the stacking of the kagomé planes influences the magnetic ordering, i.e. why the system ends up in the $q = 0$ configuration. Since it was found that the sample in this study has disordered stacking, it might influence the magnetic ordering here as well, even though one would think that stacking should not affect the 2D magnetic behavior, as the spins interact primarily in the kagomé planes (ab-plane) and the stacking is an effect along the c axis.

The neutron scattering data display both 3D phenomena, as by the magnetic ordering, as well as 2D phenomena, as seen from the excitation which fits the Warren line shape. The co-existence of 3D ordering and 2D dynamics of this variety has, to the authors knowledge, not been widely reported in the literature. A neutron study by Janas et al. [90] on the frustrated hexagonal lattice h-YMnO$_3$ similarly finds 2D dynamics within the 3D ordered state.

7 Conclusion

The synthesis yielded seven powder subsamples of Cr-jarosite, of which six are deuterated and mixed to a collective deuterated sample of 6.9 g. The charaterization analysis showed overall agreement between techniques that the sample consists of primarily stoichiometric Cr-jarosite.

The solid state ^{2}H MAS NMR experiments primarily revealed resonances from the stoichiometric Cr_2-OD environment, as well as low intensity resonances from $Cr-OD_2$ ($\delta = 818 \pm 2$ ppm), D_2O/D_3O ($\delta = 4 \pm 2$ ppm), and an unidentified environment at $\delta = 872 \pm 5$ ppm. The relative intensity of the $Cr-OD_2$ environment indicates that the sample contains 2.4 ± 0.1 % Cr vacancies. The relative intensities of the D_2O/D_3O environment suggest that K on the A-site is substituted with up to $18.7 \pm 1.0\%$ D_3O or up to $28.0 \pm 1.5\%$ D_2O.

IR measurements confirm the presence of OD groups, an indication of stoichiometric Cr-jarosite. IR further indicates slight remnants of OH groups, which might indicate that the sample is not fully deuterated. This has not proved to be a problem in any of the other measurements.

TGA measurements show four mass loss steps and a remaining mass percentage of 59.6%. The proposed thermal decomposition and other possible thermal decompositions found in the literature suggest a higher remaining mass percentage than what is found experimentally. The proposed thermal decomposition of defects suggests that defects in the sample, such as D_2O and D_3O^+ on the A-site, will lower the remaining mass percentage. Even considering the amount of defects suggested by NMR results, the proposed thermal decomposition is incompatible with TGA results. The thermal decomposition process of Cr-jarosite is therefore unknown and the proposed thermal decomposition for the defects cannot be confirmed either.

PXRD results show that the spectrum generally is consistent with reference spectra, with few discrepancies in intensity and peak positions, which can be explained by systematic differences from the reference measurement and impurities, respectively. Rietveld refinement yielded estimates of cell parameters $a = 7.22079(21)$ Å and $c = 17.17945(98)$, which is reasonably close to what is found in similar studies. The refinement also gave estimates of the Cr and K occupancy of 98% and 93% respectively. The value of the c parameter as well as the asymmetric shape of Bragg peaks with high l-values indicate that the sample is subject to disordered stacking of the kagomé planes, likely due to D_3O^+ on the A-site. Since the magnetic interactions primarily exist within each plane, the stacking should not affect the 2D magnetic properties.

Pictures of the powder granules from SEM showed grains in the range of 5-50 μm.
The EDS results support the high stoichiometry findings of the previous characterization techniques with a K/Cr/S ratio of 1.00/3.29/2.00 suggesting, what is already known, that excess Cr is present in the sample in the form of Cr pieces which have not reacted.

NMR, PXRD, EDS and susceptibility results are all in overwhelming agreement with the ones reported in Janas et. al. [80], since the samples were produced similarly.

The neutron scattering experiment at MARI yielded data with a resolution too low to perform convincing analysis of magnetic excitations. Based on the knowledge of the appropriate energy range from MARI, another experiment was performed at LET, which more clearly showed a magnetic excitation around $q = 1.07\,\text{Å}^{-1}$, as well as features from a spin wave with indications of a DM interaction. The data shows that the system is antiferromagnetically ordered in the $q = 0$ configuration below the Néel temperature, $T_N \simeq 3.7$ K, which debunks speculations of this system being a spin liquid.

The neutron scattering experiments show both 2D and 3D features, specifically 3D ordering and 2D dynamics. The excitation is clearly uncorrelated with the 3D ordering as it persists at temperatures way above the ordering temperature, up to ~ 55 K, and the near perfect fit with the Warren line shape confirms its 2D nature.

This exciting mixture of 2D and 3D physics is, to the authors knowledge, so far unexplored, and not explained by ordinary spin wave theory.

8 Outlook

Aspirations to make detailed investigations of the magnetic excitations in Cr-jarosite will require robust methods of making powder samples of higher purity or single crystals, preferably both. Acquisition and use of single crystals for neutron scattering experiments would presumably yield data which could be especially useful in, for example, modeling of spin waves and estimating the exchange parameters.

Production of higher purity samples might be feasible by having better control of the oxygen uptake during synthesis, such as suggested by Grohol et al. [15] where a lid supposedly floats atop the solution inside the hydrothermal vessel. This method was briefly attempted during the work of this thesis, but finding a lid with the appropriate thermal and buoyant abilities was not achieved at that point.

Another promising synthesis method to try out would be the high temperature/pressure method performed by Okuta et al. [36], which produced single crystals of Cr-jarosite. The initial challenge with this technique is in finding the proper equipment, since highly specialized hydrothermal vessels that can withstand ~ 150 MPa pressure are needed.

An additional method of characterizing the sample could be elemental analysis, where the elemental composition and elemental quantity can be determined. This would quantify excess elements compared to the stoichiometric composition, but not necessarily how they are incorporated in the structure.

Other relevant techniques which could be used to explore the properties of Cr-jarosite include heat capacity and susceptibility experiments. Susceptibility measurements were performed on subsample SLL-4 by PhD student Sofie Janas, but was not considered in detail in this thesis.

References

[1] Philip Ball. Quantum materials: Where many paths meet. *MRS Bulletin*, 42(10):698–705, 2017.

[2] Stephen Blundell. *Magnetism in Condensed Matter*. Oxford University Press, 2014.

[3] Philippe Lacroix, Mila Claudine, and Frédéric Mendels. *Introduction to Frustrated Magnetism: Materials, Experiments, Theory*. Springer, Berlin, Heidelberg, 2011.

[4] Kei Yosida. *Theory of Magnetism*. Springer, 1991.

[5] A. J. Berlinsky and A. B. Harris. Landau Theory for Two or More Order Parameters. In A. J. Berlinsky and A. B. Harris, editors, *Statistical Mechanics: An Introductory Graduate Course*, Graduate Texts in Physics, pages 223–261. Springer International Publishing, Cham, 2019.

[6] Karl W. Böer and Udo W. Pohl. Magnetic Semiconductors. In *Semiconductor Physics*, pages 1–24. Springer International Publishing, Cham, 2014.

[7] Chemistry libretext website. https://chem.libretexts.org/Bookshelves/Inorganic_Chemistry/Book%3A_Introduction_to_Inorganic_Chemistry/06%3A_Metals_and_Alloys-_Structure_Bonding_Electronic_and_Magnetic_Properties/6.08%3A_Ferro-%2C_Ferri-_and_Antiferromagnetism. Accessed: 03-09-2020.

[8] Charles Kittel. *Introduction to Solid State Physics*. Wiley, 2005.

[9] Tôru Moriya. Anisotropic superexchange interaction and weak ferromagnetism. *Phys. Rev.*, 120:91–98, Oct 1960.

[10] L. A. Mól, R. L. Silva, R. C. Silva, A. R. Pereira, W. A. Moura-Melo, and B. V. Costa. Magnetic monopole and string excitations in two-dimensional spin ice. *Journal of Applied Physics*, 106(6):063913, September 2009.

[11] Kim Lefmann. Neutron scattering: Theory, instrumentation, and simulation, Spring 2018.

[12] Takashi Imai and Young S. Lee. Do quantum spin liquids exist? *Physics Today*, 69(8):30–36, August 2016.

[13] Leon Balents. Spin liquids in frustrated magnets. *Nature*, 464(7286):199–208, March 2010.

[14] R. Moessner. Magnets with strong geometric frustration. *Can. J. Phys.*, 79(11-12):1283–1294, December 2001.

[15] Daniel Grohol, Kittiwit Matan, Jin-Hyung Cho, Seung-Hun Lee, Jeffrey W. Lynn, Daniel G. Nocera, and Young S. Lee. Spin chirality on a two-dimensional frustrated lattice. *Nature Materials*, 4(4):323–328, April 2005.

[16] T. Yildirim and A. B. Harris. Magnetic structure and spin waves in the kagomé jarosite compound $KFe_3(SO_4)_2(OH)_6$. *arXiv.org*, Mar 10 2006.

[17] T. Inami, T. Morimoto, M. Nishiyama, S. Maegawa, Y. Oka, and H. Okumura. Magnetic ordering in the kagomé lattice antiferromagnet $KCr_3(OH)_6(SO_4)_2$. *Physical Review B*, 64(5), July 2001.

[18] Jan N Reimers and A. J Berlinsky. Order by disorder in the classical heisenberg kagomé antiferromagnet. *Physical review. B, Condensed matter*, 48(13):9539–9554, 1993.

[19] S.-H. Lee, C. Broholm, M. F. Collins, L. Heller, A. P. Ramirez, C. Kloc, E. Bucher, R. W. Erwin, and N. Lacevic. Less than 50% sublattice polarization in an insulating S=3/2 kagome' antiferromagnet at low T. *Physical Review B*, 56(13):8091–8097, October 1997.

[20] Tian-Heng Han, Joel S. Helton, Shaoyan Chu, Daniel G. Nocera, Jose A. Rodriguez-Rivera, Collin Broholm, and Young S. Lee. Fractionalized excitations in the spin-liquid state of a kagome-lattice antiferromagnet. *Nature*, 492(7429):406–410, December 2012.

[21] P. W. Anderson. Resonating valence bonds: A new kind of insulator? *Materials Research Bulletin*, 8(2):153 – 160, 1973.

[22] John L. Jambor. Nomenclature of the alunite supergroup. *The Canadian Mineralogist*, 37(6):1323–1341, 1999.

[23] Peter Atkins and Ronald Friedman. *Molecular Quantum Mechanics*. Oxford University Press, 2005.

[24] A. S. Wills, A. Harrison, C. Ritter, and R. I. Smith. Magnetic properties of pure and diamagnetically doped jarosites: Model *kagomé* antiferromagnets with variable coverage of the magnetic lattice. *Phys. Rev. B*, 61(9):6156–6169, March 2000.

[25] Susan A. Welch, Andrew G. Christy, Dirk Kirste, Sara G. Beavis, and Fern Beavis. Jarosite dissolution I — Trace cation flux in acid sulfate soils. *Chemical Geology*, 245(3-4):183–197, November 2007.

[26] M. E. Elwood Madden, R. J. Bodnar, and J. D. Rimstidt. Jarosite as an indicator of water-limited chemical weathering on Mars. *Nature*, 431(7010):821–823, October 2004.

[27] Maria-Ondina Figueiredo and Teresa Pereira da Silva. The Positive Environmental Contribution of Jarosite by Retaining Lead in Acid Mine Drainage Areas. *Int J Environ Res Public Health*, 8(5):1575–1582, May 2011.

[28] Elisabeth Grube, Andrew S. Lipton, and Ulla Gro Nielsen. Identification of hydrogen species in alunite-type minerals by multi-nuclear solid-state NMR spectroscopy. *Physics and Chemistry of Minerals*, September 2018.

[29] Ulla Gro Nielsen, Juraj Majzlan, and Clare P. Grey. Determination and Quantification of the Local Environments in Stoichiometric and Defect Jarosite by Solid-State ^{2}H NMR Spectroscopy. *Chemistry of Materials*, 20(6):2234–2241, March 2008.

[30] U. G. Nielsen, J. Majzlan, B. Phillips, M. Ziliox, and C. P. Grey. Characterization of defects and the local structure in natural and synthetic alunite (K, Na, $H_3O)Al_3(SO_4)_2(OH)_6$ by multi-nuclear solid-state NMR spectroscopy. *American Mineralogist*, 92(4):587–597, April 2007.

[31] Anthony R. West. *Basic Solid State Chemistry*. Wiley, 2001.

[32] Mathilde B. Sørensen. Frustrated magnetism in chromium jarosites $KCr_3(OH)_6(SO_4)_2$, 2019. Bachelor thesis.

[33] Andrew S. Wills and Andrew Harrison. Structure and magnetism of hydronium jarosite, a model kagomé antiferromagnet. *J. Chem. Soc., Faraday Trans.*, 92(12):2161–2166, 1996.

[34] Daniel Grohol and Daniel G. Nocera. Hydrothermal oxidation-reduction methods for the preparation of pure and single crystalline alunites: Synthesis and characterization of a new series of vanadium jarosites. *Journal of the American Chemical Society*, 124(11):2640–2646, March 2002.

[35] Daniel G. Nocera, Bart M. Bartlett, Daniel Grohol, Dimitris Papoutsakis, and Matthew P. Shores. Spin Frustration in 2d Kagomé Lattices: A Problem for Inorganic Synthetic Chemistry. *Chemistry - A European Journal*, 10(16):3850–3859, August 2004.

[36] Koji Okuta, Shigeo Hara, Hirohiko Sato, Yasuo Narumi, and Koichi Kindo. Observation of 1/3 Magnetization-Plateau-Like Anomaly in $S =3/2$ Perfect Kagomé Lattice Antiferromagnet $KCr_3(OH)_6(SO_4)_2$ (Cr-jarosite). *Journal of the Physical Society of Japan*, 80(6):063703, June 2011.

[37] M. G. Townsend, G. Longworth, and E. Roudaut. Triangular-spin, kagome plane in jarosites. *Phys. Rev. B*, 33:4919–4926, Apr 1986.

[38] A. Keren, K. Kojima, L. P. Le, G. M. Luke, W. D. Wu, Y. J. Uemura, M. Takano, H. Dabkowska, and M. J. P. Gingras. Muon-spin-rotation measurements in the kagomé lattice systems: Cr-jarosite and fe-jarosite. *Phys. Rev. B*, 53:6451–6454, Mar 1996.

[39] C. L. Lengauer, G. Giester, and E. Irran. $KCr_3(OH)_6(SO_4)_2$: Synthesis, characterization, powder diffraction data, and structure refinement by the Rietveld technique and a compilation of alunite-type compounds. *Powder Diffraction*, 9(4):265–271, 1994.

[40] Tamaki Morimoto, Masahide Nishiyama, Satoru Maegawa, and Yoshio Oka. Magnetization of New Kagomé Lattice Antiferromagnets: Cr-Jarosites, $ACr_3(OH)_6(SO_4)_2$ [A = Na, K, Rb, NH$_4$]. *Journal of the Physical Society of Japan*, 72(8):2085–2090, August 2003.

[41] Susumu Okubo, Ryohei Nakata, Shohei Ikeda, Naoki Takahashi, Takahiro Sakurai, Wei-Min Zhang, Hitoshi Ohta, Tokuro Shimokawa, Tôru Sakai, Koji Okuta, Shigeo Hara, and Hirohiko Sato. Dzyaloshinsky–Moriya Interaction and the Ground State in $S = 3/2$ Perfect Kagome Lattice Antiferromagnet $KCr_3(OH)_6(SO_4)_2$ (Cr-Jarosite) Studied by X-Band and High-Frequency ESR. *Journal of the Physical Society of Japan*, 86(2):024703, February 2017.

[42] Daniel Grohol, Daniel G. Nocera, and Dimitris Papoutsakis. Magnetism of pure iron jarosites. *Physical Review B*, 67(6):064401, February 2003.

[43] Bart M. Bartlett and Daniel G. Nocera. Long-Range Magnetic Ordering in Iron Jarosites Prepared by Redox-Based Hydrothermal Methods. *Journal of the American Chemical Society*, 127(25):8985–8993, June 2005.

[44] J. E. Dutrizac and S. Kaiman. Synthesis and properties of jarosite-type compounds. *Canadian Mineralogist*, 14:151–158, 1976.

[45] Melinda J. Duer. *Solid-state NMR spectroscopy: principles and applications*. Blackwell Science Ltd, 2002.

[46] Horst Friebolin. *Basic One- and Two-Dimensional NMR Spectroscopy*. Wiley, 2005.

[47] Timothy D. W. Claridge. Chapter 2 - Introducing high-resolution NMR. In *High-Resolution NMR Techniques in Organic Chemistry*, volume 27 of *Tetrahedron Organic Chemistry Series*, pages 11 – 34. Elsevier, 2009.

[48] Kim Lefmann. Supplementary notes for the magnetism course, KU and DTU, Spring 2017.

[49] E. L. Hahn. Spin echoes. *Phys. Rev.*, 80:580–594, Nov 1950.

[50] David D. Laws, Hans-Marcus L. Bitter, and Alexej Jerschow. Solid-state nmr spectroscopic methods in chemistry. *ChemInform*, 33(47):278–278, 2002.

[51] Cory M. Widdifield and Robert W. Schurko. Understanding chemical shielding tensors using group theory, MO analysis, and modern density-functional theory. *Concepts in Magnetic Resonance Part A*, 34A(2):91–123, 2009.

[52] Robert A. Meyers. *Encyclopedia of Analytical Chemistry*. Wiley, 2000.

[53] Ae Ja Kim, Frank R Fronczek, Leslie G Butler, Shixiong Chen, and Ellen A Keiter. Deuterium quadrupole coupling constants and asymmetry parameters in bridging metal hydride complexes. *Journal of the Amarican Chemical Society*, 113:9090–9096, 1991.

[54] Francis Spencer Millett and Benjamin P. Dailey. Nmr determination of some deuterium quadrupole coupling constants in nematic solutions. *The Journal of Chemical Physics*, 56(7):3249–3256, 1972.

[55] Jasim M. A. Al-Rawi, George Q. Behnam, and Nihad I. Taha. Deuterium nuclear magnetic resonance spectroscopy. larmor frequency ratio, referencing and chemical shift. *Organic Magnetic Resonance*, 16(3):198–201, 1981.

[56] I. J. Lowe. Free induction decays of rotating solids. *Phys. Rev. Lett.*, 2:285–287, Apr 1959.

[57] Perkin Elmer. *A Beginner's Guide to Thermigravimetric Analysis*.

[58] Peter Atkins, Julio de Paula, and Ronald Friedman. *Physical Chemistry*. Oxford University Press, 2014.

[59] Elisabeth Grube. Investigation of H_xO_y species in alunite-type minerals and other iron sulphates. Master's thesis, University of Southern Denmark, 2011.

[60] Janice L. Bishop and Enver Murad. The visible and infrared spectral properties of jarosite and alunite. *American Mineralogist*, 90(7):1100–1107, 2005.

[61] Arne M. Vandenbroucke. *Abatement of volatile organic compounds by combined use of non-thermal plasma and heterogeneous catalysis*. PhD thesis, Ghent University, 2015.

[62] Dana A. Powers, George R. Rossman, Harvey J. Schugar, and Harry B. Gray. Magnetic behavior and infrared spectra of jarosite, basic iron sulfate, and their chromate analogs. *Journal of Solid State Chemistry*, 13(1-2):1–13, February 1975.

[63] Pamela J. Murphy, Adrian M.L. Smith, Karen A. Hudson-Edwards, William E. Dubbin, and Kate Wright. Raman and IR Spectroscopic Studies of Alunite-Supergroup Compounds Containing Al, Cr3+, Fe3+ and V3+ at the B Site. *The Canadian Mineralogist*, 47(3):663–681, 2009.

[64] Christian W. Huck. *Near-Infrared Spectroscopy in Natural Product Research*, pages 1–18. American Cancer Society, 2014.

[65] Richard Rennie and C. K. Loong. *Elements of Slow-Neutron Scattering*. Cambridge University Press, 2015.

[66] R. J. Barlow. *Statistics - A Guide to the Use of Statistical Methods in the Physical Sciences*. Wiley, 1999.

[67] Yang Leng. *Materials Characterization*. Wiley, 2008.

[68] Lumen learning wbsite. `https://courses.lumenlearning.com/suny-microbiology/`. Accessed: 28-09-2020.

[69] B. T. M. Willis and C. J. Carlile. *Experimental Neutron Scattering*. Oxford University Press, 2009.

[70] Bahman Zohuri. *Neutronic Analysis For Nuclear Reactor Systems*. Springer, 2019.

[71] Psi website. `http://https://psi.ch/en/media/the-sinq-neutron-source`. Accessed: 14-07-2020.

[72] Isis website. `http://isis.stfc.ac.uk`. Accessed: 30-09-2019.

[73] J. M. Carpenter and Jonathan Law. *A Dictionary of Physics*. Oxford University Press, 2019.

[74] MARI instrument website. `https://www.isis.stfc.ac.uk/Pages/mari.aspx`. Accessed: 10-08-2020.

[75] MARI technical specifications website. `https://www.isis.stfc.ac.uk/Pages/Let-technical-information.aspx`. Accessed: 16-09-2020.

[76] N. Violini, J. Voight, and T. Brückel. Investigation of timing and positioning of T_0 choppers at long pulse neutron sources. *Proceedings of the 21st Meeting of the International Collaboration on Advanced Neutron Sources (ICANS XXI)*, pages 272–277, September 2014.

[77] LET technical specifications website. `https://www.isis.stfc.ac.uk/Pages/MARI-technical-specification.aspx`. Accessed: 16-09-2020.

[78] LET instrument website. `https://www.isis.stfc.ac.uk/Pages/Let.aspx`. Accessed: 10-08-2020.

[79] R. I. Bewley, J. W. Taylor, and S. M. Bennington. LET, a cold neutron multi-disk chopper spectrometer at ISIS. *Nuclear Instruments and Methods in Physics Research Section A: Accelerators, Spectrometers, Detectors and Associated Equipment*, 637(1):128 – 134, 2011.

[80] Sofie Janas, Mathilde Borup Sørensen, Anders Bruhn Arndal Andersen, Mikkel Juelsholt, Martin Boehm, Kasper Steen Pedersen, Kirsten Marie Ørnsbjerg Jensen, Kim Lefmann, and Ulla Gro Nielsen. Structural characterization and magnetic properties of chromium jarosite $KCr_3(OD)_6(SO_4)_2$. *Accepted in Phys. Chem. Chem. Phys.*, 2020.

[81] W. Kunda and H. Veltman. Decomposition of jarosite. *Metallurgical Transactions B*, 10(3):439–446, September 1979.

[82] J. E. Dutrizac and T. T. Chen. Factors affecting the precipitation of chromium(III) in jarosite-type compounds. *Metall and Materi Trans B*, 36(1):33–42, February 2005.

[83] Mikkel Juelsholt, PhD student at University of Copenhagen. Personal communication.

[84] Koichi Momma and Fujio Izumi. *VESTA3* for three-dimensional visualization of crystal, volumetric and morphology data. *Journal of Applied Crystallography*, 44(6):1272–1276, Dec 2011.

[85] A. S Wills, A Harrison, S. A. M Mentink, T. E Mason, and Z Tun. Magnetic correlations in deuteronium jarosite, a model s = 5/2 kagomé antiferromagnet. *Europhysics Letters (EPL)*, 42(3):325–330, may 1998.

[86] J. E. Greedan, M. Bieringer, J. F. Britten, D. M. Giaquinta, and H. C. zur Loye. Synthesis, Crystal Structure, and Unusual Magnetic Properties of InMnO3. *Journal of Solid State Chemistry*, 116(1):118–130, April 1995.

[87] B. E. Warren. X-Ray Diffraction in Random Layer Lattices. *Phys. Rev.*, 59(9):693–698, May 1941.

[88] Andrey Varlamov and Lev G. Aslamazov. *The Wonders of Physics*. World Scientific Publishing Company, 2012.

[89] K. F. Riley and M. P. Hobson. *Essential Mathematical Methods for the Physical Sciences*. Cambridge University Press, 2011.

[90] Sofie Janas, Jakob Lass, Ana-Elena Tutueanu, Morten L. Haubro, Christof Niedermayer, Uwe Stuhr, Guangyong Xu, Dharmalingam Prabhakaran, Pascale P. Deen, Sonja Holm-Dahlin, and Kim Lefmann. Classical spin liquid or extended critical range in h-$YMnO_3$? *Submitted to Physical Review Letters*, 2020.

[91] Tapan Chatterji. *Neutron scattering from magnetic materials*. Elsevier Science, 2006.

[92] Jens Jensen and Allan R. Mackintosh. *Rare Earth Magnetism - Structures and Excitations*. Clarendon Press, 1991.

[93] M. Nishiyama, T. Morimoto, S. Maegawa, T. Inami, and Y. Oka. Magnetic ordering and fluctuation in kagome lattice antiferromagnets, Fe and Cr jarosites. *Canadian Journal of Physics*, 79(11-12):1511–1516, 2001.

[94] T. Inami, M. Nishiyama, S. Maegawa, and Y. Oka. Magnetic structure of the kagomé lattice antiferromagnet potassium jarosite $kfe_3(OH)_6(SO_4)_2$. *Phys. Rev. B*, 61:12181–12186, May 2000.

[95] Ningxin Jiang, Arun Ramanathan, John Bacsa, and Henry S. La Pierre. Synthesis of a d1-titanium fluoride kagome lattice antiferromagnet. *Nature Chemistry*, 12(8):691–696, August 2020.

Appendix

A   Sample

Sample	Amount [g]
SLL-2	1.3938
SLL-3	1.0798
SLL-4	0.2247
SLL-5	1.4282
SLL-6	1.4472
SLL-7	1.3810
Combined sample	6.9305

Table 10: Mass contribution from each subsample to the combined sample.

A.1   Notes to samples

SLL-1 and SLL-2 The oven turned off during the heating process, so the pressure bomb was moved to a new oven approximately one day after it had initially been put in the oven. The bomb then stayed 5 days in the new oven.

SLL-1 This sample was not rinsed, therefore leftover compounds from the mixture is mixed with the Cr-jarosite powder.

SLL-2 This sample was primarily rinsed with D_2O, but a small part of it was rinsed with H_2O. $0.0045g$ ($< 1\%$ of synthesized mass) leftover Cr pellets was removed from the powder.

SLL-4 During PXRD the sample was spilled within the instrument and therefore lost. The amount of lost sample is approximately $0.5g$.

A subset of the sample was left to dry in an oven for two days, in order to determine if the original sample had been dried properly. This subset is packed in a different sample holder and labeled SLL-4t. $0.2552g$ ($\approx 18\%$ of synthesized mass) leftover Cr pellets was removed from the powder.

SLL-6 and SLL-7 Was in the oven 7 days instead of 5 days. Dried overnight instead of a few hours.

SLL-6 $0.0686g$ ($\approx 4\%$ of synthesized mass) leftover Cr pellets was removed from the powder.

SLL-7 $0.0379g$ ($\approx 2\%$ of synthesized mass) leftover Cr pellets was removed from the powder.

B NMR measurements

NMR spectra of samples SLL-2 to SLL-7.
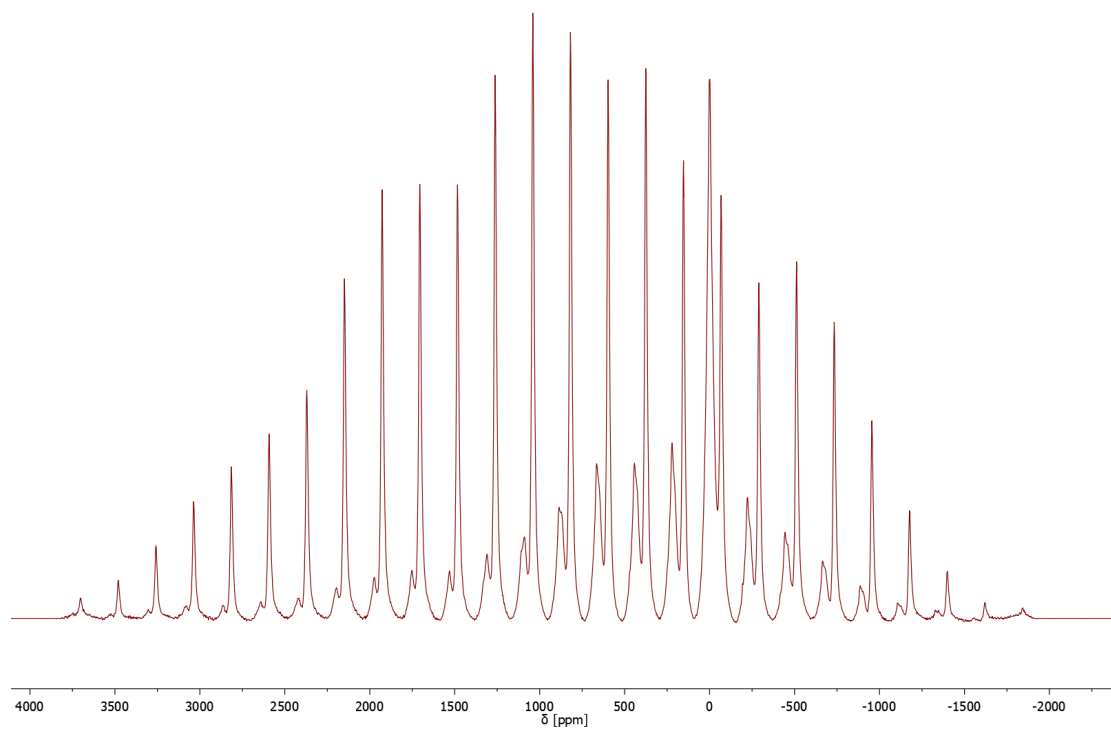
Figure 51: NMR of sample SLL-2.
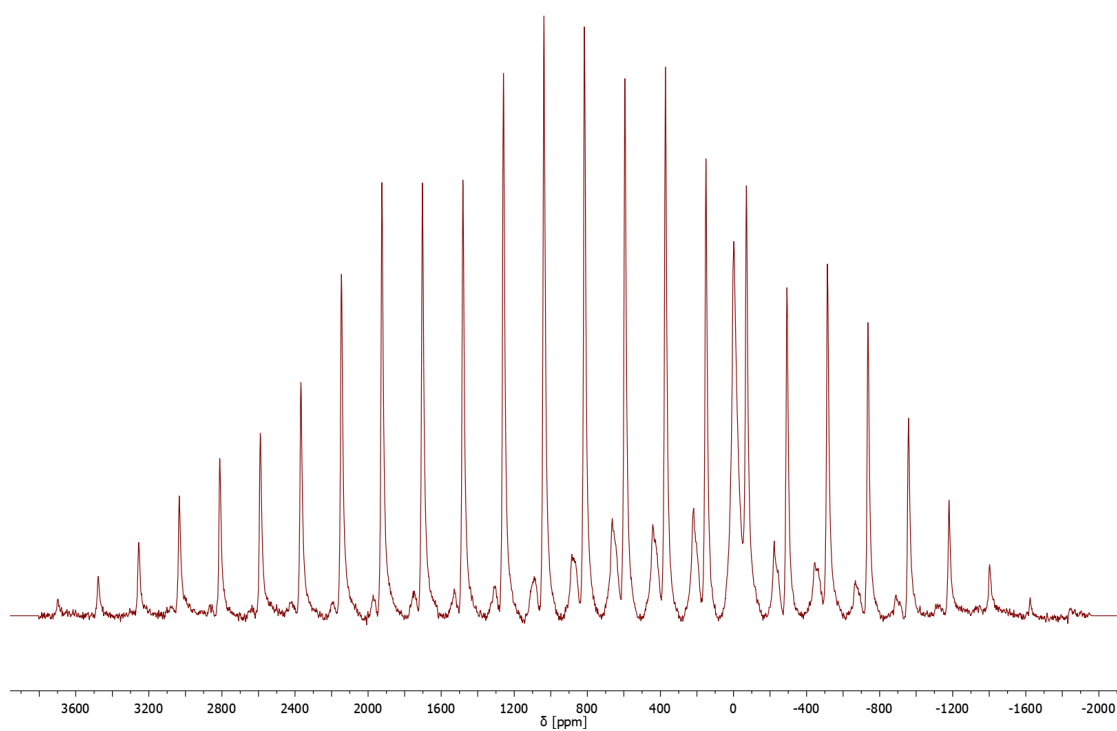
Figure 52: NMR of sample SLL-3.
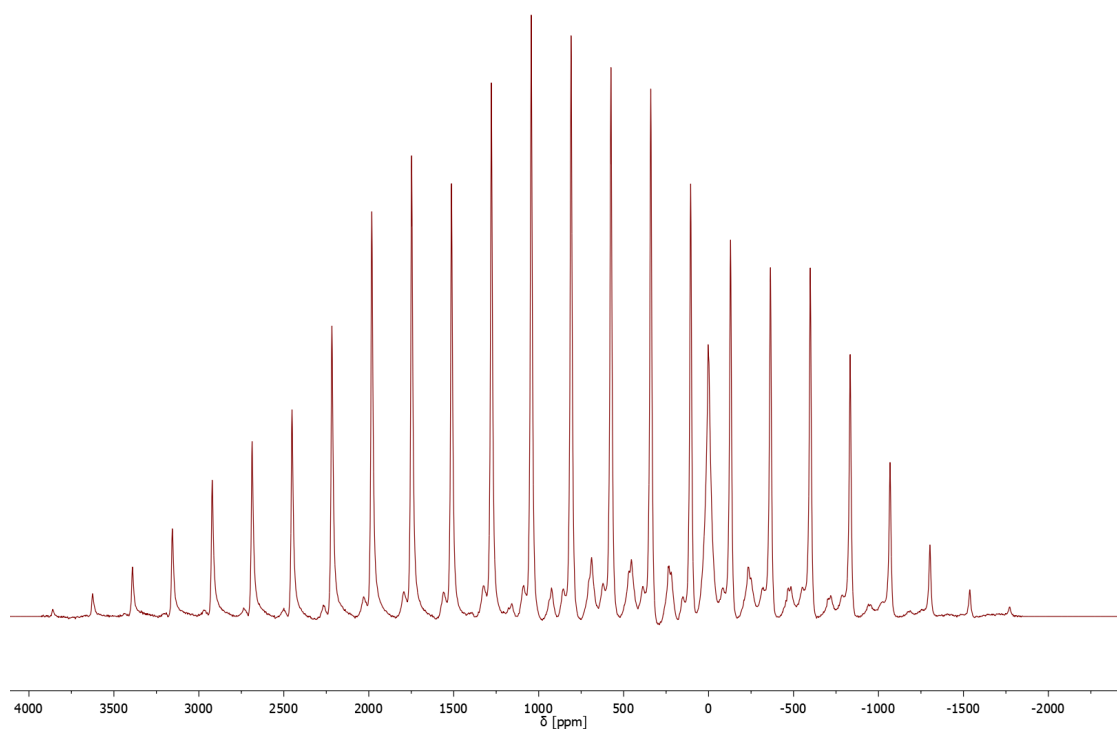
Figure 53: NMR of sample SLL-4.
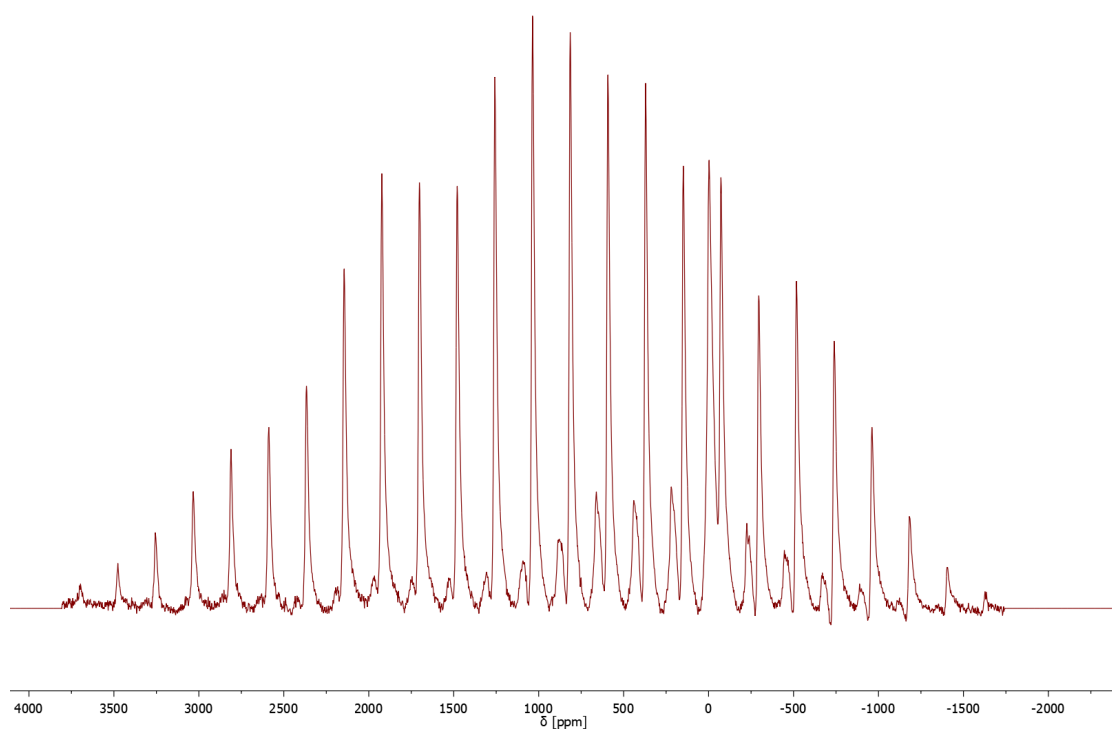
Figure 54: NMR of sample SLL-5.
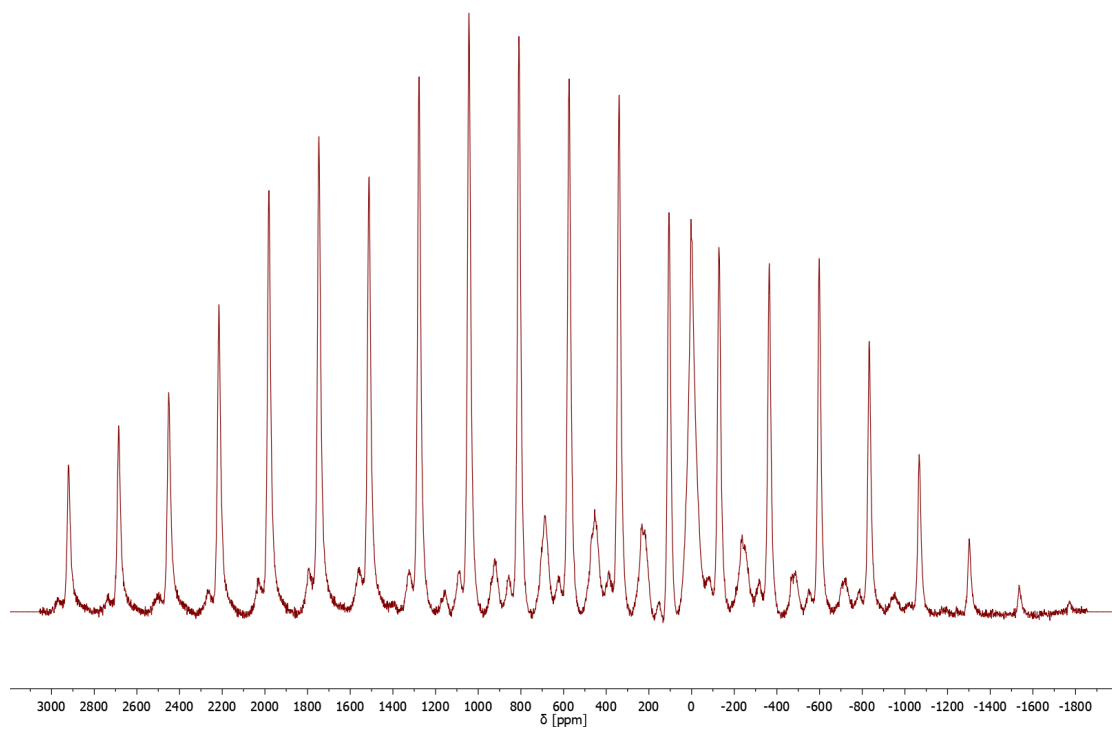
Figure 55: NMR of sample SLL-6.
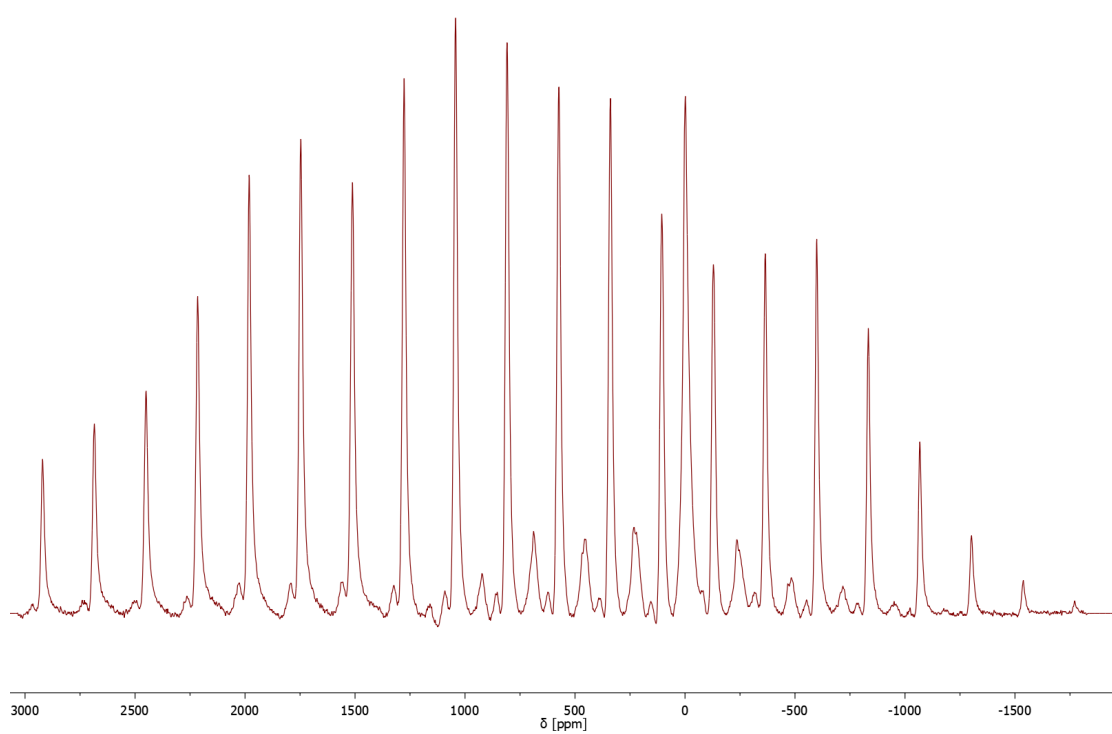
Figure 56: NMR of sample SLL-7.
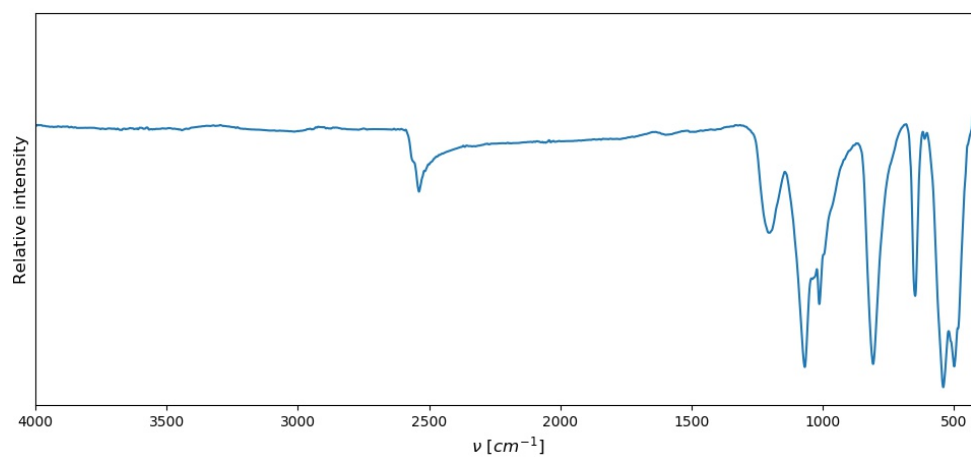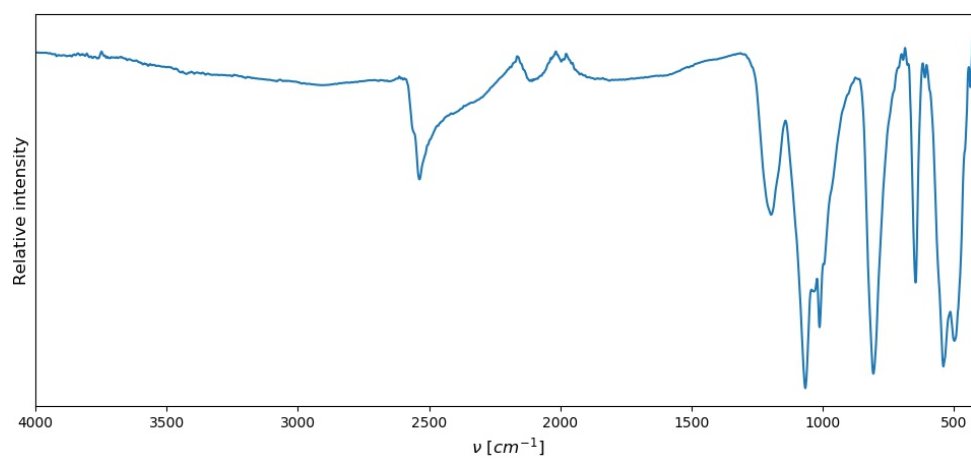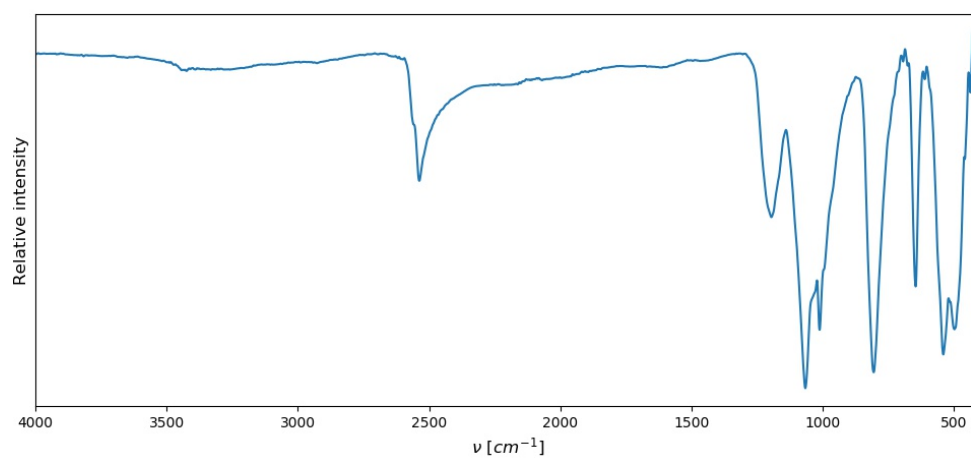
C IR measurements

IR - SLL-1
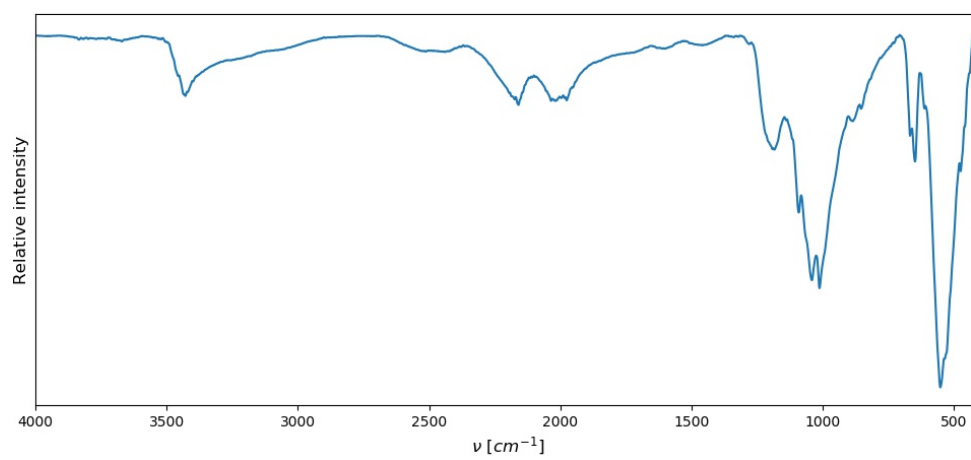
IR - SLL-2
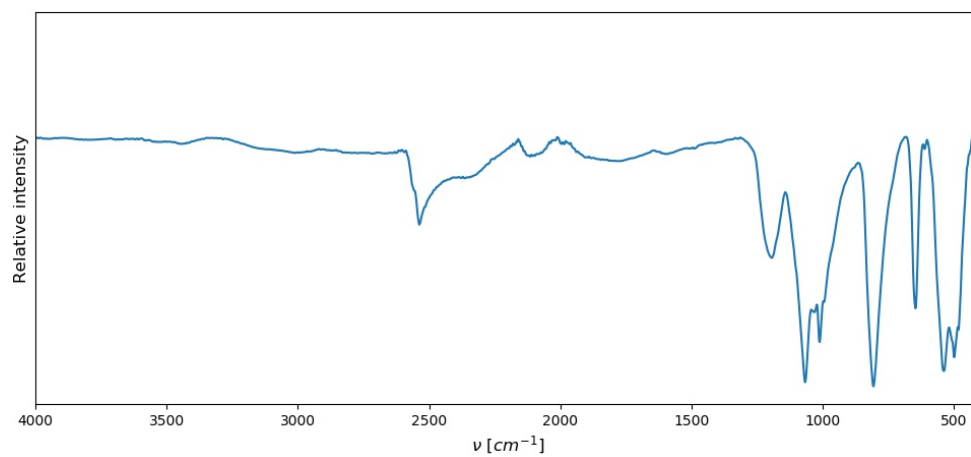
IR - SLL-3
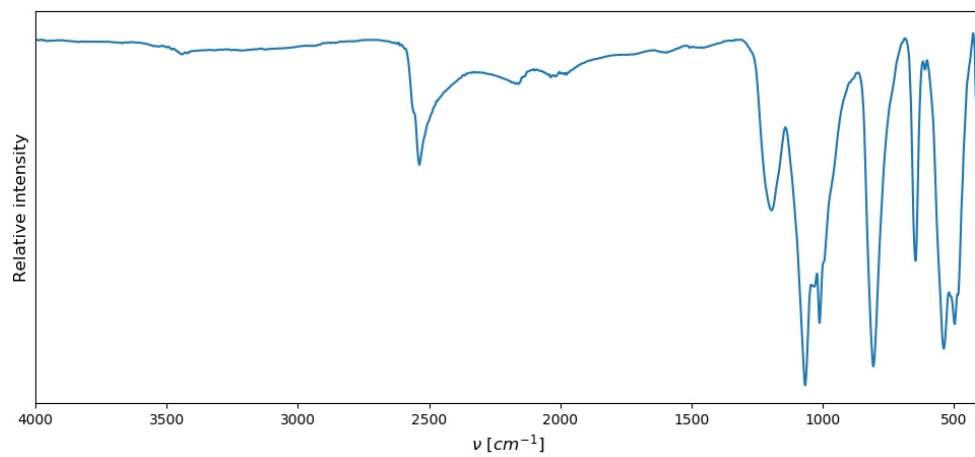
IR - SLL-4
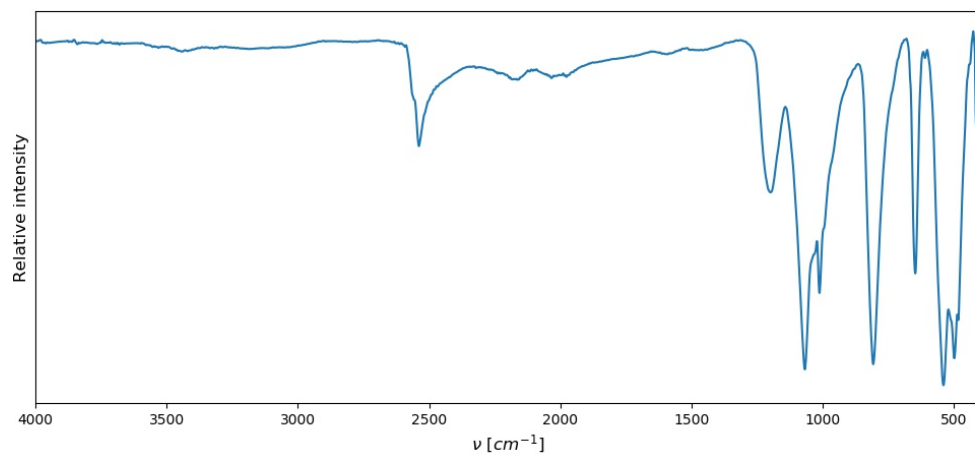
IR - SLL-5

IR - SLL-6

IR - SLL-7

D   TGA measurements

TGA curves and quantified mass loss steps for all subsamples.
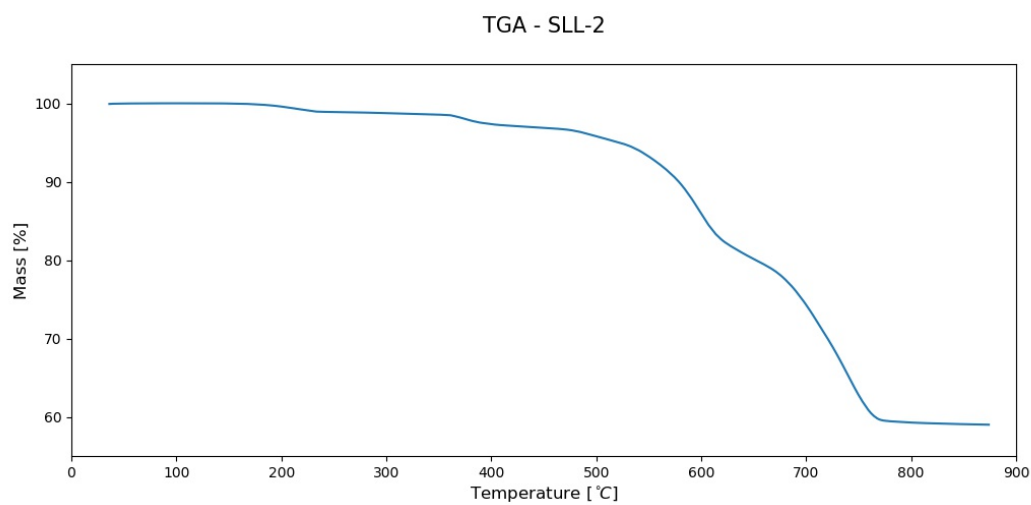
TGA - SLL-2

SLL-2

Mass loss no.	Temperature	Mass [mg]	Mass percentage [%]
1	$300°C$	61.93	98.7
2	$450°C$	60.77	96.9
3	$650°C$	50.22	80.1
4	$800°C$	37.17	59.3

TGA - SLL-3
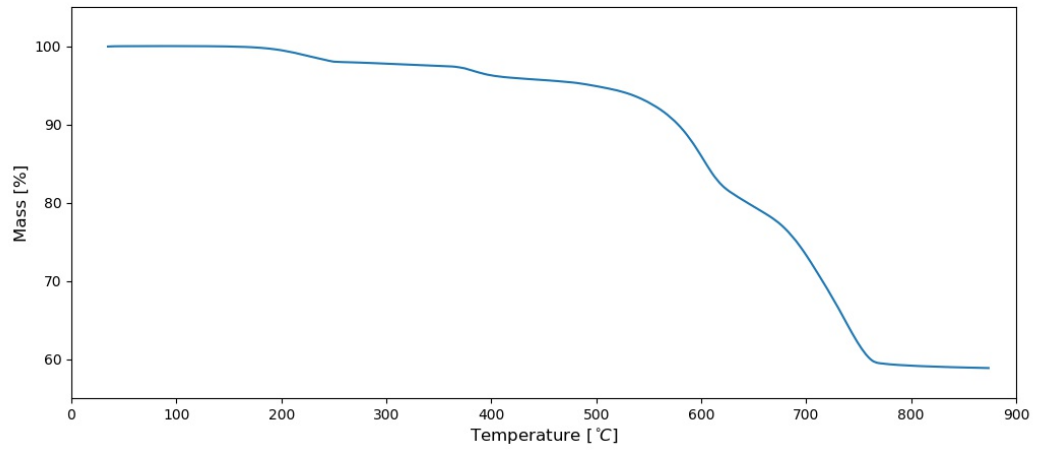
SLL-3

| Mass loss no.	Temperature	Mass [mg]	Mass percentage [%]
1	$300°C$	48.08	97.8
2	$450°C$	47.04	95.7
3	$650°C$	39.07	79.5
4	$800°C$	29.09	59.2

TGA - SLL-4
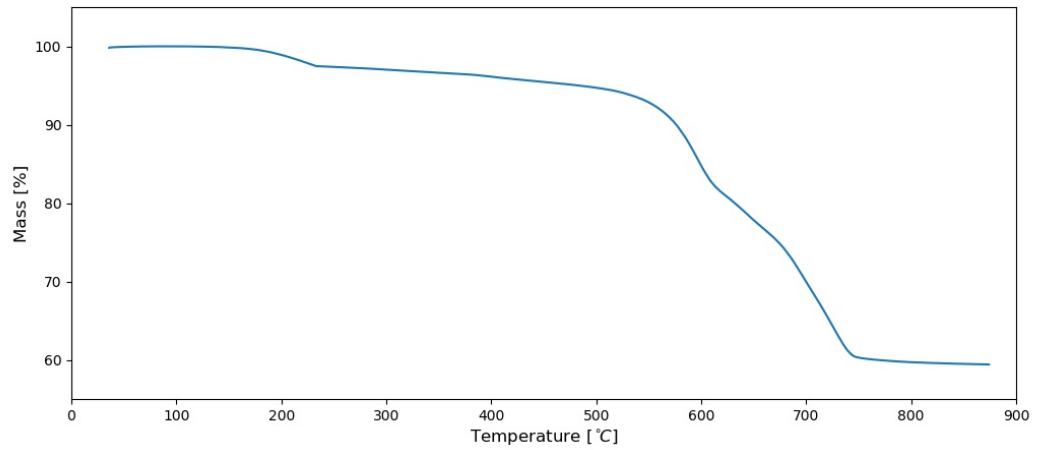
SLL-4

Mass loss no.	Temperature	Mass [mg]	Mass percentage [%]
1	$300°C$	21.24	97.0
2	$650°C$	17.03	77.8
3	$800°C$	13.07	59.7

TGA - SLL-5
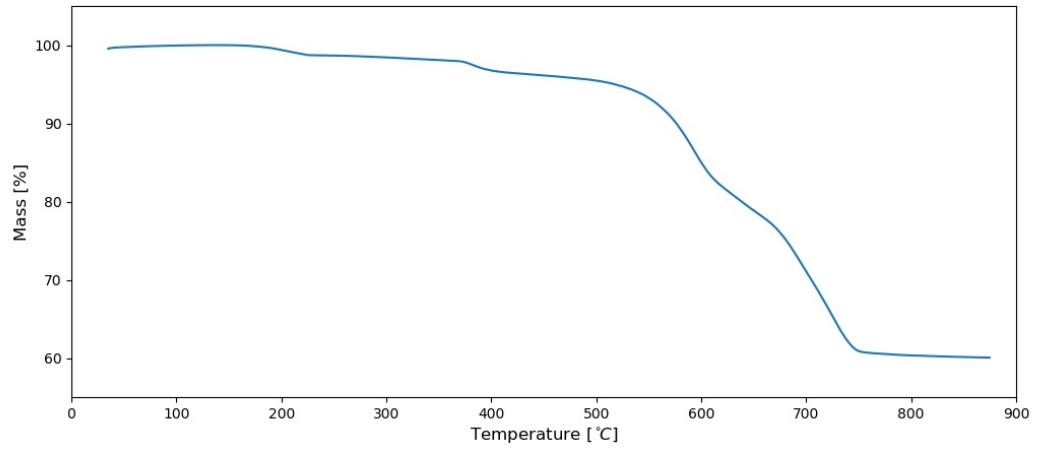
SLL-5

Mass loss no.	Temperature	Mass [mg]	Mass percentage [%]
1	$300°C$	26.69	98.4
2	$450°C$	26.06	96.1
3	$650°C$	21.38	78.8
4	$800°C$	16.36	60.3

TGA - SLL-6
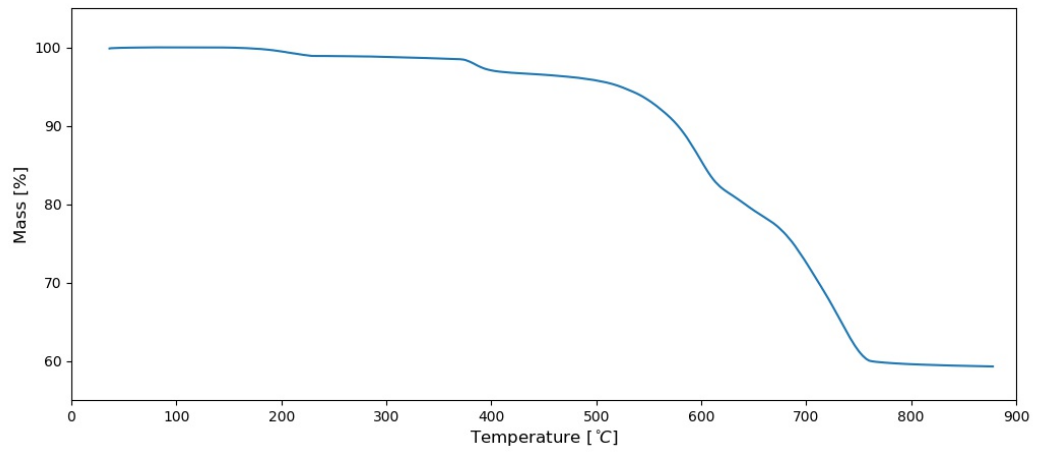
SLL-6

Mass loss no.	Temperature	Mass [mg]	Mass percentage [%]
1	$300°C$	37.65	98.8
2	$450°C$	36.78	96.5
3	$650°C$	30.18	79.2
4	$800°C$	22.71	59.6

TGA - SLL-7
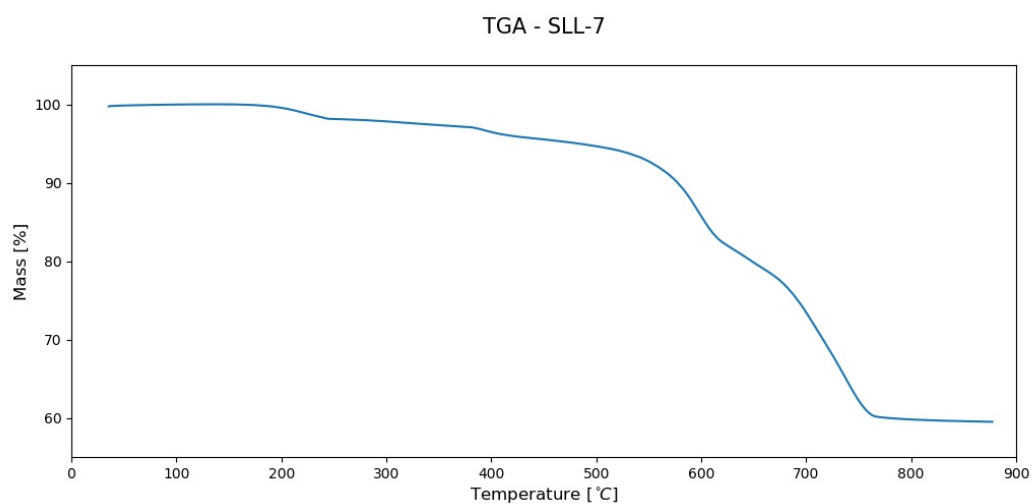
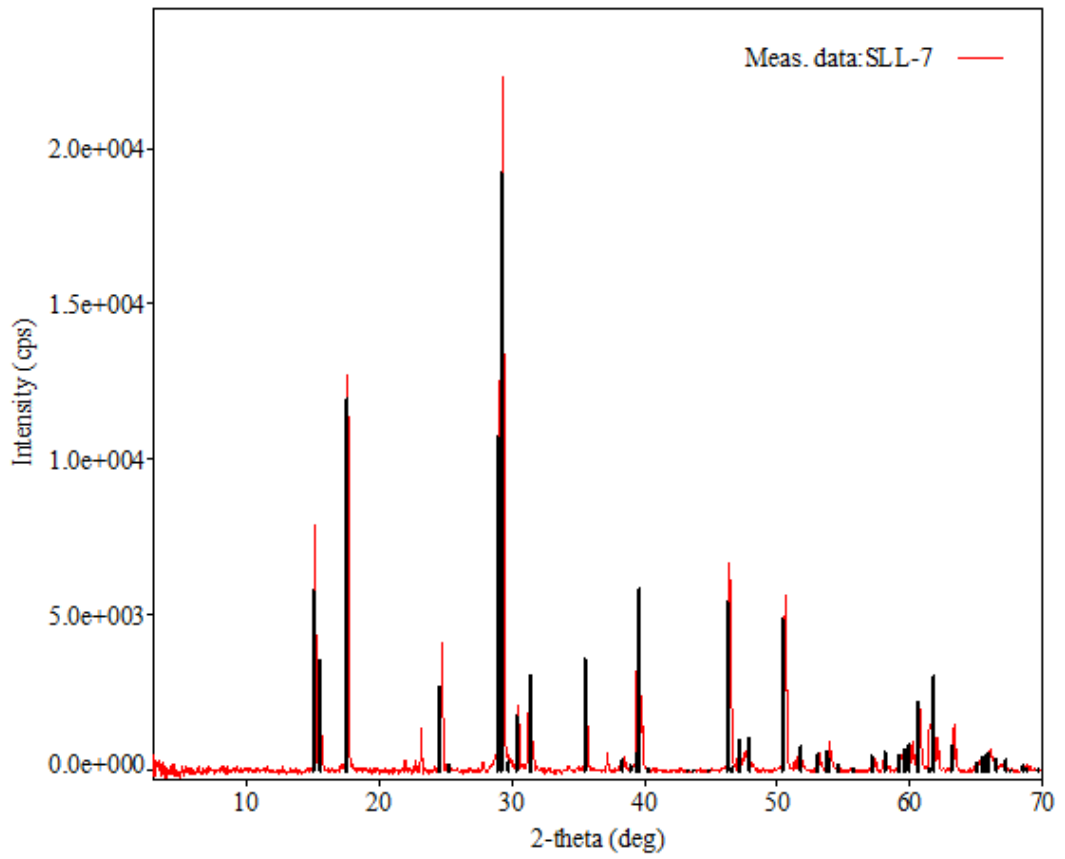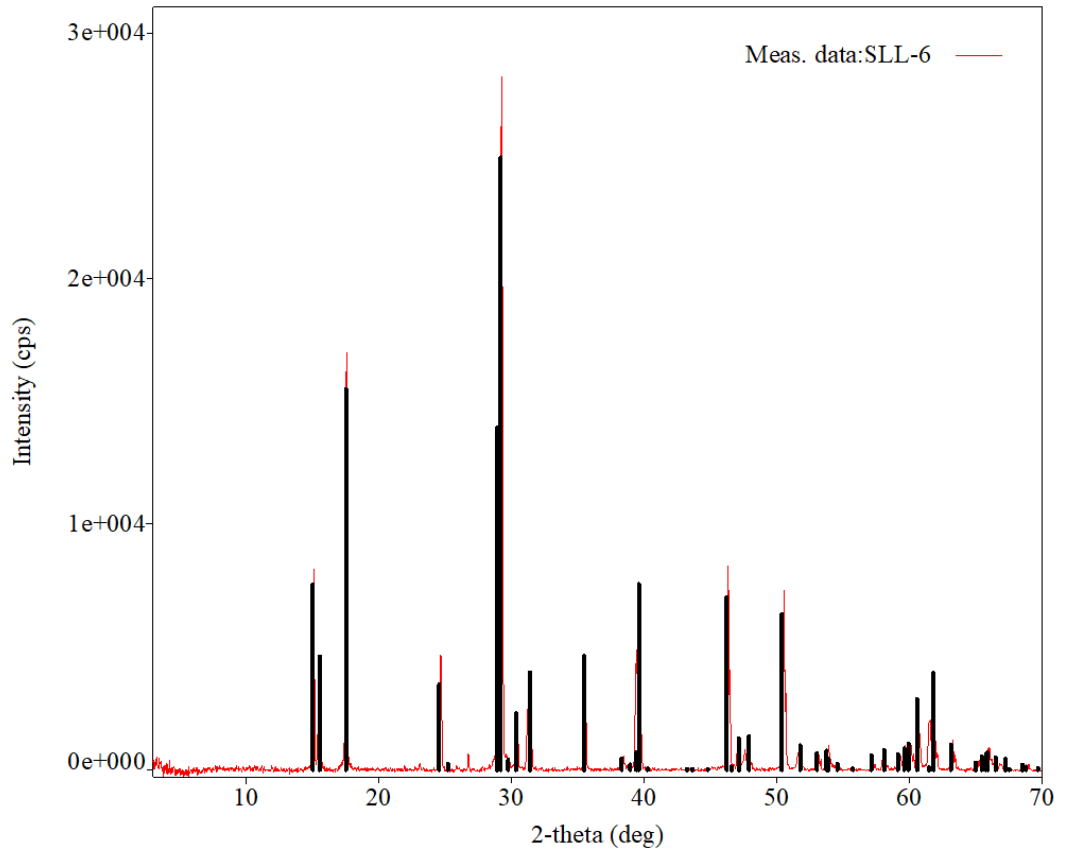| SLL-7			
Mass loss no.	Temperature	Mass [mg]	Mass percentage [%]
1	$300°C$	41.18	97.8
2	$450°C$	40.21	95.5
3	$650°C$	33.58	79.8
4	$800°C$	25.17	59.8

E   PXRD measurements

PXRD spectra of subsamples plotted with the peak position of a reference Cr-jarosite from [39].
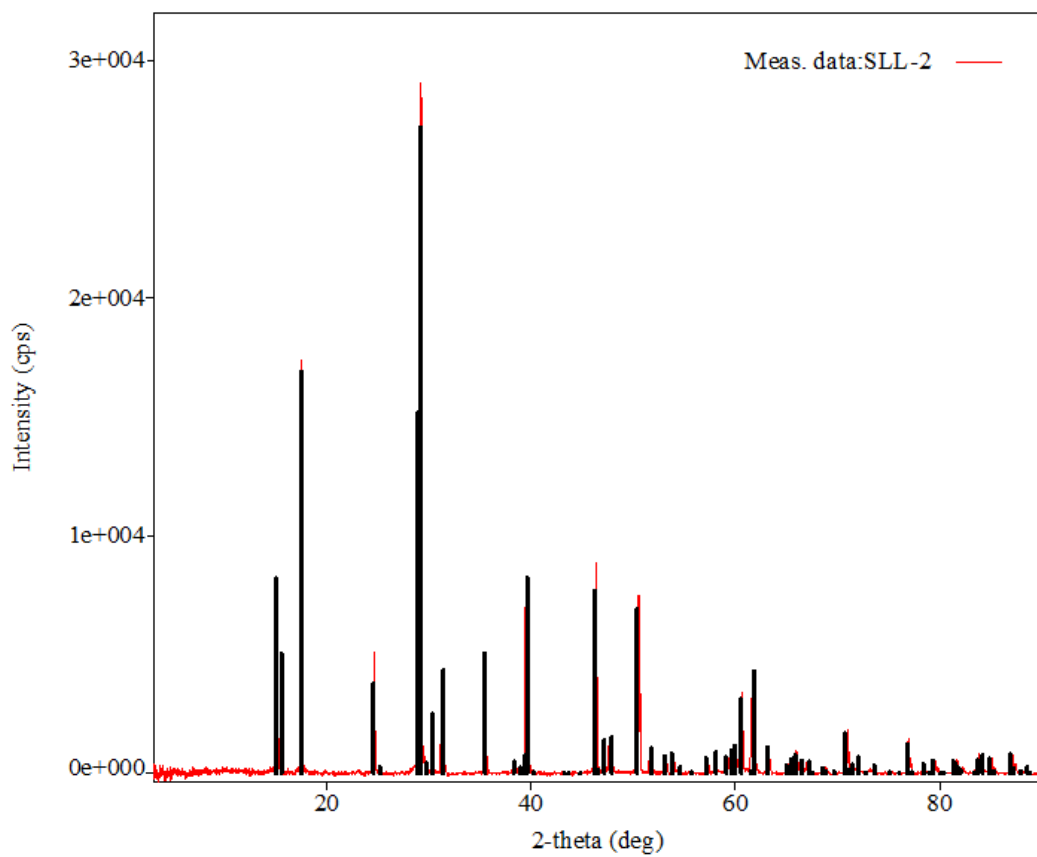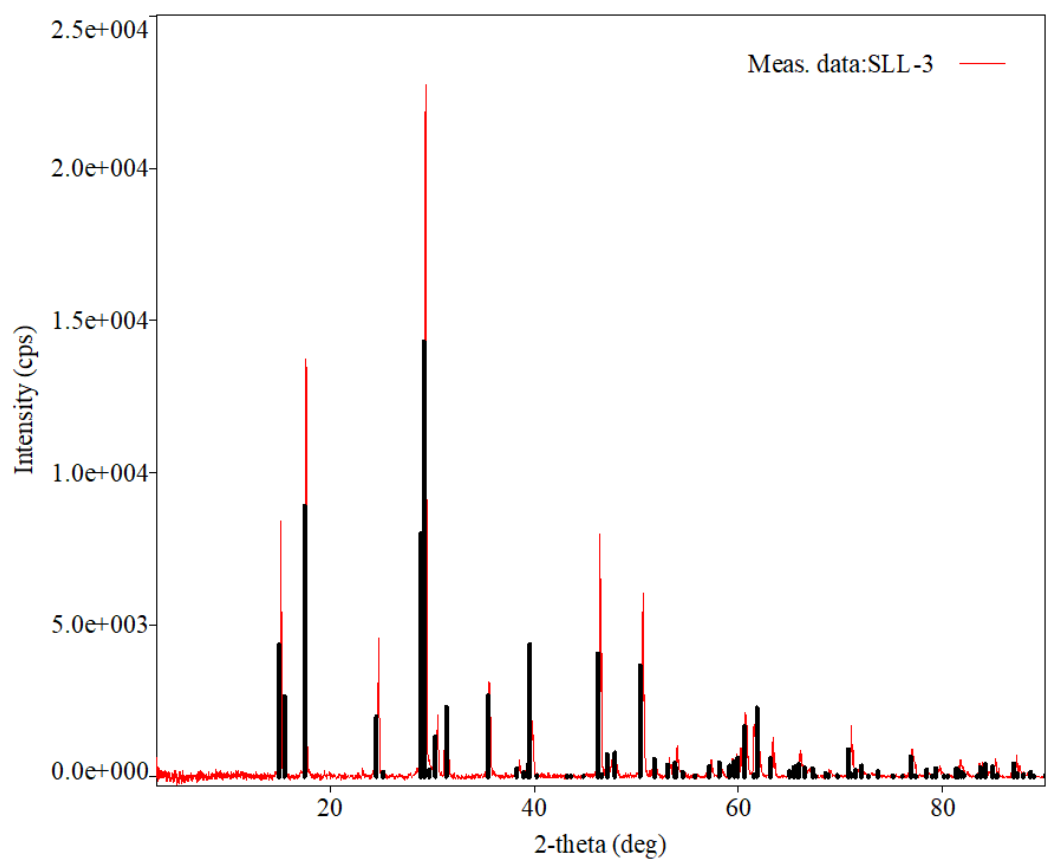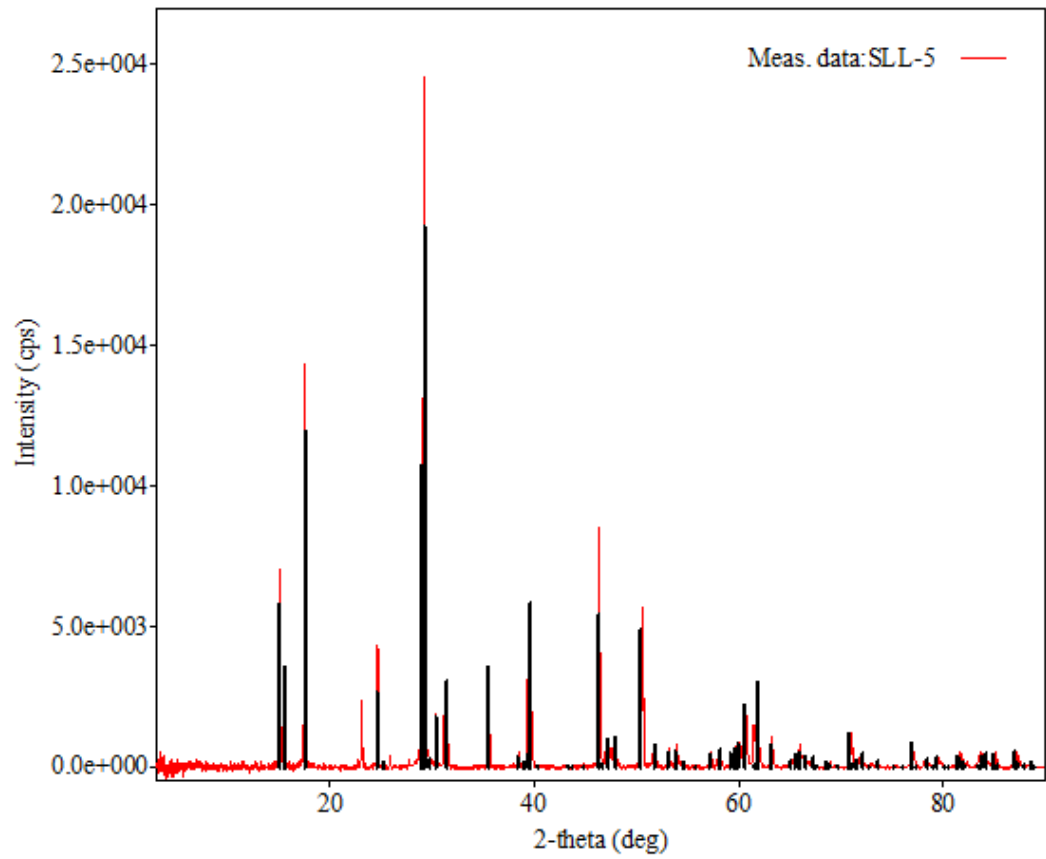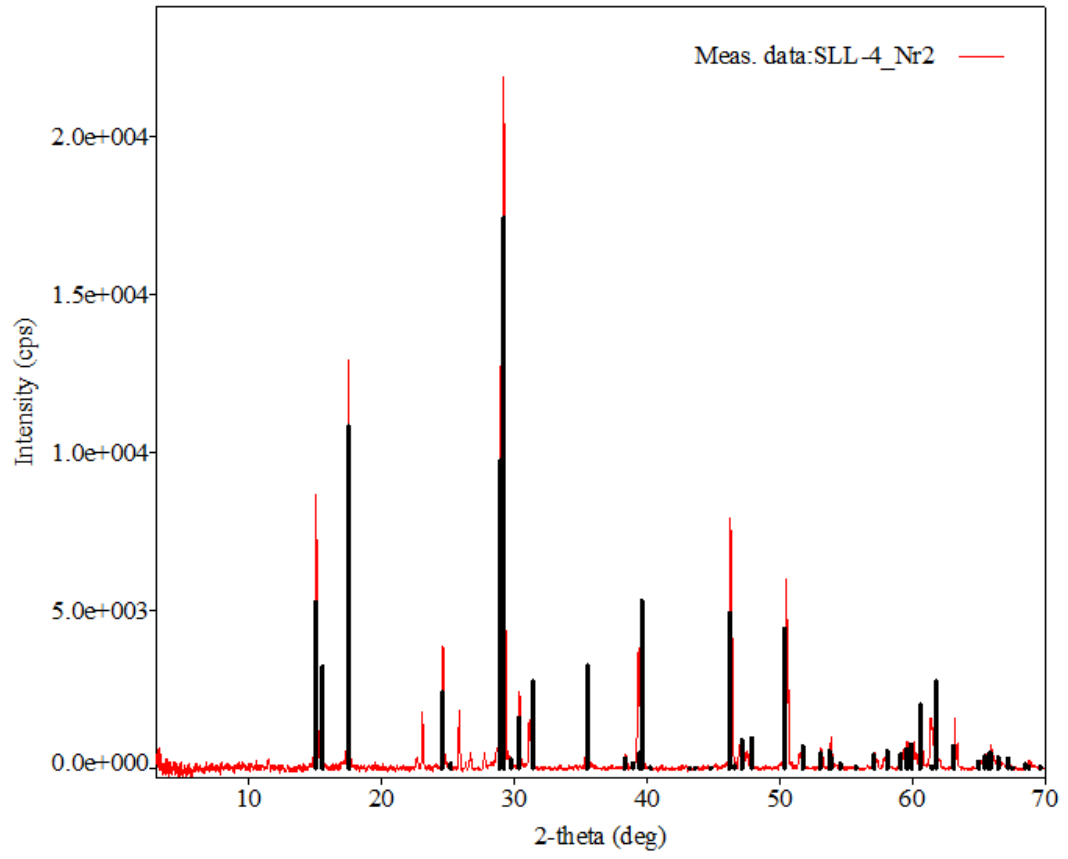
F   SEM measurements

SEM measurements courtesy of Dr Tae-Hyun Kim, University of Southern Denmark. Roughly 1 mg of the sample was dispersed in 1 mL ethanol and then subjected to ultrasonication for 15 min. A drop of the mixture was then dried at 50 °C for 10 minutes on a Si wafer before coating the sample with a 15 nm layer Au plasma.
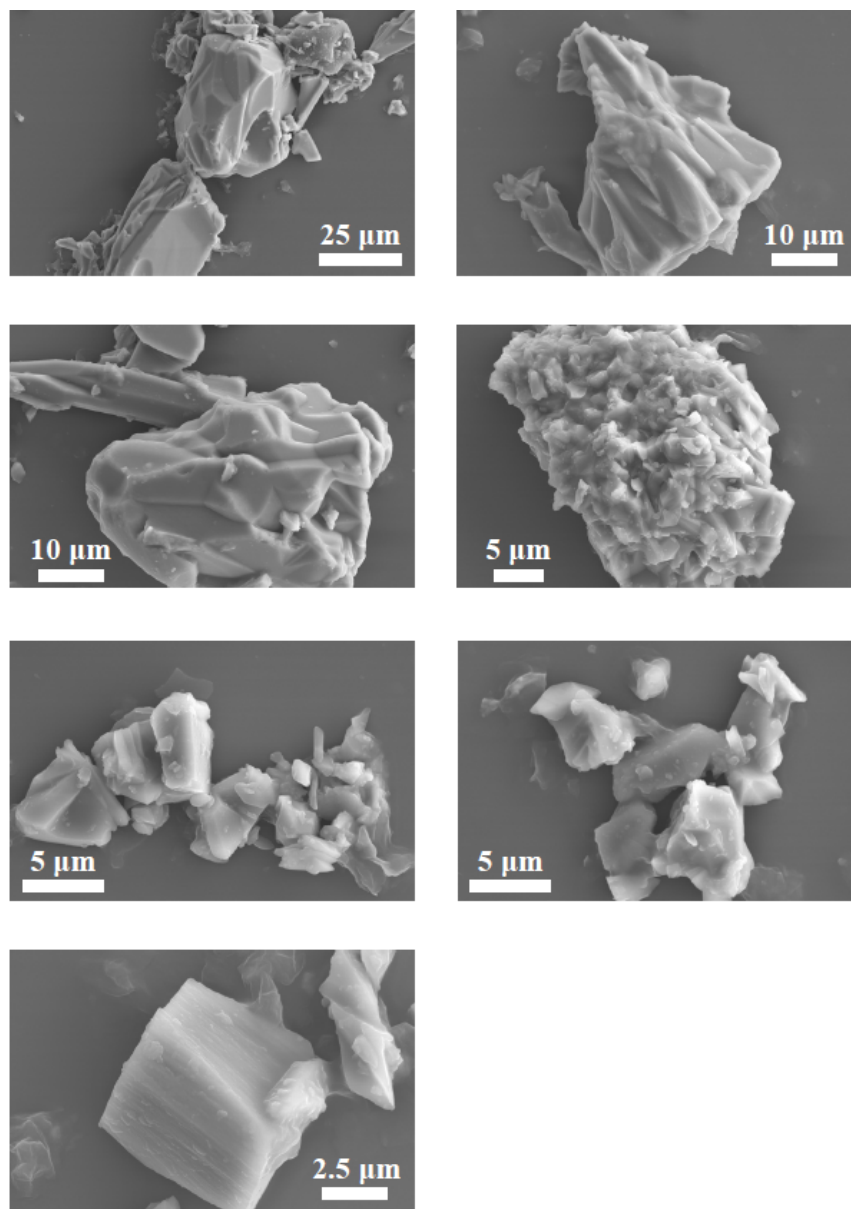

Figure 60: SEM pictures from seven areas in the sample. The length scale is indicated on each picture.

G   EDS measurements

EDS measurements courtesy of Dr Tae-Hyun Kim, University of Southern Denmark.
Table 12 shows the EDS measurements from five randomly chosen positions in the sample, acquired with a 15 kV accelerated electron beam at 15 mm working distance. The tables show the distribution of O, S, K and Cr in the sample by both weight percentage (wt%) and atom percentage (at%). Weight percentage indicate how much of the samples mass is constituted by a specific element, whereas the atom percentage indicate the number distribution of atoms of the elements that make up the sample.
Table 13 shows the average from the five measurements, including the standard deviations of the weight percentage and atom percentage.

Element	wt%	at%
O	47.20	70.75
S	13.10	9.80
K	7.50	4.60
Cr	32.21	14.86

Element	wt%	at%
O	38.04	62.70
S	14.14	11.63
K	8.42	5.68
Cr	39.40	19.99

Element	wt%	at%
O	33.99	58.37
S	15.61	13.38
K	9.36	6.58
Cr	41.03	21.68

Element	wt%	at%
O	46.87	70.51
S	12.90	9.69
K	7.69	4.74
Cr	32.54	15.06

Element	wt%	at%
O	30.77	54.92
S	15.29	13.62
K	10.12	7.39
Cr	43.83	24.07

Table 12: EDS measurements from five random positions in the sample.

Element	wt%	$\sigma_{wt\%}$	at%	$\sigma_{at\%}$
O	39.37	7.45	63.45	7.11
S	14.21	1.23	11.62	1.88
K	8.62	1.11	5.80	1.20
Cr	37.80	5.20	19.13	4.08

Table 13: Average of the five measurements from table 12.

H   Constant-q cuts

Constant-q cut of inelastic neutron scattering data for $E_i = 2.2$ meV and $E_i = 3.7$ meV, similar to that of $E_i = 7.6$ meV in figure 20.
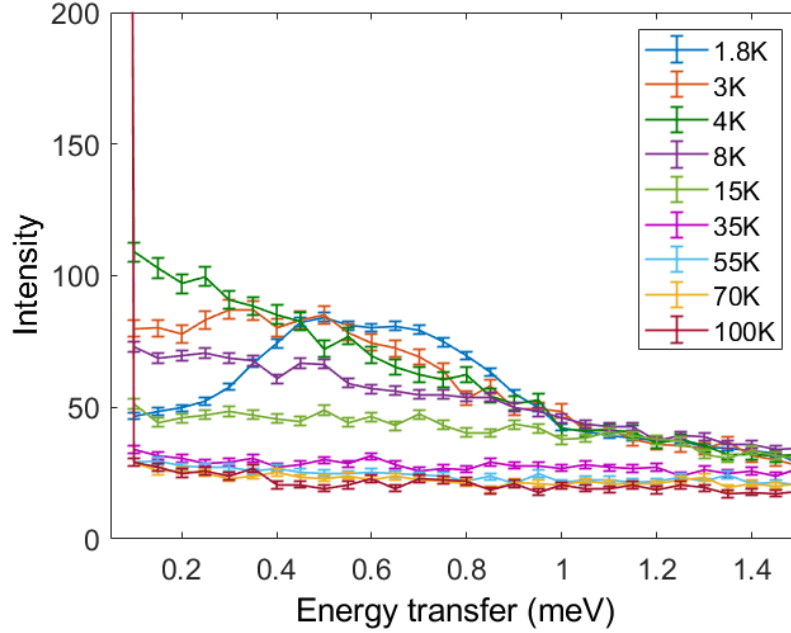

Figure 61: Constant-q cut at $q = 1.10 \pm 0.05\,\text{Å}^{-1}$ for $E_i = 2.2$ meV at all temperatures. Y-axis shows the intensity in arbitrary units.
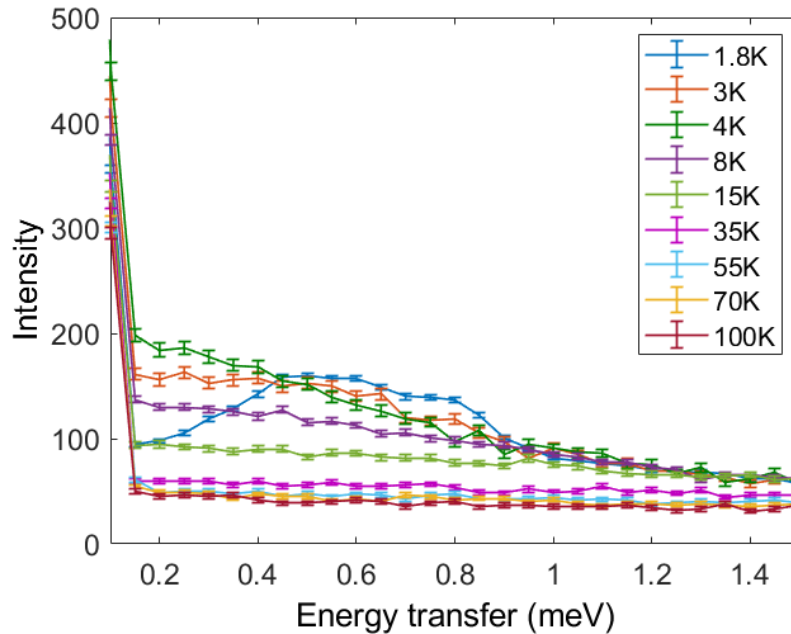

Figure 62: Constant-q cut at $q = 1.10 \pm 0.05\,\text{Å}^{-1}$ for $E_i = 3.7$ meV at all temperatures. Y-axis shows the intensity in arbitrary units.